

Individualized prescriptive inference in ischaemic stroke

DOMINIC GILES^{1*}, ROBERT GRAY¹, CHRIS FOULON¹, GUILHERME POMBO¹, JAMES K. RUFFLE¹, TIANBO XU¹, H. ROLF JÄGER¹, JORGE CARDOSO², SEBASTIEN OURSELIN², GERAINT REES¹, ASHWANI JHA¹, PARASHKEV NACHEV^{1*}

¹UCL Queen Square Institute of Neurology, University College London, London, UK

²School of Biomedical Engineering & Imaging Sciences, King's College London, London, UK

**Corresponding authors*

Abstract

The gold standard in the treatment of ischaemic stroke is set by evidence from randomized controlled trials, based on simple descriptions of presumptively homogeneous populations. Yet the manifest complexity of the brain's functional, connective, and vascular architectures introduces heterogeneities that violate the underlying statistical premisses, potentially leading to substantial errors at both individual and population levels. The counterfactual nature of interventional inference renders quantifying the impact of this defect difficult. Here we conduct a comprehensive series of semi-synthetic, biologically plausible, virtual interventional trials across 100M+ distinct simulations. We generate empirically grounded virtual trial data from large-scale meta-analytic connective, functional, genetic expression, and receptor distribution data, with high-resolution maps of 4K+ acute ischaemic lesions. Within each trial, we estimate treatment effects using models varying in complexity, in the presence of increasingly confounded outcomes and noisy treatment responses. Individualized prescriptions inferred from simple models, fitted to unconfounded data, were less accurate than those from complex models, fitted to confounded data. Our results indicate that complex modelling with richly represented lesion data is critical to individualized prescriptive inference in ischaemic stroke.

Main text

Marked individual variability in response to treatment is near-universal across medicine. However plausible the therapeutic mechanism, estimating the efficacy of an intervention—for a specific patient and across the population—requires *inference from empirical observations of treatment outcomes*. The established inferential approach, enshrined in the randomized controlled trial (RCT), seeks to estimate the average treatment effect (ATE) across populations described simply enough to permit modelling with standard statistical methods under randomized treatment allocation policy¹. The critical underlying assumption—random inter-subject variability—is secure where the underlying biological mechanisms are homogeneous across the population, but violated where they are heterogeneous, invalidating any inference that rests on it: for both the individual patient and the whole population². For example, in the presence of two subpopulations of equal size and diametrically opposite responses—one negative, one positive—the average treatment effect will tend towards zero, regardless of the statistical power of the study, the quality of the data, and the magnitude of subpopulation-specific effects (Figure 1). Crucially, heterogeneity is not detectable within the prespecified trial evaluation itself, nor necessarily in any subsequent subgroup analysis based on the same trial specification: richer descriptions, more flexible models, and less reductive estimands are required³⁻⁶. The heterogeneity must be explicitly exposed by a new attribute—the differentiation between ischaemic and haemorrhagic stroke in thrombolysis offers a striking example⁷—or hitherto unmodelled relations between attributes. Moreover, it may be so complex as to be impossible to capture within the simple, rigid statistical practice RCTs conventionally enforce.

This cardinal problem has three major consequences. First, an intervention may be mistakenly judged to be ineffective for all when it benefits an identifiable many, prematurely dismissing a valuable treatment, wasting the cost of its development, and discouraging further research into its mechanism and application⁸. Second, an intervention may be avoidably prescribed to those who do not respond or are harmed by it, degrading clinical outcomes, exposing patients to unnecessary risk, and promoting systematic inequalities in care. Third, since RCTs, with ATE as the outcome measure, have been placed on the highest pedestal, at the apex of the hierarchy of clinical evidence, neither argument nor data outside the established framework is permitted to gainsay them, indefinitely perpetuating both the errors and their consequences⁹.

Arguably nowhere is this defect more important than in stroke, worldwide the second commonest cause of death and the commonest cause of adult neurological disability^{10,11}. Though the aetiology is comparatively simple—vascular rupture, occlusion, or both—and the immediate treatment commensurately focused^{12,13}, the functional deficits subsequent management must address may be as complex as the organization of the brain itself¹⁴. The observed patterns of disability, responses to treatment, and long-term recovery all suggest marked heterogeneity¹⁵, explicitly violating the assumptions on which conventional interventional inference rests. Indeed, what we know of the functional anatomy of the brain¹⁶, and the topology of ischaemic lesions, makes it inevitable that their interaction in stroke should exhibit a complex but nonetheless organized structure that may not be dismissed as random noise¹⁷⁻¹⁹. A “one-size-fits-all” assumption is not only biologically implausible here: it is directly contradicted by the facts².

Without a means of capturing complex heterogeneity historically, we have had no option but to ignore it²⁰ or model it in an oversimplified manner²¹. But the combination of machine learning with large-scale data now renders statistical models of sufficient expressivity and flexibility computationally tractable and deployable in real world practice⁴⁻⁶. Inferences about individuals may now be informed by the local subpopulation to which they belong—defined by many clinical, physiological, and anatomical characteristics—estimating treatment effects much closer to the level of the individual, opaque to the global, population-level,

perspective that is the limit of conventional approaches. Within such *individualized prescriptive inference*, the underlying statistical model seeks to determine not the ATE across the population, but the *conditional average treatment effect* (CATE) informed by a *wide array* of the patient's distinctive features, resulting in estimates that are much more personalized, with reduced systematic variability across the population²². Just as the now familiar heterogeneity of ischaemic vs haemorrhagic stroke was resolved by brain imaging, so as yet unknown heterogeneities defined by multiple factors may be resolved by complex modelling of rich data^{15,23–25}.

How do we realize such an individualized approach? Where available, observations of responses to unconfounded treatment allocation—such as from a traditional RCT—may be combined with established low-²⁶ or novel high-dimensional¹⁹ multivariable modelling of conditional outcomes^{4–6}. Randomization remains a powerful strategy, the best available means of protection from hidden confounding. But in the setting of unknown heterogeneity defined by *many* interacting factors, the necessary data scale becomes infeasibly large, forcing reliance on routine clinical data streams with limited control over randomization. We must therefore determine the *comparative* importance of minimizing confounding due to non-random treatment allocation policies *vs* maximizing model expressivity and flexibility in inferring the prescription for each patient. If accuracy is now shown to be more sensitive to the former than the latter, then a RCT remains the optimal approach. Conversely, if model expressivity and flexibility are shown to be decisive, then achieving the data scales machine learning requires—and only routine clinical streams can provide—becomes paramount. In an ideal world, randomization would be combined with highly expressive models⁶: the question is where the compromise should lie when real-world constraints place the two in opposition.

Examining the largest set of registered acute stroke lesion data ever assembled—4,119 lesions—here we perform a comprehensive comparison of traditional interventional inference—randomized allocation policy with simple covariate adjustment—*vs* a novel approach—flexible counterfactual modelling of non-randomized data based on deep representation learning of anatomical patterns of damage. Our analysis tests the hypothesis that, under real-world constraints, the fidelity of inferred individual prescriptions depends *less* on unconfounded treatment allocation policy than on capturing treatment response heterogeneity with expressive generative models combined with flexible causal models. Our null hypothesis concerns CATE-based inference in the context of varying degrees of treatment allocation, and representations that vary from narrowly-defined (effectively ATE-based inference), to richly expressive: complex representations plus confounded allocation is not superior to simple representations plus random allocation. On the rejection or otherwise of the hypothesis rests the optimal inferential policy for evaluating treatments in acute stroke sensitive to the functional organization of the brain.

Since counterfactual outcomes of treatment are unobserved, this comparison requires a potential outcomes modelling framework^{27,28}. Crucially, we cannot rely on empirical evidence of treatment efficacy from standard RCTs, for we are concerned with the setting of heterogeneity where their assumptions are definitionally violated. In the absence of a ground truth, constitutive of the inferential problem here, we are compelled to use a semi-synthetic counterfactual framework^{29–33}. To promote real-world generalizability, our simulations are informed by large-scale, multi-modal empirical data: high-resolution lesion anatomy, and meta-analytic functional³⁴, gene transcription³⁵, and neurotransmitter receptor³⁶ maps. Moreover, we traverse a wide space of plausible real-world settings—systematically manipulating the richness of lesion parameterization, the magnitude and variability of treatment effects, the extent of treatment–outcome confounding, and the biological nature of the underlying deficit and treatment responsiveness—across the largest set of simulations ever performed with brain lesion data of any kind.

Following well-established principles of causal inference³⁷⁻³⁹, our approach relies on a causal model, represented by a directed acyclic graph, of the spatial relationship between brain lesions and functional anatomy—a map of disrupted functions—and between treatment receipt and physiological anatomy—a map of treatment responsiveness—that explains observable patient outcomes (Figure 2). This formulation allows us to quantify the impact on the efficacy of individualized prescription of *both* observable *and* unobservable treatment–outcome confounding, across the full space of plausible real-world scenarios, including a wide range of treatment and recovery effects. We can thus directly address the question of the relative contribution of randomization—the advantage of RCTs—and greater model expressivity and flexibility—the advantage of complex models of large-scale observational data, where real-world constraints force a compromise between the two approaches.

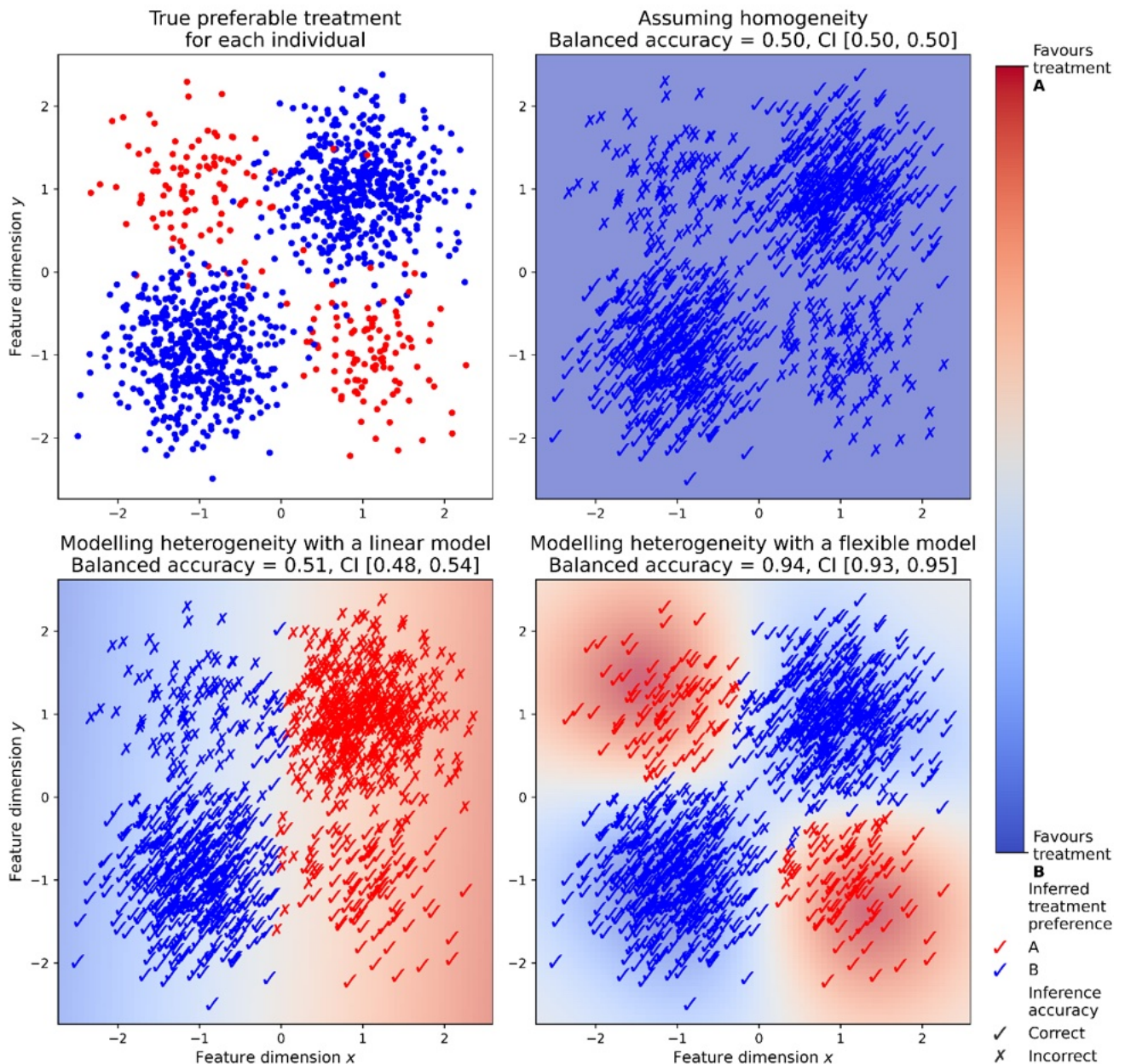


Figure 1. Inferring treatment effects in the setting of heterogeneity. Consider a hypothetical scenario where the members of a population described on continuous dimensions (x & y) systematically differ in their responsiveness to two treatments (A (red) & B (blue)). The two populations differ in size (A is smaller), and are non-linearly distinguished by their features (occupying diametrically opposed quadrants of the feature space). A statistical model of the optimal treatment that ignores the heterogeneity entirely, unconditionally averaging across all patients, inevitably favours B wholesale as the larger proportion, achieving chance level balanced accuracy (upper right). A model accounting for heterogeneity in simple, linear terms (a linear support vector machine) achieves only slightly better accuracy, for the distinguishing features are not linearly separable (lower left). By contrast, a model flexible enough to absorb complex, non-linearly defined heterogeneity (a support vector machine with a radial basis function kernel) achieves near perfect balanced accuracy (lower right). Note the differences in fidelity here can only be entrenched by higher quality or larger scale data, for they are a consequence not of the data or its sampling but of the mismatch between the complexity of the data and the flexibility of the statistical model.

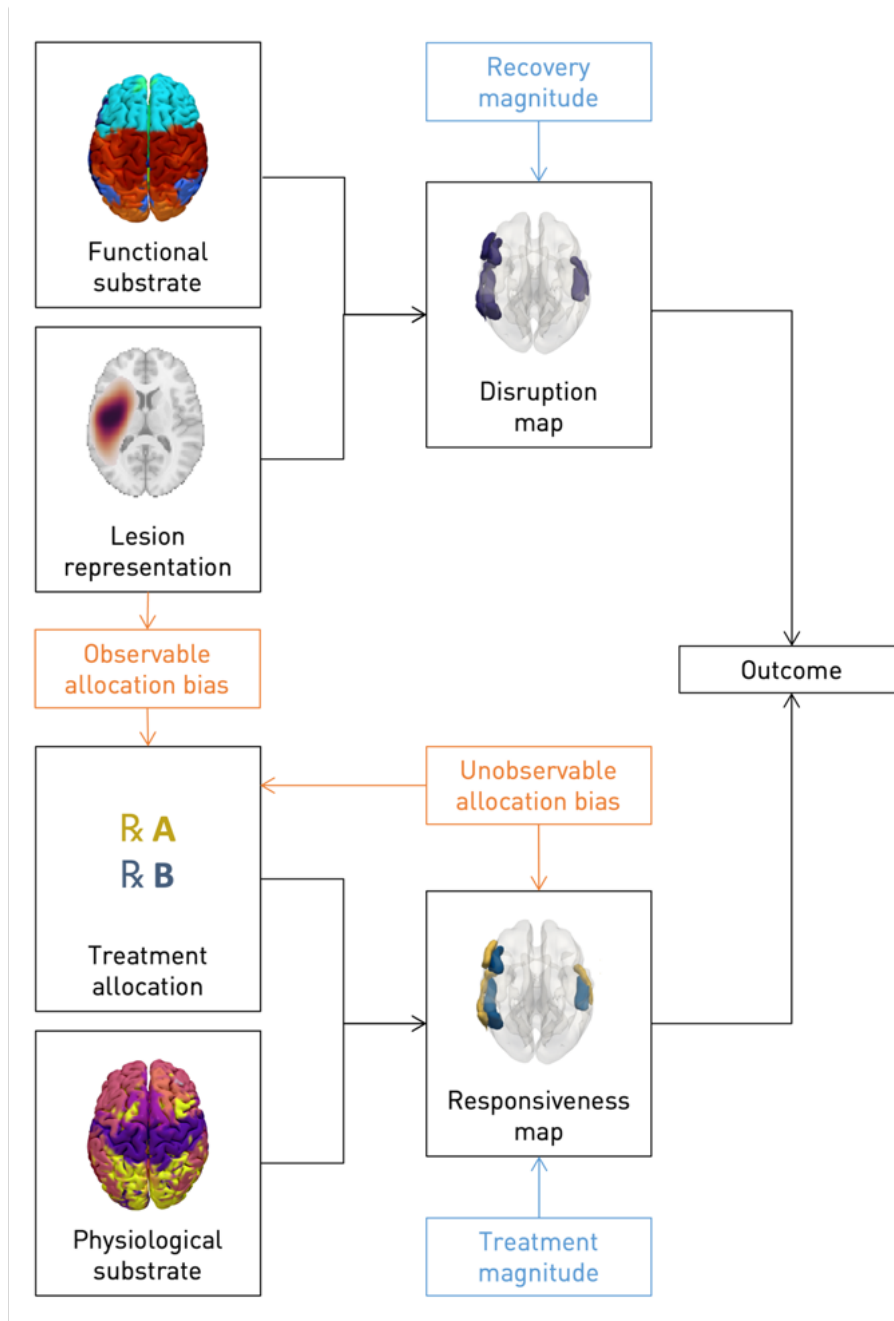
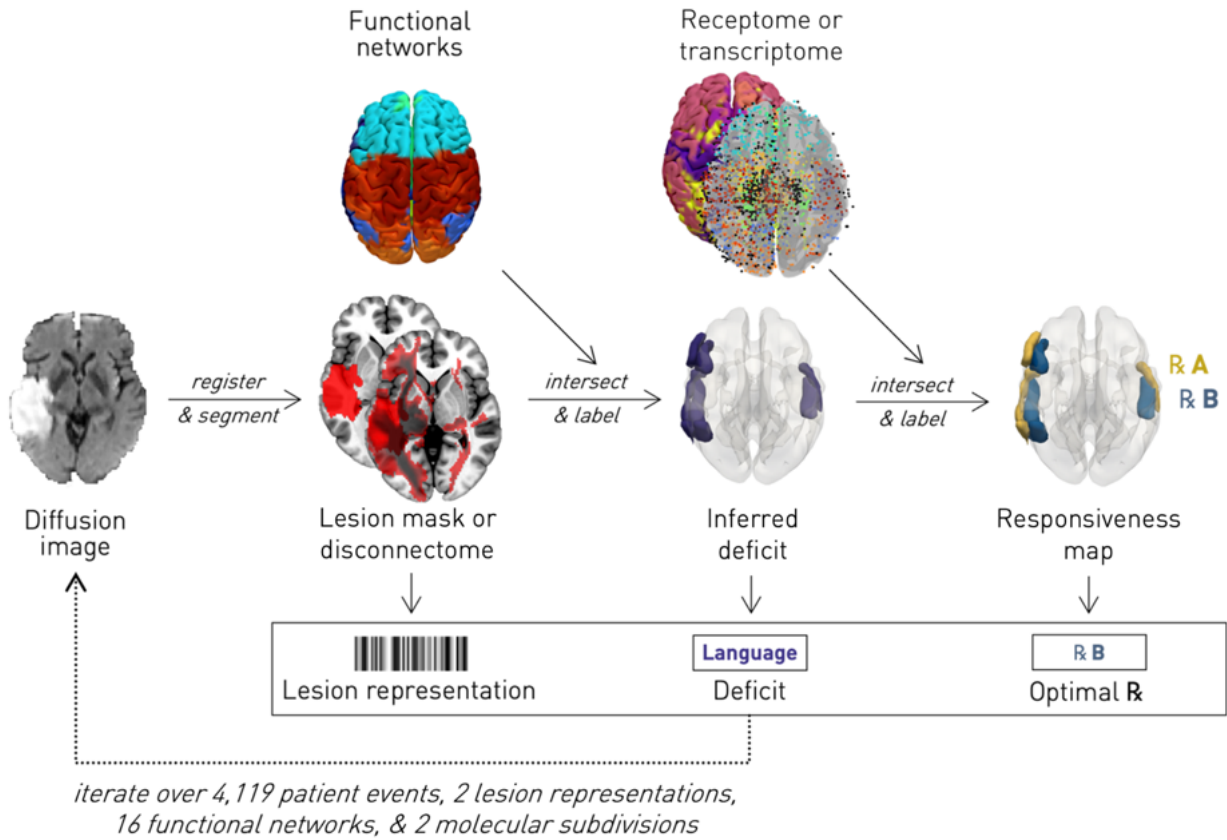


Figure 2. Causal modelling of treatment—conditional outcomes in stroke. Directed acyclic graph of the modelled causal relations between brain lesions and functional anatomy—a map of disrupted functions—and between treatment receipt and physiological anatomy—a map of treatment responsiveness—in generating the observed outcome. The lesion anatomical representation (lesion or disconnectome) interacts with the functional substrate to generate a data-driven functional *disruption map*. In parallel, the treatment allocation policy interacts with the physiological substrate (microarray RNA transcription or neurotransmitter receptor data) to generate a data-driven treatment *responsiveness map*. These two spatial maps intersect to generate the patient outcome, modulated by the magnitudes of recovery and treatment effects. The relationships are modelled to be corrupted by varying degrees of observable or unobservable confounding due to non-random treatment allocation, enabling quantification of their impact on the fidelity of inferred optimal treatment.

Ground truth generative process



Prescriptive modelling & evaluation

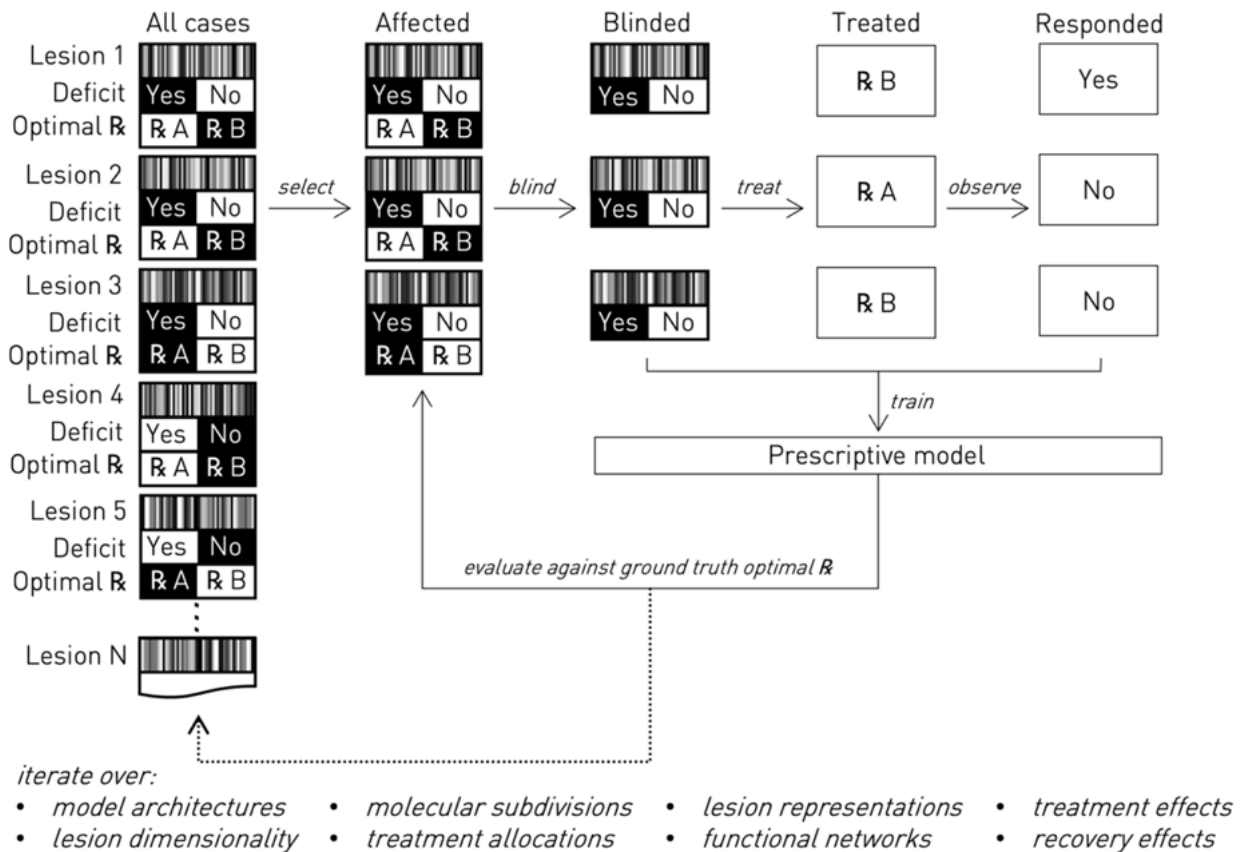


Figure 3. Semi-synthetic ground truth synthesis (upper panel). Schematic of the process of semi-synthetic ground truth generation from lesions or disconnectomes, given meta-analytic maps of brain functional organization and physiology. Diffusion weighted magnetic resonance images were obtained from patients with confirmed acute ischaemic stroke. Each image volume was non-linearly transformed into Montreal Neurological Institute (MNI) template space, facilitating voxel-based comparisons between different lesioned images and with meta-analytic functional and physiological maps. A binary ischaemic mask was automatically segmented from each image, and used to simulate real-world individual-level variability of functional deficits and treatment responses. The overlap between each lesion and each of 16 meta-analytic functional grey matter networks, transformed into MNI space, was used to generate plausible synthetic functional deficits (lesion-deficit simulation). The anatomical territory associated with each functional network were further subdivided by transcriptome or receptome distribution data into two subregions, variably responsive to different interventions, furnishing treatment effect heterogeneity. A plausible anatomically determined ground truth for treatment responsiveness is thereby established, enabling explicit quantification of the fidelity in inferring the optimal treatment. The resulting semi-synthetic data comprise stroke phenotype representations, associated functional deficits, and the designated optimal treatment for each patient simulation.

Virtual interventional trials (lower panel). We used Monte Carlo methods to simulate a large number of virtual trials across the full set of modelled lesion-deficit relationships, treatment responsiveness, and treatment allocation policies. For each functional network, all patients with corresponding deficits were recruited to virtual trials in which they receive one of two treatments. At least one of these was determined to be truly effective. Non-random treatment allocation as may occur in an observational setting was simulated using a confounding hyperparameter, ranging from 0 (randomized) to 1 (treatment selection based strongly upon patient phenotype). A patient's response to a given treatment was dependent upon two sources of probabilistic noise: treatment effect, $\mathbb{P}(\text{response} \mid \text{truly susceptible})$, and recovery effect, $\mathbb{P}(\text{spontaneous response})$, independent of treatment received and responsiveness. These sources of noise are always present to some degree in any trial, randomized or observational. Within 10-fold cross-validation, prescriptive models were fitted using the training set, with quantified noise and confounding, for the objective of retrieving the optimal treatment, to each individual patient. The model was evaluated using a held-out test set, for lesion representations, disconnectome representations, functional networks, genetic expression-derived treatment responsiveness subnetworks, and receptor distribution-derived treatment responsiveness subnetworks, across the ranges of confounding, treatment effect and recovery effect.

Results

To test our hypothesis, we must first establish a semi-synthetic framework for empirically-informed *virtual interventional trials* (Figure 3). A real trial is inadequate, for the success or failure of a treatment has no ground truth against which the fidelity of the inference can be quantified. Since the disability caused by a stroke is directly related to the underlying disrupted functional anatomy, it is natural to posit lesion–deficit relations in terms of observed, potentially disrupted, neural patterns of functional organization, even if other factors will inevitably bear on the outcome. Equally, responsiveness to treatments acting downstream of the vascular disruption—e.g. tissue preservation, modulation, or regeneration—is plausibly sensitive to the biological properties of the damaged or threatened substrate. Our semi-synthetic simulation framework therefore combines lesion–deficit ground truth maps from functional anatomical data with treatment responsiveness ground truth maps from physiological, receptor distribution and genetic expression data. Both sets of simulated ground truths are derived from comprehensive, large-scale, meta-analytic data in the public domain. Finally, we need a large, maximally inclusive collection of acute stroke lesion maps that is plausibly representative of the heterogeneity of the population, registered into a common anatomical space to allow faithful comparison between individuals. A small sample biased by selective recruitment would inevitably lead to under-estimates of observed heterogeneity and our capacity to model it.

A data-driven map of functional networks in the human brain

To construct a set of ground truth lesion–deficit relations maximally grounded in real-world evidence, we derived a hierarchical grey matter functional parcellation of the human brain from a comprehensive analysis of NeuroQuery meta-analytic functional imaging and associated textual data³⁴. Hierarchical voxel-based clustering of individual behavioural and cognitive terms based on the similarity of corresponding neural activation patterns yielded 16 distinct functional networks covering the full range of imaged behaviours (Figure 4; Supplementary S1). Remarkably, though the clustering was driven solely by these activation patterns, strong commonalities in the keyword terms belonging to each cluster emerged—across the network archetypes of hearing, language, introspection, cognition, mood, memory, aversion, coordination, interoception, sleep, reward, visual recognition, visual perception, spatial reasoning, motor, and somatosensory—corroborating the fidelity of the mapping approach (Supplementary S2). Each of these 16 archetypal functional networks provided a plausible ground truth for the critical neural substrates of the associated group of behaviours, replicating the likely spatial form and complexity of actual lesion–deficit relations, across the entire behavioural landscape.

Genetic expression and receptor-determined treatment responsiveness

To create biologically plausible patterns of treatment response heterogeneity, individual variation in response was determined by further subdivision of the functional networks guided by physiological, whole-brain genetic expression maps³⁵ or by neurotransmitter receptor distributions³⁶. A deficit associated with a given functional network was thus designated as preferentially responsive to one of two treatments, dependent on which genetic expression or receptor-directed subdivision (Supplementary S9 & S10) is primarily disrupted by a given lesion. Crucially, treatment responsiveness, like the deficit itself, is thereby rendered sensitive to the anatomy of the lesion in its interaction with plausibly material biological features. Again, the objective is to replicate the likely form and complexity of anatomically organized determinants of responsiveness, not to identify them for any specific function.

Lesion-deficit and treatment response simulation

A set of 4,119 non-linearly registered diffusion-weighted magnetic resonance images (DWI) from 2,830 unique unselected patients with confirmed acute ischaemic stroke was used to create a set of empirically informed, simulated lesion–deficit relations (Figure 3, upper panel; Figure 5). Though a proportion were drawn from the same patient, no images from within the same 30-day period from the same individual were retained in the dataset, as visualized in Supplementary S3.

Lesion binary masks automatically segmented from each DWI and transformed into standard MNI stereotactic space were intersected with each of the 16 functional grey-matter networks, yielding 4,119 lesion–deficit relations across the full range of lesions and behaviours. A lesion intersecting with $\geq 5\%$ of a subnetwork was designated as causing a corresponding deficit. To capture the broader impact of lesions on grey matter-defined functional areas through white matter damage, “disconnectome” representations were also generated from each lesion mask^{40,41}, extending each lesion to remote grey matter areas disconnected by it, weighted in proportion to the extent of connectivity (Figure 5). Disconnectome deficits were analogously designated, using a threshold of 0.5 to binarize the representation.

For each lesion and each functional network affected by it, the intersection with the responsiveness maps (see Figure 2) determines whether the individual is included in the trial and, if they are, their responsiveness to the two treatments. The precise mechanism with which the intersection determines inclusion and response is described in the Methods section *Ground truth modelling*.

Prescriptive inference with virtual interventional trials

Having generated a ground truth, we conducted a series of virtual interventional trials, where each patient event—defined by empirical lesion anatomy, the corresponding simulated deficit, and simulated treatment responsiveness—was allocated to receive one of two treatments, differing in their individual-level effects as outlined above (Figure 3, lower panel). The task is to fit probabilistic models of individual outcomes to the trial data, from which we can then infer individualized prescriptions. Unlike a real trial, however, here we can quantify the fidelity of the inference against the ground truth, where the outcome for each individual, given each treatment, is known. This enables us to compare the performance of different models and experimental settings objectively²⁷.

To capture the full space of possible treatment and response scenarios, we varied both treatment and recovery effects across their entire possible range within independently conducted trials. Similarly, to generate treatment–outcome confounds, we vary the degree to which treatment allocation policy depends on lesion location, from not at all (random/unconfounded), to fully deterministic (non-random/confounded). In the process, we observe the effect on prescriptive inference as the assumptions underlying causal inference (see Methods section *Prescriptive inference*) are stretched to breaking point⁴².

An alternative non-random allocation regime based on unobserved covariates was additionally implemented as a test of hidden confounding. The complete combination of these parameters—functional network, treatment responsiveness, lesion representation, treatment effect, recovery effect, and allocation policy—yielded 22,528 separate virtual clinical trial conditions, of which a 10-fold cross-validation scheme was implemented and results evaluated over 460 representation–prescriptive configuration combinations, leading to a total of 103,628,800 simulations.

Each trial used machine learning to model the distribution of conditional outcomes. We used the following model architectures: random forest⁴³, extremely randomized trees⁴⁴, XGBoost⁴⁵, logistic regression⁴⁶ and

Gaussian process⁴⁷. Here, the models were trained using cross-validation to predict outcomes from treatment allocation and representations of lesion anatomy. The treatment to prescribe is then inferred to be the one that has the greatest relative probability of causing a favourable outcome. The efficacy of this prescription is evaluated using balanced accuracy (Figures 6 and 7); see also Methods section *Prescriptive inference* and Supplementary S11-17 for other evaluations.

To quantify the value of capturing the anatomical detail of lesions with expressive representational models, each stroke lesion representation (binary lesion mask or disconnectome) was embedded into a low-dimensional space, using a volume variational deep auto-encoder (VAE)⁴⁸, volume non-variational deep auto-encoder (AE), non-negative matrix factorization (NMF)⁴⁹ and principal component analysis (PCA)⁵⁰ to latent embeddings of varying length up to 50 components¹⁷. Independent models employing progressively higher dimensional representations were then compared against the baseline low-dimensional lesion representations typically employed in conventional stroke trials, vascular territory (anterior circulation ischaemic stroke or posterior circulation ischaemic stroke), or 6 specific arterial divisions, adapted from the atlases presented by Liu et al⁵¹. Each trial was thus evaluated with 46 representations: two low-dimensional baselines and eleven incrementally higher dimensional ones across four representational rationales.

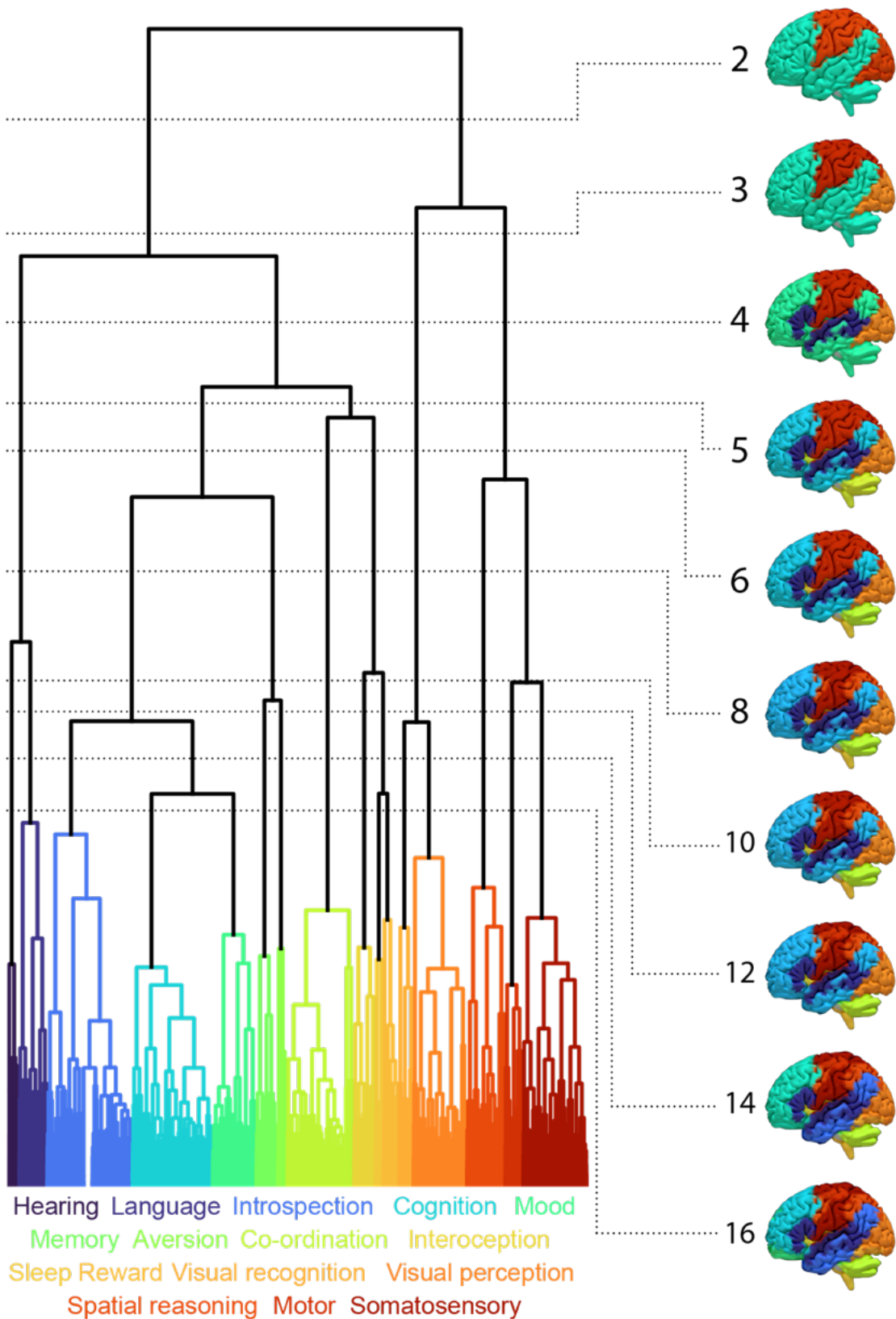


Figure 4. Functional ground truths. Functional grey matter parcellation dendrogram, showing agglomerative voxel-based clustering based upon association distances between voxels in their functional distributions. Visualizations of functional groupings at various thresholds up to 16 are shown on the right, displaying the grey matter functional hierarchy. From the 16-network parcellation, the archetypal terms associated with each group are shown below the dendrogram, with consistency of colours throughout.

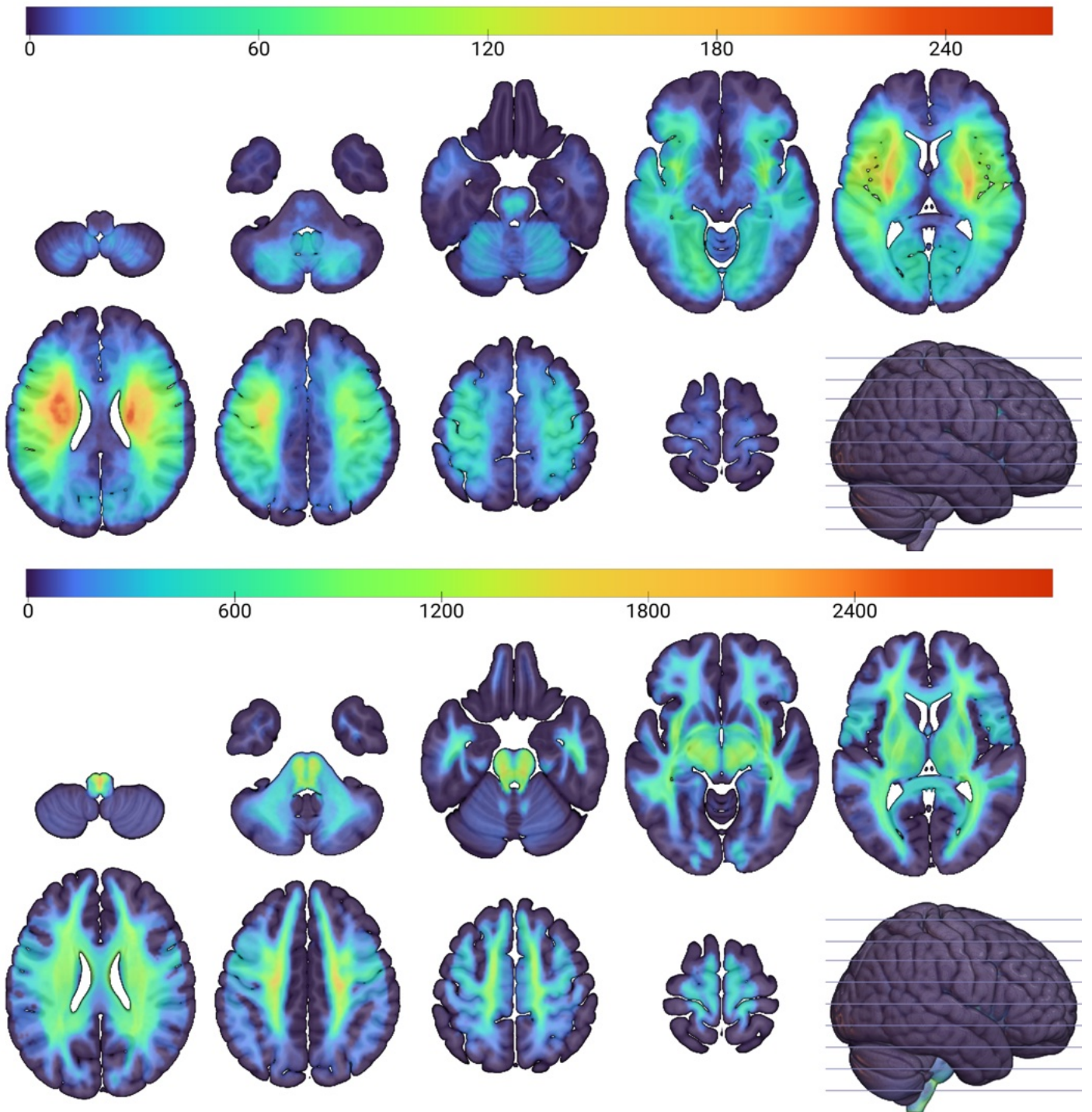


Figure 5. Lesion (upper panel) and disconnectome (lower panel) anatomical distributions. Axial slices showing the coverage in voxel-based summation of binary ischaemic maps of lesions (upper), and the summation of binarized disconnectome distributions ($p > 0.5$) associated with each of the lesions (lower), showing coverage across the brain. For both representations, $N = 4,119$.

Prescriptive inference is limited by model dimensionality, not allocation policy

Under statistically ideal conditions—large treatment effects, infrequent spontaneous recovery, random allocation—prescriptions based on richly expressive representations were significantly more accurate than simple vascular baseline models overall (Figure 6, upper left corners of each panel; Figure 7, upper row of each panel).

With lesion masks as the input, balanced accuracy for inferring the optimal treatment from the 50-dimensional VAE representation, averaged across all 16 functional networks, was 0.793 [95% CI [0.75, 0.84]], vs 0.523 [95% CI [0.50, 0.55]] for a simple vascular baseline ($t = 10.5$, $p = 1.66 \times 10^{-18}$, Cohen's $d = 1.96$). A similarly striking difference was revealed by precision-in-estimation-of-heterogeneous-treatment-effects (PEHE, lower is better), yielding 0.466 [95% CI [0.44, 0.49]] for the 50-dimensional VAE representation vs 0.676 [95% CI [0.63, 0.72]] for the simple vascular baseline ($t = -8.12$, $p = 3.92 \times 10^{-13}$, Cohen's $d = -1.44$), indicating superiority of the richly expressive representation across both metrics.

With disconnectomes as the input, balanced accuracy from the 50-dimensional VAE representation was 0.875 [95% CI [0.83, 0.92]], vs 0.546 [95% CI [0.52, 0.57]] for the simple vascular baseline ($t = 13.5$, $p = 4.28 \times 10^{-24}$; Cohen's $d = 2.62$); by PEHE, 50-dimensional VAE yielded 0.349 [95% CI [0.33, 0.37]] vs 0.592 [95% CI [0.56, 0.63]] for the simple vascular baseline ($t = -10.2$, $p = 2.86 \times 10^{-17}$, Cohen's $d = -2.13$), similarly indicating broad superiority of the richly expressive representation.

With increasing noise—small treatment effects, frequent spontaneous recovery—the advantage of the richly expressive representations remained significant across most of the parameter space (white filled circles in Figure 6, right column; Figure 7, upper right panel), except for the noisiest settings where no statistical distinction could be made. Crucially, this advantage persisted even under strong corruption by treatment–outcome confounding from allocation bias (white filled circles in Figure 6, right column; Figure 7, lower right panel), generally yielding greater prescriptive fidelity even from a markedly confounded and noisy trial modelled with a richly expressive representation than from a fully randomized trial at the same noise level modelled with a simple one.

The observed patterns of comparative performance were broadly invariant when averaged across the criteria of treatment responsiveness—transcriptome or receptome (Figure 6a, b); lesion anatomical representation—lesion masks or disconnectomes (Figure 6c, d); and observability of treatment allocation confounding—location-based or unobservable (Figure 6e, f). A high-dimensional representation, even in the setting of strongly confounded allocation, was almost always at least non-inferior to the RCT-like setup, of low-dimensional models and randomization, and in the vast majority substantially superior. These findings were consistently replicated across most functional deficit simulations (Figure 7), based on the functional— anatomical networks visualized in Supplementary S9 & S10. An identical analysis based on PEHE demonstrated the same overall patterns (Supplementary S11-17).

These results provide strong grounds for *rejecting* the null hypothesis stated in the Introduction section. We have shown that complex representations plus confounded allocation are always non-inferior and almost always superior to simple representations plus random allocation.

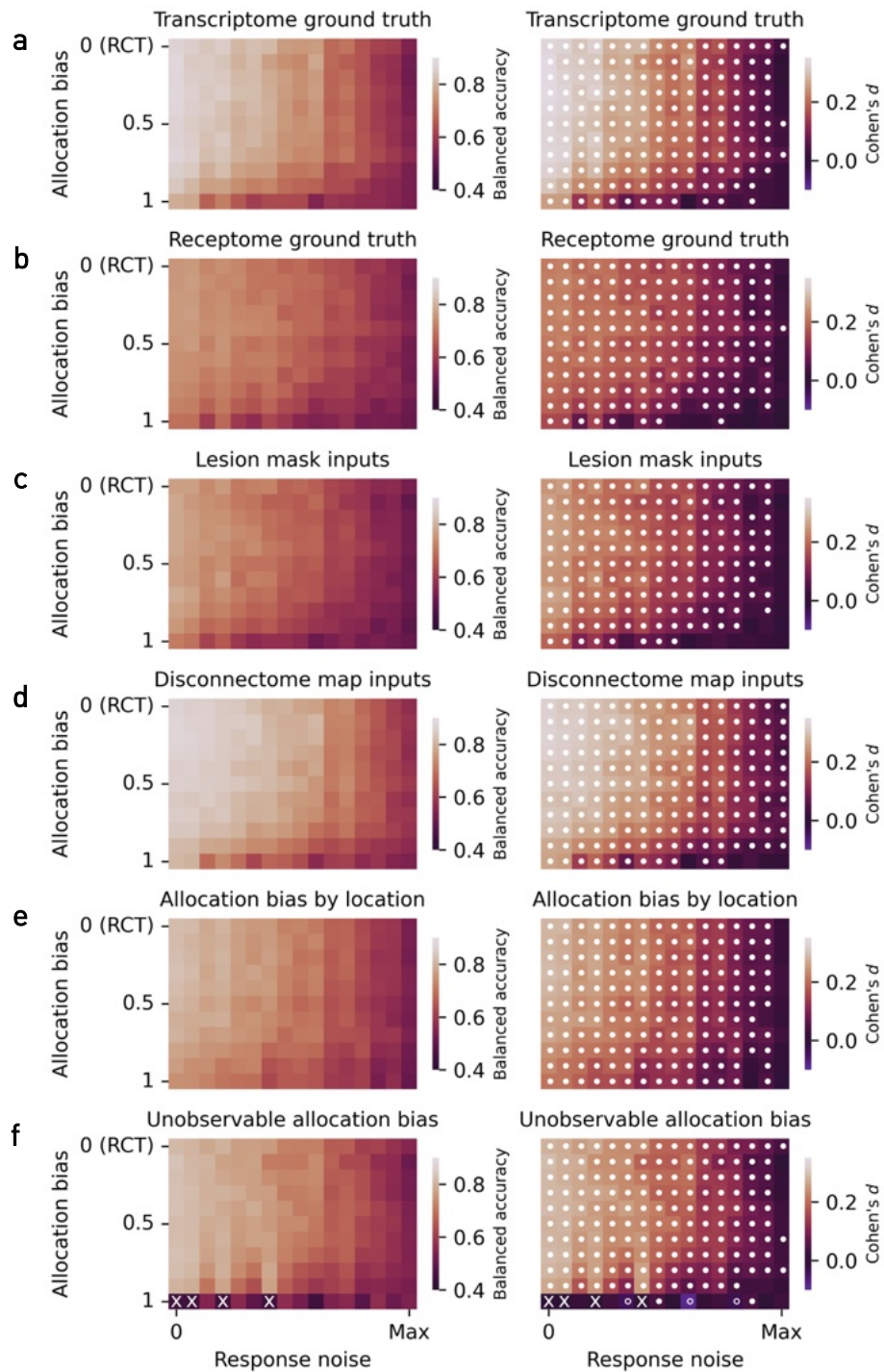


Figure 6. Prescriptive performance with the optimal richly expressive representation quantified by balanced accuracy (left panel column, see Supplementary S11-S14 for full descriptions), and statistical comparison against a simple vascular baseline, anterior or posterior vascular territories (right panel column). A filled circle indicates significantly higher performance for the expressive representation, and an unfilled circle significantly higher performance for the baseline model (using a Benjamini–Hochberg corrected critical value for 0.05 significance level). An ‘x’ indicates simulation conditions with insufficient class balance to permit prescriptive model fitting (e.g. because there are no non-responders). Rows **a** and **b** show performance averaged across the criteria for treatment responsiveness (transcriptome or receptome); rows **c** and **d** across lesion input representation type (lesion masks or disconnectomes); and rows **e** and **f** across allocation confounding observability (location-based or unobservable). The optimal expressive representation is shown to be non-inferior to simple vascular territories at informing prescription across almost the full landscape of observational conditions, and superior in the vast majority. See S15 for respective PEHE plots.

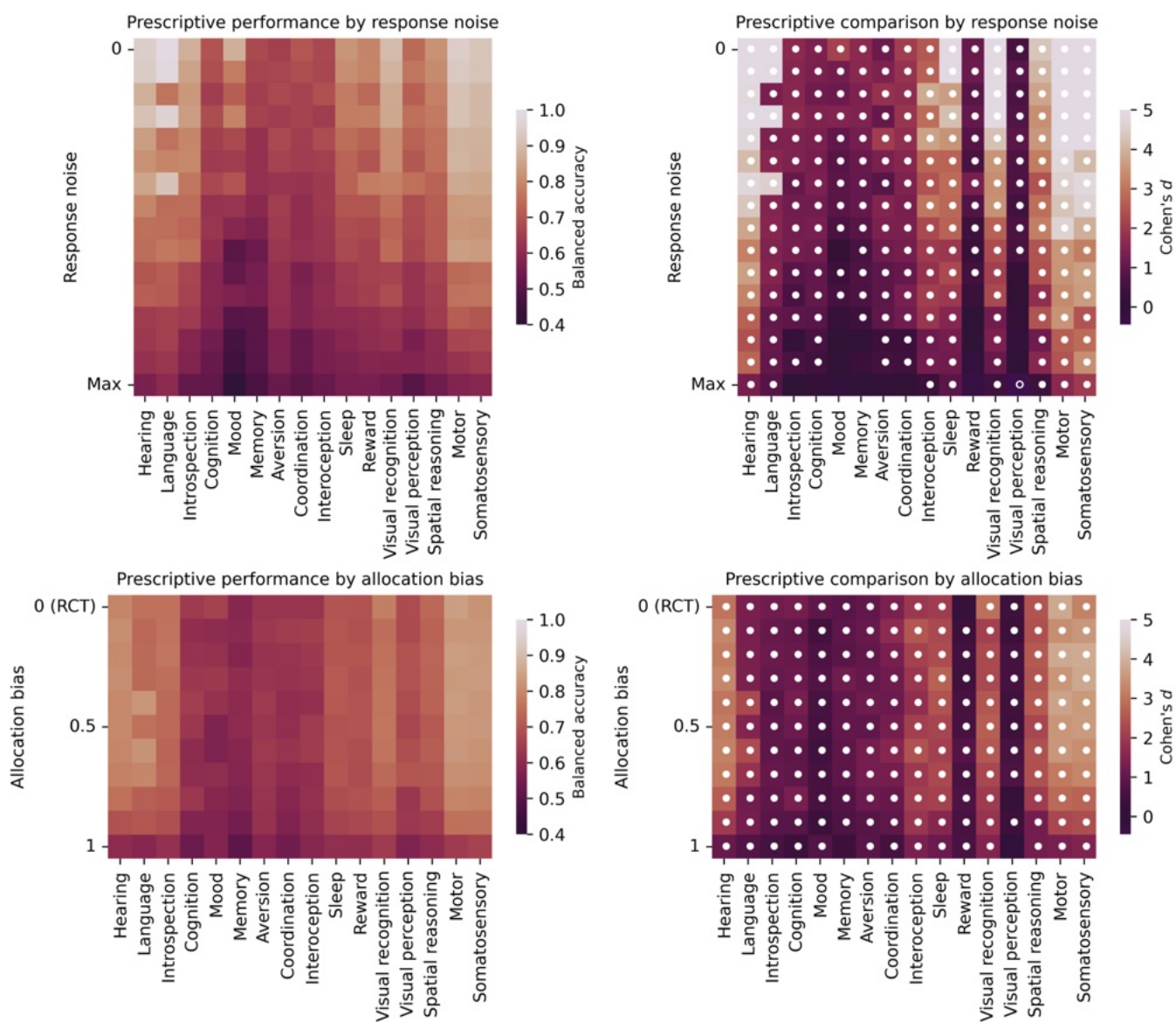


Figure 7. Prescriptive performance with the optimal richly expressive representation quantified by balanced accuracy (see S11-S14 for full description), stratified according to the modelled functional deficit, and averaged across all simulation conditions. The right column shows Cohen's *d*-effect size when comparing prescriptive performance using the optimal representation against a simple vascular baseline. A filled circle indicates superior performance for the optimal representation, beyond the Benjamini–Hochberg corrected critical value for 0.05 significance level; an unfilled circle indicates superior performance for the simple vascular baseline correspondingly. The full anatomical–physiological modelling framework is visualized in Supplementary S9 & S10 for receptome and transcriptome, respectively. The advantage in prescriptive performance for the richly expressive approach is shown to generalize across modelled functional deficits as well as data conditions defined by outcome response noise and treatment allocation confounding. See S16 for respective PEHE plot.

Discussion

We address a cardinal question in the domain of ischaemic stroke: the optimal approach, under real-world constraints, to evaluating a treatment where the deficit and treatment responsiveness may exhibit sensitivity to anatomical patterns of functional activation, neurotransmitter receptors, genetic expression, or other neural properties of similar spatial structure. This is a question no-one has previously examined. Yet the unusually large number of interventions discarded at the trial stage⁵², and the protracted history of those now persuasively shown to be beneficial⁵³, cast doubt on the felicity of the established approach founded on simple estimands, highly reductive descriptions of patients, and inflexible statistical models. Moreover, the picture of the brain emerging at every level—from the molecular to the physiological—indicates a finely granular, replicable organization overwhelmingly likely to result in treatment heterogeneity no simple approach could adequately capture⁸. Given the sheer scale of stroke worldwide, millions of years of disability may be lost not because we do not have the good treatments but because we have failed to mitigate the impact of heterogeneity on the determinability of their effects.

Crucially, this is not a question that can be answered with conventional empirical studies alone. When—as almost always—only one of many treatments can be offered to a given patient, the question of which is optimal is counterfactual, to be settled by inference across a population of patients for which there can be no hard ground truth. A failure of inference here cannot be distinguished from a failure of the intervention, and if the inferential approach is never questioned, replication will not correct the error but typically entrench it. It is striking that whereas absence of evidence is understood not to constitute evidence of absence, negative RCTs are widely interpreted as conclusive proof of a lack of meaningful therapeutic effect⁵⁴, for provided the trial has been correctly conducted, no other outcome is assumed to be possible⁹.

Addressing this urgent question requires semi-synthetic simulations where the space of hypothetical treatment–outcome relationships is comprehensively surveyed with as much biological constraint as the problem permits. If we can show that one inferential approach is superior to another—*across the broadest accessible space of hypothetical possibility*—we need not have evaluated any *specific* relationship for our conclusions plausibly to generalize across the field. Here we therefore combine the largest and most diverse collection of stroke lesion anatomical maps ever assembled with functional³⁴, genetic expression³⁵, and receptor distribution³⁶ maps drawn from the largest accessible data scales, and evaluate the treatment–outcome relationships across the full range of magnitudes of treatment and recovery effects. Our analysis spans 103,628,800 prescriptive simulations, involving >72,000 CPU-core hours of computation on a high-performance cluster. Evaluating any specific treatment–outcome relationship—however finely described and empirically corroborated—would not be sufficient, because generalization across arbitrary relationships would remain untested.

Our analysis shows that the expressivity of the representational models used to infer treatment effects has a profound impact on their fidelity, across the surveyed space of hypothetical possibility, irrespective of the representation of the lesion, the functional domain of the deficit, or the source—receptor or genetic expression—of the determinants of treatment responsiveness. The use—near universal in the field—of simple, highly reductive lesion descriptors, such as crude vascular territory, is revealed to be suboptimal. Now that advances in machine learning have made rich representation of stroke lesions easily realisable, failing to model lesion architecture with the granularity the underlying anatomical relationships demand is hard to justify.

The superiority of inference with complex models extends to the setting of confounded treatment allocation such as observational studies inevitably risk. We show that richly expressive models of non-randomized

data are typically superior to simple models of fully randomized data even where strong allocation confounding is present. Though randomization itself is always desirable, it is shown to matter *less* than representational expressivity. Where real-world resourcing or other constraints force a choice between achieving the data scales complex models demand in an observational context vs conducting a RCT with simple methods, the latter may no longer be assumed to be preferable, indeed our findings suggest the contrary. Where real-world feasibility permits it, complex modelling is ideally combined with randomization; equally, an effect drawn from observational data may be subsequently evaluated with randomized, prospectively acquired data from plausibly homogeneous subpopulations. Both approaches, including their combination, need to be considered in the light of real-world constraints.

That there are bound to be aspects of treatment—revascularization, for example—where a therapeutic mechanism may be simple and general enough to be captured with conventional inferential methods does not imply that alternatives should be pursued only where the mechanism is plausibly complex. The critical outcome measure in stroke—as in medicine generally—is the impact on the patient’s life, which is here expressed through the complex interaction between the anatomical patterns of damage and the functional organization of the underlying neural substrate. If one link in the chain of causation requires it, a more flexible inferential approach is desirable overall. Even revascularization requires reference to the structure of the vascular tree, whose intricate organization entails the possibility of complex heterogeneity. In any event, our mechanistic knowledge is rarely, if ever, sufficiently secure to place hard bounds on the requisite model flexibility.

Equally, though we may use a highly compressed representation—a two-dimensional embedding of lesion anatomy, for example—to stratify patients upstream of randomization within an otherwise conventional RCT, the loss of fidelity in the compression must be balanced against the gain in enabling randomization. Representation learning dependent on large-scale data would be required anyway, for the quality of the embedding is likely to be at least as dependent on data scale as a discriminative model of comparable flexibility. It is highly unlikely that overt—rather than latent—low-dimensional descriptors can commonly be found, for no (say) blood-borne signal could plausibly capture anatomically distributed information.

Though model compactness should be encouraged, the objective to be maximized here is generalizable prescriptive fidelity, not interpretability. The representational machinery we use permits the visualization of latent lesion archetypes (Supplementary S4 & S5), grounding prescriptive recommendations in an anatomically meaningful “lexicon”. Our extremely randomized trees-based prescriptive models, though highly flexible, also offer feature importances, explicitly quantifying the influence that each lesion component exerts on the prescription. Note there is no clear ethical basis for preferring a low-fidelity, readily interpretable model over a higher fidelity, comparatively opaque one. In any event, the matter cannot be settled without soliciting the views of patients and the public at large, to whom this choice has never been presented.

Unmodelled heterogeneity is not merely a statistical nuisance, limiting our power to infer the prescription associated with the greater probability of a favourable outcome at the individual level. It has consequences for medical equity, for where a failure of inference affects a distinct subpopulation, systematic epistemic inequity is introduced⁵⁵. That the disadvantaged may here be identified by multiple interacting factors—creating diverse, intersectional groups—and that the defining factors may lie outside recognized protected characteristics, does not make the resultant inequity any less significant. Medicine has a duty to maintain equity across all, regardless of the basis for their identity.

Medicine also has a duty to make the maximum use of the knowledge it draws from individual patients, often at some discomfort to them, and always at a cost to someone. For treatments already in widespread use, individually prescriptive systems can be built on—and delivered through—established clinical streams. Not only may such systems render the process of individual prescription objective and easily scalable beyond specialist centres, they enable fine-tuning to local populations, including in response to dynamic changes over time. Note that the relevant features of ischaemic stroke—discrete spatial signals with high contrast-to-noise ratio on routine diffusion-weighted imaging—are comparatively invariant to the imaging instrument, and easy to project into standard stereotactic space, rendering the modelling pipeline readily implementable. Indeed, our study exclusively uses clinical data collected in the course of routine practice, drawn from a wide diversity of scanners and image sequence types.

Though stroke is caused by anatomically organised damage to the brain, its outcomes are not exclusively determined by anatomy. A wide array of additional factors contribute to treatment outcome heterogeneity, placing varying demands on the expressivity of the models needed to capture them. The same approach can, and should, be extended beyond the anatomical domain. How readily any factor may be captured will, of course, vary, and there will inevitably be residual variation inaccessible to any practicable model. But the question of whether a factor is material to outcomes, and modellable within a given regime, requires investigation within the kind of framework demonstrated here.

Finally, in common with all inference, our framework depends on foundational assumptions about the nature of the underlying causal relationships and their accessibility to imperfect observation. Inference here, as elsewhere, must always be qualified, and no model may be assumed to be the best, only more or less credibly better than another. Our approach leaves a great deal of room for further optimization it is the task of future studies to explore. But if the complexity of the brain, in both health and disease, is now undeniable, so ought to be the direction in which prescriptive models must evolve to deliver personalized, equitable care.

Methods

Indexing individuals by $i = 1, \dots, n$, each participant in our virtual trials is represented by a tuple (\mathbf{x}_i, w_i, y_i) defined as follows.

1. The phenotype characterization is denoted by $\mathbf{x}_i \in \mathbb{R}^d$, for the range of dimensionalities, d , from 2 to 50.
2. The allocated binary treatment is denoted by $w_i \in \{A, B\}$.
3. The observed binary outcome is denoted by $y_i \in \{0, 1\}$. Here, 1 is the favourable outcome and 0 is the unfavourable outcome.

This constitutes a biologically plausible observational dataset, $\{(\mathbf{x}_i, w_i, y_i)\}_{i=1}^n$, with manipulable values of allocation confoundedness, and observational noise in the form of fixed treatment and recovery effects. Each (\mathbf{x}_i, w_i, y_i) is assumed to be sampled i.i.d. from some distribution $\mathbb{P}(\mathbf{X}, W, Y)$. Here, and henceforth, we model each of these random variables respectively as belonging to the same probability distribution, but with different parameters (for this reason, there are no subscripts on \mathbf{X}, W or Y).

We follow the Neyman–Rubin causal modelling framework^{37,56}. Each individual has two potential outcomes, $Y_i^{(A)}$ and $Y_i^{(B)}$, caused by receiving treatment A or B, respectively. Given wholly empirical data, only one potential outcome is observed and therefore the individual treatment effect, $\tau_i := Y_i^{(A)} - Y_i^{(B)}$, cannot be evaluated. The optimal treatment, w_i^* , cannot be evaluated either. The advantage of our semi-synthetic virtual trials is that each of these quantities is known, enabling evaluation of the prescriptive inference. In the following sections we describe the data-generating process for the virtual trial data.

Patient population

Patients attending the University College London Hospitals NHS Foundation Trust hyperacute stroke service undergo diffusion weighted imaging (DWI) within 24 hours of presentation where feasible as part of the clinical routine. We used irrevocably anonymized magnetic resonance imaging data from unselected patients with an admission diagnosis—both clinical and radiological—of acute ischaemic stroke. This dataset comprises 4,119 irrevocably anonymized DWI from 2,830 unique patients. Where multiple images of a patient were available, only those ≥ 30 days apart were used, ensuring—given the duration of DWI positivity⁵⁷—that each image represented a new lesion. Supplementary S3 shows a CONSORT-2010 flow chart of the recruitment process. The age and sex distributions are shown in Supplementary S8. Beyond basic demographics, no other characteristics, or observed outcomes, were collected or modelled, for we are concerned with modelling counterfactual, unobserved outcomes given virtual, yet to be identified, interventions. A proportion of the data reported here has been used in previous studies^{17–19,41,58}.

Image processing & lesion segmentation

The UNETR transformer segmentation model⁵⁹, a variant of the U-Net convolutional neural network that has been tailored to volume segmentation, was used to automatically segment the lesions in each DWI. The architecture comprises a stack of transformers as the encoder, connected to the decoder through skip connections. The training dataset contained 1,803 DWI with b1000, chosen for the high contrast between acute stroke lesions and the surrounding brain tissues. From this dataset, 1,256 images comprised a group for manual validation, a subset documented in the published study by Mah et al¹⁸ and 547 images were segmented using a simpler U-Net model and then manually corrected by a neurologist (PN) experienced in the task. All (b0, b1000) pairs were non-linearly registered to the MNI template, where the b1000 was co-registered to the b0, and resliced to 2 mm³ resolution⁵⁸. The resultant volumes were 91 × 109 × 91. Five UNETR models were trained, each time using a different division of the dataset into a training set (80% of the data) and a validation set (20%). The best-performing model was selected for further use. Both the Dice similarity coefficient and binary cross-entropy were used to train the model. The Dice similarity coefficient alone was used to evaluate the performance on the validation set.

The signal intensities were normalized to the range 0–1. CoordConv⁶⁰ channels were concatenated to each image, to provide spatial context to the convolutional filters. Random data augmentation functions were used to improve the

generalization of the model further. These functions included histogram transformations, small affine and elastic transformations, and midline reflections.

Disconnectome representation

Ischaemic lesions do not substantially discriminate between tissue classes. Their impact on grey matter functional parcellations is ideally quantified not only by grey matter damage but also by the grey matter disconnections white matter damage incurs. For each lesion in the dataset, a disconnectome representation was therefore generated, providing a probabilistic distribution of affected tissue, including grey matter, resulting from focal ischaemia.

We employed the Disconnectome Map method from BCBtoolkit to achieve this⁴⁰. Individual-level white matter connectivity is not available at the necessary data scale. Furthermore, the long acquisition times necessary for white matter tractography renders it infeasible in the acute setting, and relying on it would introduce a bias against scanning-intolerant patients. In conformity with established practice^{61,62} we therefore used a reference dataset of healthy participants' tractographies. For each lesion mask, segmented as described, the white matter fibres passing through the lesion were tracked for each of 178 healthy tractographies⁴¹, computed from the Human Connectome Project 7T diffusion imaging dataset⁶³. 178 binary disconnection masks were obtained, from which a probabilistic disconnectome map was derived for each patient. This map shows, for each voxel, the proportion of individuals in the healthy dataset that have white matter connections to the lesion.

Compressed data-driven lesion representations

Image volumes, whether lesion masks or disconnectomes, contain many redundant variables arising from the characteristic distribution of ischaemic damage. Redundancy harms computational efficiency and model stability. Creating compressed, concise representations shorn of redundancy furthermore allows explicit control over the richness of the lesion representation, allowing us to quantify the value of its descriptive detail. Since the optimal method of representation for this data is unknown: we tested a range of methods, including principal component analysis (PCA)⁵⁰, non-negative matrix factorization (NMF)⁴⁹, and volume deep auto-encoders (standard (AE) and variational (VAE))⁴⁸. We independently evaluated downstream models employing each method. A VAE was used in addition to an AE because the Bayesian prior has a regularizing effect on the representation.

Each model was trained and validated using 10-fold cross-validation. The 2,830 lesion–disconnectome pairs, constituting each individual's earliest image acquisition, were divided randomly into 10 training:validation splits. All images were assigned once to a test set. The remaining images were then randomly distributed across the 10 training sets, ensuring that data from the same patient never appeared in both compartments of a training:validation split. Each representation method was evaluated with embedding dimensionalities 2, 5, 10, 15, 20, 25, 30, 35, 40, 45, 50.

Principal component analysis

The standard implementation of PCA from SciKit-Learn⁶⁴, with default parameters was used. PCA is limited to capturing linear relations, but admits a closed form solution. The principal components for ischaemic mask lesion archetypes are visualized in Supplementary S4.2. The principal components for disconnectome archetypes are visualized in S5.2.

Non-negative matrix factorization

The use of NMF in this setting is well established¹⁷. The Nimfa library⁶⁵, with 'random vcol' initialization was used. Visualizations for lesion archetypes are shown in Supplementary S4.1 and for disconnectome archetypes in S5.1.

Deep auto-encoders

The AE's encoder was composed of four layers of three-dimensional ResNet-type convolutional blocks, followed by fully connected layers. The decoder used the same architecture, in reverse. The VAE's architecture was the same, except the encoder produced the mean and standard deviation of the m -dimensional posterior latent distribution. Samples were drawn from the VAE's posterior with the reparameterization trick⁴⁸. A batch size of 10 was used. We

trained for a minimum of 16 epochs, and a maximum of 32. If the loss failed to improve for 4 consecutive epochs then training was terminated early.

Atlas-based lesion representations

We created a set of baseline representations from simple vascular territories of the kind commonly used in stroke studies⁶⁶. Liu et al. describe atlases of vascular territories with varying levels of arterial tree specificity⁵¹. The territories indexed by the simplest arterial map were supplied by the anterior or posterior arterial systems⁶⁷. They also provide⁵¹ a specific atlas including the territories supplied by specific major arteries: anterior cerebral artery, middle cerebral artery, posterior cerebral artery and vertebrobasilar artery. The baseline representations were computed by identifying the occluded artery, as the lateralized vascular territory that overlapped the most with the lesion representation, as measured by Dice.

Functional deficit modelling

Our virtual trials begin with recruitment, where participants are selected based on the overlap between their ischaemic stroke lesion segmentation and a functional-anatomical network. These networks are parcellated into anatomical regions such that, if sufficiently lesioned, a corresponding functional deficit is modelled to be present. The deficit itself was derived by agglomerative clustering of open source meta-analytic data from the neurological and neuroscientific literature, compiled by NeuroQuery³⁴, as visualized in Figure 4. The process is outlined below.

Functional parcellation

The NeuroQuery³⁴ dataset consists of predicted neural activation maps, where voxel intensities are z-scores describing the association at that point in MNI space with a specific n-gram drawn from a large corpus of neuroscientific papers. Each image volume comprised $46 \times 55 \times 46$ voxels at 4 mm^3 resolution in MNI space. Volumes associated with n-grams that could not be plausibly associated with cognitive and behavioural functions were manually excluded, leaving 2,095 n-grams for analysis. A binary grey matter mask was generated by thresholding the grey matter tissue probability map⁶⁸ at 0.2. To match the template space of the functional data, nearest neighbour resampling was used to reshape this 1.5 mm^3 $121 \times 145 \times 121$ mask to $46 \times 55 \times 46$ voxels, leaving 21,410 nonzero voxels. Grey matter was selected to isolate neural substrates plausibly associated with functional deficits caused by lesions. White matter (dis)connectivity was incorporated downstream using disconnectome analysis to infer probabilistic estimates of additional disrupted grey matter resulting from each lesion⁴¹. The grey matter voxels from the 2,095 selected NeuroQuery volumes were reshaped into a 2095×21410 matrix. Each column represented a grey matter voxel, and each row quantified the functional association with each of the neuroscientific terms.

We applied agglomerative clustering to the 21,410 columns⁶⁹, grouping voxels hierarchically based on their functional dependence. Distance between clusters was correlated with functional dissimilarity. Agglomeration of voxels was then performed by adjusting the critical distance threshold, forming clusters of voxels according to their functional similarity (Figure 4), without consideration of spatial relations. A custom program was developed for rapid post-hoc manipulation of the distance threshold. Voxels from discrete connected components of volumes $< 4^3$ voxels were reclassified using K-nearest neighbours ($K = 5$) to mitigate the risks of potential low-effect size artefacts resulting from underlying noise. Figure 4 shows the functional parcellation at ten different levels of the hierarchy. Supplementary S1 shows further visualizations of the 16-group functional parcellation. The parcellation will be made available in Neuroimaging Informatics Technology Initiative (NIfTI) format.

The n-grams associated with each of the 16 functional networks respectively were recovered by computing similarity metrics with the NeuroQuery volumes³⁴, giving a ranking of functional similarity for each network. For each network, the n-grams ranked in the top ten had a coherent functional theme (Supplementary S2). A summary functional theme for each was manually determined on inspection of this list. Where functional-anatomical associations were expected—given the neuroscientific literature e.g. memory–hippocampi—these were corroborated by the automatic n-gram rankings.

Ground truth modelling

The availability of both factual and counterfactual outcomes in our virtual trials enables us to fully evaluate the prescriptive inference. With real data alone this is impossible due to the *fundamental problem of causal inference*^{27,37}. Our virtual trial data combines real patient data with empirically-informed patterns of treatment responsiveness. Given this semi-synthetic ground truth, we can simulate both random and non-random treatment allocation policies, with corresponding observational outcomes. An individualized prescription can then be inferred from probabilistic models of outcomes conditioned on treatment. These prescriptions can then be evaluated using the virtual ground truth, which would otherwise have been partially unobserved.

Each network in the 16-group functional parcellation is divided into two subnetworks. The subdivision, described in the following section, is based on neurotransmitter receptomes³⁶ or genetic transcriptomes³⁵ (Supplementary S9 & S10). This yields two targets for treatment that could plausibly be differentially modulated by our virtual treatments. The modelling of treatment targets in this manner allows us to synthesize virtual trial data, where each individual's responsiveness to a virtual treatment can be determined by the overlap of these subnetworks with the lesion anatomy. Note the treatment targets were based on plausible anatomical-physiological structure, rather than any specific established therapeutic process or molecular identity.

The probabilistic disconnectome representations were binarized at 0.5. The voxel-wise dot-product between each binary lesion representation and each of the 32 responsive-determining subnetworks was computed. If this measure of overlap exceeded 5% of the volume of each subnetwork, the lesion was designated as responsive to the corresponding treatment. This threshold is within the range of critical damage thresholds considered by Mah et al¹⁸. In this way, we generate the data for the virtual trials from the 16 functional networks, with both lesion masks or disconnectomes, and responsiveness informed by meta-analytic neurotransmitter receptor or genetic transcription distributions. The tables describing the sample sizes, separability and overlap are available in Supplementary S6.

Neurotransmitter receptome

Hansen et al³⁶ conduct a large-scale analysis of neurotransmitter organization within the human neocortex. Their analysis was based on positron emission tomography (PET) data, collected from >1200 healthy individuals. Radiotracers were administered that targeted 19 neurotransmitter receptors, across 9 systems: 5-hydroxytryptamine (5HT), dopamine, noradrenaline, histamine, acetylcholine (ACh), cannabinoid, opioid, glutamate and γ -aminobutyric acid (GABA).

To determine the preponderance of the receptor distributions within each functional network, we computed the Dice similarity coefficient between the binarization of each network and the group-average of PET image z-scores for each receptor. This was performed at both the level of the specific receptor subtypes, and at the level of the neurotransmitter system. For each functional network, voxels were assigned to whichever of the two most preponderant receptor types (Supplementary S9) had the greatest z-score. This generates contrasting subnetwork pairs describing plausible treatment targets that can be differentially modulated.

Genetic transcriptome

The Allen Institute provides microarray ribonucleic acid (RNA) data with an "all genes, all structures" approach, sampled across six cadaveric adult control brains³⁵. Aggregating these data yielded 3,702 samples, across 58,691 genes per sample. The spatial co-ordinates of each sample site were supplied in MNI space.

For each of the functional networks, samples located within each network mask were selected and then agglomeratively clustered into two groups according to their microarray RNA data⁶⁹. This provides support for a subdivision based on molecular *dissimilarity*. The microarray data do not cover every grey matter voxel in the brain. With unobserved values set to 0, the volumes were convolved with a Gaussian kernel, to provide smooth estimates of the unobserved values. The standard deviation of the kernel was optimized to simultaneously balance the two classes while minimizing the number of connected components. The functional subnetworks acquired from this method are visualized in Supplementary S10. Note the objective here was to derive plausible spatial distributions of responsiveness, as far as available data allows.

Treatment response heterogeneity

The preceding steps yielded an array of functional networks spanning the entire brain, with two sets of anatomical–physiological subdivisions each, admitting plausible patterns of heterogeneous treatment responsiveness. Each lesion representation that surpassed the 5% threshold with respect to at least one of the treatment-responsive subnetworks was included in virtual trial simulations. Some lesions were responsiveness to both virtual treatments, and therefore had no ‘optimal’ treatment. These lesions were excluded from balanced accuracy computations, but not precision-in-estimation-of-heterogeneous-effects, PEHE³², because PEHE penalizes the model for inferring superiority given equivalent treatments.

The virtual trial data derived from transcriptome and receptome subnetworks enable us to evaluate the model in the presence of heterogeneous responses to treatment, within cohorts presenting with observable functional deficits. The evaluation uses semi-synthetic observational data, with non-random treatment allocation and response noise specified using hyperparameters, as described in the following sections.

Modelling treatment allocation policies

Estimates of treatment outcomes can be degraded by biases in the data. RCTs mitigate treatment–outcome confounding. For example, if a patient is more likely to receive a treatment in the context of severe disease associated with worse outcomes, a naïve comparison against those who do not receive the treatment will be contaminated by the confounding effects of disease severity. Observational data is especially prone to treatment–outcome confounding, as treatments are typically guided by prior beliefs about their efficacy. We must therefore evaluate the impact of confounding—as well as the expressivity of the lesion representation—in our simulation framework, so that its effect on prescriptive inference can be estimated.

Observable confounding

We used the co-ordinates of the lesion centroid to simulate the treatment–outcome confounding effects, as virtual treatment responsiveness varies with location. For each pair $[A, B]$ of response-determining subnetworks, we computed the centroid of A, $(c_{x,A}, c_{y,A}, c_{z,A})$, and the centroid of B, $(c_{x,B}, c_{y,B}, c_{z,B})$. The axis along which the two centroids differ the most is then calculated, as $\text{argmax}(|c_{x,A} - c_{x,B}|, |c_{y,A} - c_{y,B}|, |c_{z,A} - c_{z,B}|)$. For each pair $[A, B]$, the lesion representations are then arranged in increasing order of the centroid co-ordinate along this axis.

For the k th lesion of the ordered list, the corresponding probability with which treatment B is allocated rather than treatment A is the k th element of the vector $\boldsymbol{\rho} = \text{linspace}(0.5 - b_{obs}, 0.5 + b_{obs}, N)$. Here, N is the number of participants, and the degree of confounding is controlled by the confounding hyperparameter $b_{obs} \in [0, 0.5]$. If $b_{obs} = 0$, each patient has an equal probability of allocation to treatment groups A or B, effectively simulating a RCT. We allocate treatments differently for $b_{obs} \in (0.5, 1]$. In this case, the extremes of the ordered data are allocated deterministically depending on their relation to the training set median.

Unobservable confounding

An additional mechanism was implemented to model allocation to treatment by unobserved factors. By unobserved factors, we mean features not predictable from the phenotype characterisation, \mathbf{x}_i . This mechanism makes treatment allocation depend on true treatment responsiveness, w^* —allocation is now sampled from a Bernoulli distribution, with probability $\mathbb{P}(W = w^*) = b_{un_obs}$. Here, b_{un_obs} is the hyperparameter that determines the degree of unobservable confounding.

Response noise with fixed treatment and recovery effects

The causal inference literature distinguishes recipients of treatments whose outcome is independent of treatment, as ‘doomed’ and ‘immune’⁷⁰. In our experiments we vary the probability that participants are designated as ‘doomed’, using a fixed treatment effect (TE) hyperparameter, where $\text{TE} = \mathbb{P}(Y = 1 \mid W = w^*)$. This is the probability that there is a favourable outcome, $Y = 1$, given an individually suitable treatment allocation, $W = w^*$. We use an additional hyperparameter to designate participants as ‘immune’, using a fixed recovery effect (RE) hyperparameter, where $\text{RE} = \mathbb{P}(Y = 1)$. This is the probability of a favourable outcome. A synthetic ground truth with $\text{TE} = 1$ and $\text{RE} =$

0 would therefore have no response noise, with all patients responding according to whether their stroke phenotype is responsive to the intervention that they were allocated to receive.

Prescriptive inference

Problem setup

It is common to replace the individualized treatment effect, τ_i , with the conditional average treatment effect⁷¹ (CATE). This is defined as $\hat{\tau}(\mathbf{x}_i) := \mathbb{E}[Y_i^{(A)} - Y_i^{(B)} \mid \mathbf{X} = \mathbf{x}_i]$. We can estimate the CATE, based on the following set of assumptions: the interventions are sufficiently well-defined (consistency); the allocation to treatment depends only on observed covariates (conditional exchangeability); and the probability of receiving each available treatment is non-zero across all individuals (positivity)^{39,72}.

When these assumptions are satisfied, the CATE is referred to as *identifiable*, i.e. it can be estimated⁷¹. We experiment with values of the TE, RE and treatment–outcome confounding that stretch these assumptions to breaking point. The experiments involve simulated noise levels that exist in real healthcare data⁷³. Simulating observable confounding illuminates the effect of stressing conditional exchangeability, while simulating *unobservable* confounding illuminates the effect of its violation. Extreme confounding weakens positivity/overlap, making some individuals highly likely to be allocated to one treatment over the other. When the hyperparameter that controls confoundedness is 1, allocation becomes deterministic, and we observe the effect of invalidating positivity.

Given these three assumptions, we can estimate the CATE as the difference between two probabilities:

$$\begin{aligned} \hat{\tau}(\mathbf{x}_i) &= \mathbb{E}[Y_i^{(A)} \mid \mathbf{X} = \mathbf{x}_i] - \mathbb{E}[Y_i^{(B)} \mid \mathbf{X} = \mathbf{x}_i], \text{ linearity,} \\ &= \mathbb{E}[Y_i^{(A)} \mid W = A, \mathbf{X} = \mathbf{x}_i] - \mathbb{E}[Y_i^{(B)} \mid W = B, \mathbf{X} = \mathbf{x}_i], \text{ cond. exchangeability,} \\ &= \mathbb{E}[Y_i \mid W = A, \mathbf{X} = \mathbf{x}_i] - \mathbb{E}[Y_i \mid W = B, \mathbf{X} = \mathbf{x}_i], \text{ SUTVA \& consistency,} \\ &= \mathbb{E}[Y \mid W = A, \mathbf{X} = \mathbf{x}_i] - \mathbb{E}[Y \mid W = B, \mathbf{X} = \mathbf{x}_i], \text{ equal distributions,} \\ &= \mathbb{P}(Y = 1 \mid W = A, \mathbf{X} = \mathbf{x}_i) - \mathbb{P}(Y = 1 \mid W = B, \mathbf{X} = \mathbf{x}_i), \text{ binary outcome.} \end{aligned}$$

Here, the final two probabilities are realized using supervised learning: decision trees, Gaussian processes and logistic regression.

Assumptions in more detail

Consistency means that, if $W_i = A$ then $Y_i = Y_i^{(A)}$, and if $W_i = B$ then $Y_i = Y_i^{(B)}$. It also implies that the treatment is always applied in the same manner (e.g. the same dose and route of drug administration). In some of the causal modelling literature, an assumption of stable unit treatment value assumption, or SUTVA, is stated, conveying the same condition. This further makes explicit the underlying assumption of independence between units: that one individual’s receipt of a treatment has no effect on another individual’s treatment allocation, also encapsulating the concept of no variation within defined treatments.

Conditional exchangeability guarantees the absence of unobserved confounders (sometimes referred to as *unconfoundedness*). The potential outcomes, $Y^{(A)}$ and $Y^{(B)}$ are independent of the treatment allocation, W , given the phenotype characterisation, \mathbf{X} , i.e. $Y^{(A)} \perp W \mid \mathbf{X}$ and $Y^{(B)} \perp W \mid \mathbf{X}$. This is also referred to as *ignorability*. The randomization of treatment in RCTs promotes conditional exchangeability⁷⁴.

Positivity, or *overlap*, means that before allocation, both treatment allocation probabilities are non-zero, encouraging inclusion of data relating to both treatments across subpopulations: $0 < \mathbb{P}(W = w \mid \mathbf{X} = \mathbf{x}) < 1$ for all w, \mathbf{x} . This is sometimes referred to as strong ignorability.

Prescriptive inference

We infer treatment effects using two frameworks from the causal inference literature^{29,31,75–77}. The one-model/Slearner⁷⁵ framework involves modelling $\mathbb{P}(Y = 1 \mid W = w, \mathbf{X} = \mathbf{x})$ using a single outcome classifier, fitted to pairs (\mathbf{x}, δ_w^A) , where δ_w^A is the Kronecker delta, which equals 1 when $w = A$ and 0 otherwise. The optimal treatment is then inferred to be the treatment with the greatest corresponding probability.

The two-model/TLearner⁷⁵ approach employs two separate outcome-predicting classifiers. The first classifier is fitted to the participants allocated to treatment A; the second to treatment B. For each unseen individual and each treatment, the probability of causing a favourable outcome is computed from the corresponding model. The optimal treatment is then inferred to be the treatment with the greatest corresponding probability.

Models

We used the following range of contrasting architectures for the one-model/SLearner and two-model/TLearner: extremely randomized trees⁴⁴, random forest⁴³, Gaussian process⁴⁷, XGBoost⁴⁵ and logistic regression⁴⁶, from SciKit-Learn⁶⁴ and the XGBoost⁴⁵ Python packages, each with default parameter settings.

Model evaluation

The fidelity of the prescriptive inference was assessed with balanced accuracy and PEHE. In all cases, we use 10-fold cross-validation and report validation set accuracies. The training:validation splits were selected randomly at the start, before any models were fitted. In particular, the splits were selected before the phenotype characterisations were computed. The prescriptive inference was evaluated on the validation sets only.

Model evaluation: balanced accuracy

Balanced accuracy is only computed for virtual trial participants who are responsive to treatment A or B, but not both. This was computed as the mean of the proportions where the preferable treatment was correctly inferred. We reported most of our performance results in terms of balanced accuracy because most of our virtual trials involved class imbalance.

Model evaluation: precision in estimation of heterogeneous effects (PEHE)

The PEHE^{32,78} is a continuous quantification of the CATE estimation. It was computed across all virtual trial participants in each validation set. The participants included those responsive to both treatments equally ($\tau_i = 0$). This allowed us to evaluate whether the model could indeed infer responsiveness to both treatments. The measure was computed as $\sqrt{\frac{1}{N_{val}} \sum_{i=1}^{N_{val}} (\hat{\tau}(\mathbf{x}_i) - \tau_i)^2}$, for N_{val} validation set participants. The CATE, $\hat{\tau}$, was computed as the difference of two supervised learning model predictions, as described in *Problem setup*.

Comparison

While the PEHE is usefully a continuous measure of *predictive* performance, the balanced accuracy measures how closely the inferred *prescription* matches the optimal prescription. This is the question that motivates our work. For this reason, we include PEHE only for completeness.

Low-dimensional representations, \mathbf{x}_i , were used as a baseline in our experiments. They were derived from the affected vascular territories arising from the broad anterior or posterior arterial systems, as described in *Atlas-based lesion representations*. This distinction, between anterior and posterior vascular occlusion, is incorporated in the UK clinical guidance as a factor influencing the decision between the acute ischaemic stroke treatments of mechanical thrombectomy or intravenous thrombolysis⁶⁶. This baseline was computed with unconfounded allocation, as a surrogate for RCTs. When comparisons were made to this baseline, treatment effect and recovery effect were kept equal. This is because randomization does not control for these features of interventions.

Prescriptive performance, with phenotype characterisation, \mathbf{x}_i , derived from ischaemic lesion masks was presented separately from \mathbf{x}_i derived from disconnectomes. These results were summarized using their aggregate mean, and contrasted using independent sample two-sided t -tests. Superiority was determined using the critical p -value, computed using the Benjamini–Hochberg method⁷⁹. The false discovery rate reflected 0.05 significance level.

Data availability

Functional grey matter parcellations including their subdivided versions will be made available after publication. Neuroimaging data cannot be released publicly owing to the terms of access to clinical data specified in the ethical approval.

Code availability

Will be made available after publication.

References

1. Deaton, A. & Cartwright, N. Understanding and misunderstanding randomized controlled trials. *Social Science & Medicine* vol. 210 2–21 (2018).
2. Mulder, R. *et al.* The limitations of using randomised controlled trials as a basis for developing treatment guidelines. *Evid. Based Ment. Health* **21**, 4–6 (2018).
3. Rothwell, P. M. Subgroup analysis in randomised controlled trials: importance, indications, and interpretation. *The Lancet* **365**, 176–186 (2005).
4. Luedtke, A. R. & van der Laan, M. J. Evaluating the impact of treating the optimal subgroup. *Stat. Methods Med. Res.* **26**, 1630–1640 (2017).
5. Kessler, R. C., Bossarte, R. M., Luedtke, A., Zaslavsky, A. M. & Zubizarreta, J. R. Machine learning methods for developing precision treatment rules with observational data. *Behav. Res. Ther.* **120**, 103412 (2019).
6. VanderWeele, T. J., Luedtke, A. R., van der Laan, M. J. & Kessler, R. C. Selecting optimal subgroups for treatment using many covariates. *Epidemiology* **30**, 334–341 (2019).
7. Wardlaw, J. & Warlow, C. Thrombolysis in acute ischemic stroke: does it work? *Stroke* **23**, 1826–1839 (1992).
8. Rothwell, P. M. External validity of randomised controlled trials: “to whom do the results of this trial apply?” *The Lancet* **365**, 82–93 (2005).
9. Sackett, D. L., Rosenberg, W. M., Gray, J. M., Haynes, R. B. & Richardson, W. S. Evidence based medicine: what it is and what it isn’t. *Bmj* vol. 312 71–72 (1996).
10. Feigin, V. L. *et al.* Global, regional, and national burden of stroke and its risk factors, 1990–2019: a systematic analysis for the Global Burden of Disease Study 2019. *Lancet Neurol.* **20**, 795–820 (2021).
11. Vos, T. *et al.* Global burden of 369 diseases and injuries in 204 countries and territories, 1990–2019: a systematic analysis for the Global Burden of Disease Study 2019. *The Lancet* **396**, 1204–1222 (2020).
12. Smith, W. S. *et al.* Mechanical thrombectomy for acute ischemic stroke: final results of the Multi MERCI trial. *Stroke* **39**, 1205–1212 (2008).
13. Wardlaw, J. M., Murray, V., Berge, E. & Del Zoppo, G. J. Thrombolysis for acute ischaemic stroke. *Cochrane Database Syst. Rev.* (2014).
14. Langhorne, P., Bernhardt, J. & Kwakkel, G. Stroke rehabilitation. *The Lancet* **377**, 1693–1702 (2011).
15. Bustamante, A. *et al.* Ischemic stroke outcome: a review of the influence of post-stroke complications within the different scenarios of stroke care. *European journal of internal medicine* vol. 29 9–21 (2016).
16. Haak, K. V. & Beckmann, C. F. Understanding brain organisation in the face of functional heterogeneity and functional multiplicity. *NeuroImage* **220**, 117061 (2020).
17. Bonkhoff, A. K. *et al.* Reclassifying stroke lesion anatomy. *Cortex* **145**, 1–12 (2021).
18. Mah, Y.-H., Husain, M., Rees, G. & Nachev, P. Human brain lesion-deficit inference remapped. *Brain* **137**, 2522–2531 (2014).
19. Xu, T., Jha, A. & Nachev, P. The dimensionalities of lesion-deficit mapping. *Neuropsychologia* vol. 115 134–141 (2018).
20. Xie, Y., Brand, J. E. & Jann, B. Estimating heterogeneous treatment effects with observational data. *Sociol. Methodol.* **42**, 314–347 (2012).
21. Giraudeau, B. *et al.* Heterogeneity in pragmatic randomised trials: sources and management. *BMC Med.* **20**, 1–16 (2022).
22. Kent, D. M., Steyerberg, E. & van Klaveren, D. Personalized evidence based medicine: predictive approaches to heterogeneous treatment effects. *Bmj* **363**, (2018).
23. Holmes, M., Davis, S. & Simpson, E. Alteplase for the treatment of acute ischaemic stroke: a NICE single technology appraisal; an evidence review group perspective. *Pharmacoeconomics* **33**, 225–233 (2015).
24. Montaner, J. *et al.* Multilevel omics for the discovery of biomarkers and therapeutic targets for stroke. *Nat. Rev. Neurol.* **16**, 247–264 (2020).
25. White, P. *et al.* Standards for providing safe acute ischaemic stroke thrombectomy services (September 2015). *Clin. Radiol.* **72**, 175–e1 (2017).
26. Nguyen, T.-L., Collins, G. S., Landais, P. & Le Manach, Y. Counterfactual clinical prediction models could help to infer individualized treatment effects in randomized controlled trials—An illustration with the International Stroke Trial. *J. Clin. Epidemiol.* **125**, 47–56 (2020).
27. Holland, P. W. Statistics and causal inference. *J. Am. Stat. Assoc.* **81**, 945–960 (1986).
28. Feuerriegel, S. *et al.* Causal machine learning for predicting treatment outcomes. *Nat. Med.* **30**, 958–968 (2024).
29. Alaa, A. & van der Schaar, M. Limits of estimating heterogeneous treatment effects: Guidelines for practical algorithm design. *International Conference on Machine Learning* 129–138 (2018).
30. Alaa, A. & van der Schaar, M. Bayesian inference of individualized treatment effects using multi-task gaussian processes. *Advances in Neural Information Processing Systems* 3424–3432 (2017).
31. Curth, A. & van der Schaar, M. Nonparametric estimation of heterogeneous treatment effects: From theory to learning algorithms. in *International Conference on Artificial Intelligence and Statistics* 1810–1818 (PMLR, 2021).
32. Hill, J. L. Bayesian Nonparametric Modeling for Causal Inference. *Journal of Computational and Graphical Statistics* vol. 20 217–240 (2011).
33. Lu, M., Sadiq, S., Feaster, D. J. & Ishwaran, H. Estimating Individual Treatment Effect in Observational Data Using Random Forest Methods. *Journal of computational and graphical statistics : a joint publication of American Statistical Association, Institute of Mathematical Statistics, Interface Foundation of North America* vol. 27 209–219 (2018).
34. Dockès, J. *et al.* NeuroQuery, comprehensive meta-analysis of human brain mapping. *Elife* **9**, e53385 (2020).
35. Hawrylycz, M. J. *et al.* An anatomically comprehensive atlas of the adult human brain transcriptome. *Nature* **489**, 391–399 (2012).
36. Hansen, J. Y. *et al.* Mapping neurotransmitter systems to the structural and functional organization of the human neocortex. *Nat. Neurosci.* (2022) doi:10.1038/s41593-022-01186-3.
37. Rubin, D. B. Estimating causal effects of treatments in randomized and nonrandomized studies. *Journal of educational Psychology* vol. 66 688 (1974).
38. Pearl, J. *Causality*. (Cambridge university press, 2009).
39. Hernán, M. A. & Robins, J. M. Causal Inference: What If. (2020).
40. Foulon, C. *et al.* Advanced lesion symptom mapping analyses and implementation as BCBtoolkit. *Gigascience* **7**, giy004 (2018).
41. Thiebaut de Schotten, M., Foulon, C. & Nachev, P. Brain disconnections link structural connectivity with function and behaviour. *Nat. Commun.* **11**, 5094 (2020).
42. Zhu, Y., Hubbard, R. A., Chubak, J., Roy, J. & Mitra, N. Core concepts in pharmacoepidemiology: Violations of the positivity assumption in the causal analysis of observational data: Consequences and statistical approaches. *Pharmacoepidemiol. Drug Saf.* **30**, 1471–1485 (2021).
43. Breiman, L. Random forests. *Mach. Learn.* **45**, 5–32 (2001).
44. Geurts, P., Ernst, D. & Wehenkel, L. Extremely randomized trees. *Mach. Learn.* **63**, 3–42 (2006).
45. Chen, T. & Guestrin, C. XGBoost: A scalable tree boosting system. in *Proceedings of the 22nd ACM SIGKDD international conference on knowledge discovery and data mining* 785–794 (2016).
46. McCullagh, P. *Generalized Linear Models*. (Routledge, 2019).
47. MacKay, D. J. Information theory, inference and learning algorithms. (2003).

48. Kingma, D. P. & Welling, M. Auto-encoding variational bayes. *ArXiv Prepr. ArXiv13126114* (2013).
49. Lee, D. D. & Seung, H. S. Learning the parts of objects by non-negative matrix factorization. *Nature* **401**, 788–791 (1999).
50. Jolliffe, I. T. *Principal Component Analysis for Special Types of Data*. (Springer, 2002).
51. Liu, C.-F. *et al.* Digital 3D Brain MRI Arterial Territories Atlas. *Sci. Data* **10**, 1–17 (2023).
52. Cook, D. *et al.* Lessons learned from the fate of AstraZeneca’s drug pipeline: a five-dimensional framework. *Nat. Rev. Drug Discov.* **13**, 419–431 (2014).
53. Bespalov, A. *et al.* Failed trials for central nervous system disorders do not necessarily invalidate preclinical models and drug targets. *Nat. Rev. Drug Discov.* **15**, 516–516 (2016).
54. Kersten, P., Ellis-Hill, C., McPherson, K. M. & Harrington, R. Beyond the RCT—understanding the relationship between interventions, individuals and outcome—the example of neurological rehabilitation. *Disabil. Rehabil.* **32**, 1028–1034 (2010).
55. Carruthers, R. *et al.* Representational ethical model calibration. *Npj Digit. Med.* **5**, 170 (2022).
56. Neyman, J. S. On the application of probability theory to agricultural experiments. Essay on principles. Section 9. (Translated and edited by DM Dabrowska and TP Speed, Statistical Science (1990), 5, 465-480). *Ann. Agric. Sci.* **10**, 1–51 (1923).
57. Augustin, M. *et al.* Diffusion-weighted imaging of patients with subacute cerebral ischemia: comparison with conventional and contrast-enhanced MR imaging. *Am. J. Neuroradiol.* **21**, 1596–1602 (2000).
58. Xu, T., Rolf Jäger, H., Husain, M., Rees, G. & Nachev, P. High-dimensional therapeutic inference in the focally damaged human brain. *Brain* **141**, 48–54 (2018).
59. Hatamizadeh, A. *et al.* UNETR: Transformers for 3D Medical Image Segmentation. in *Proceedings of the IEEE/CVF Winter Conference on Applications of Computer Vision* 574–584 (2022).
60. El Jurdi, R., Petitjean, C., Honeine, P. & Abdallah, F. CoordConv-Unet: Investigating CoordConv for Organ Segmentation. *IRBM* **42**, 415–423 (2021).
61. Van Essen, D. C. *et al.* The WU-Minn human connectome project: an overview. *Neuroimage* **80**, 62–79 (2013).
62. Maier-Hein, K. H. *et al.* The challenge of mapping the human connectome based on diffusion tractography. *Nat. Commun.* **8**, 1349 (2017).
63. Vu, A. T. *et al.* High resolution whole brain diffusion imaging at 7 T for the Human Connectome Project. *Neuroimage* **122**, 318–331 (2015).
64. Pedregosa, F. *et al.* Scikit-learn: Machine learning in Python. *the Journal of machine Learning research* vol. 12 2825–2830 (2011).
65. Zitnik, M. & Zupan, B. Nimfa: A Python Library for Nonnegative Matrix Factorization. *J. Mach. Learn. Res.* **13**, 849–853 (2012).
66. National Institute for Health and Care Excellence. Stroke and transient ischaemic attack in over 16s: diagnosis and initial management. (2019).
67. Frid, P. *et al.* Detailed phenotyping of posterior vs. anterior circulation ischemic stroke: a multi-center MRI study. *J. Neurol.* **267**, 649–658 (2020).
68. Blaiotta, C., Cardoso, M. J. & Ashburner, J. Variational inference for medical image segmentation. *Comput. Vis. Image Underst.* **151**, 14–28 (2016).
69. Virtanen, P. *et al.* SciPy 1.0: fundamental algorithms for scientific computing in Python. *Nat. Methods* **17**, 261–272 (2020).
70. Greenland, S. & Robins, J. M. Identifiability, exchangeability, and epidemiological confounding. *Int. J. Epidemiol.* **15**, 413–419 (1986).
71. Imbens, G. W. & Wooldridge, J. M. Recent developments in the econometrics of program evaluation. *J. Econ. Lit.* **47**, 5–86 (2009).
72. Imbens, G. W. & Rubin, D. B. *Causal Inference in Statistics, Social, and Biomedical Sciences*. (Cambridge University Press, 2015).
73. De Carlo, V., Calati, R. & Serretti, A. Socio-demographic and clinical predictors of non-response/non-remission in treatment resistant depressed patients: a systematic review. *Psychiatry Res.* **240**, 421–430 (2016).
74. Hernán, M. A. Beyond exchangeability: the other conditions for causal inference in medical research. *Statistical Methods in Medical Research* vol. 21 3–5 (2012).
75. Künzel, S. R., Sekhon, J. S., Bickel, P. J. & Yu, B. Metalearners for estimating heterogeneous treatment effects using machine learning. *Proc. Natl. Acad. Sci.* **116**, 4156–4165 (2019).
76. Shalit, U., Johansson, F. D. & Sontag, D. Estimating individual treatment effect: generalization bounds and algorithms. in *International Conference on Machine Learning* 3076–3085 (PMLR, 2017).
77. Johansson, F. D., Shalit, U., Kallus, N. & Sontag, D. Generalization bounds and representation learning for estimation of potential outcomes and causal effects. *J. Mach. Learn. Res.* **23**, 7489–7538 (2022).
78. Louizos, C. *et al.* Causal effect inference with deep latent-variable models. *Adv. Neural Inf. Process. Syst.* **30**, (2017).
79. Benjamini, Y. & Hochberg, Y. Controlling the false discovery rate: a practical and powerful approach to multiple testing. *J. R. Stat. Soc. Ser. B Methodol.* **57**, 289–300 (1995).

Acknowledgements

Funded by UCLH NIHR Biomedical Research Centre (NIHR-INF-0840) and UKRI EPSRC (2252409). The authors acknowledge the use of the UCL Myriad High Performance Computing Facility (Myriad@UCL), and associated support services, in the completion of this work.

Corresponding authors: Dominic Giles (dominic.giles@ucl.ac.uk) and Parashkev Nachev (p.nachev@ucl.ac.uk).

Inclusion & Ethics Statement

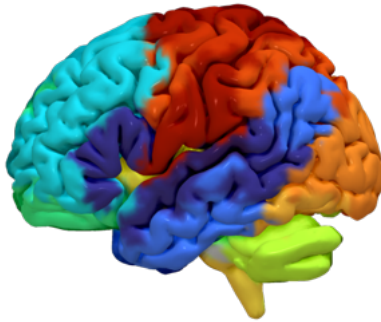
This study was performed under ethical approval by the West London & GTAC research ethics committee for consentless use of fully anonymized data. The data is an unselected sample based on clinical diagnosis of acute ischaemic stroke; no other specific inclusion or exclusion criteria were used. It should therefore be proportionally representative of the acute ischaemic stroke patient population presenting to hospital in London, UK.

Supplementary Material

Fig.	Title	Page
S1	Functional parcellation visualisation	1
S2	Ordered list of neurological terms for each functional network	3
S3	CONSORT 2010 flow diagram of dataset curation	4
S4	Lesion archetypes	5
S5	Disconnectome archetypes	7
S6	Separability, overlap, and sample size for each virtual trial	9
S7	Lesion volume distribution	10
S8	Patient age and sex distributions	11
S9	Neurotransmitter receptome subnetworks	12
S10	Transcriptome subnetworks	45
S11	Lesion representations & location bias results	78
S12	Disconnectome representations & location bias results	83
S13	Lesion representations & unobservable bias results	88
S14	Disconnectome representations & unobservable bias results	93
S15	Prescriptive analysis summary by PEHE	98
S16	Prescriptive analysis summary, stratified by deficit, by PEHE	99
S17	Performance comparison under ideal experimental conditions	100
S18	Glossary	101

S1.1: Functional parcellation surface renders

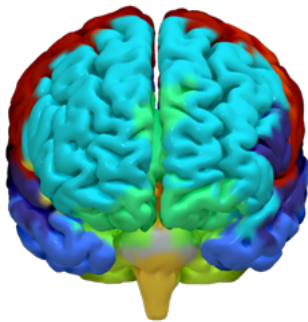
a



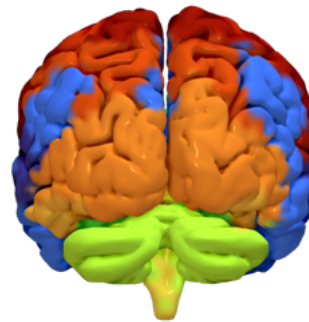
b



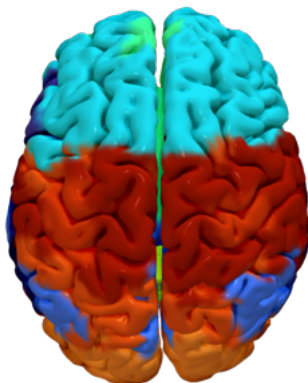
c



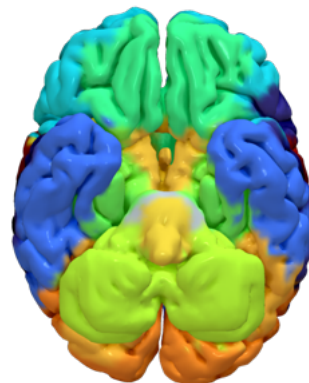
d



e

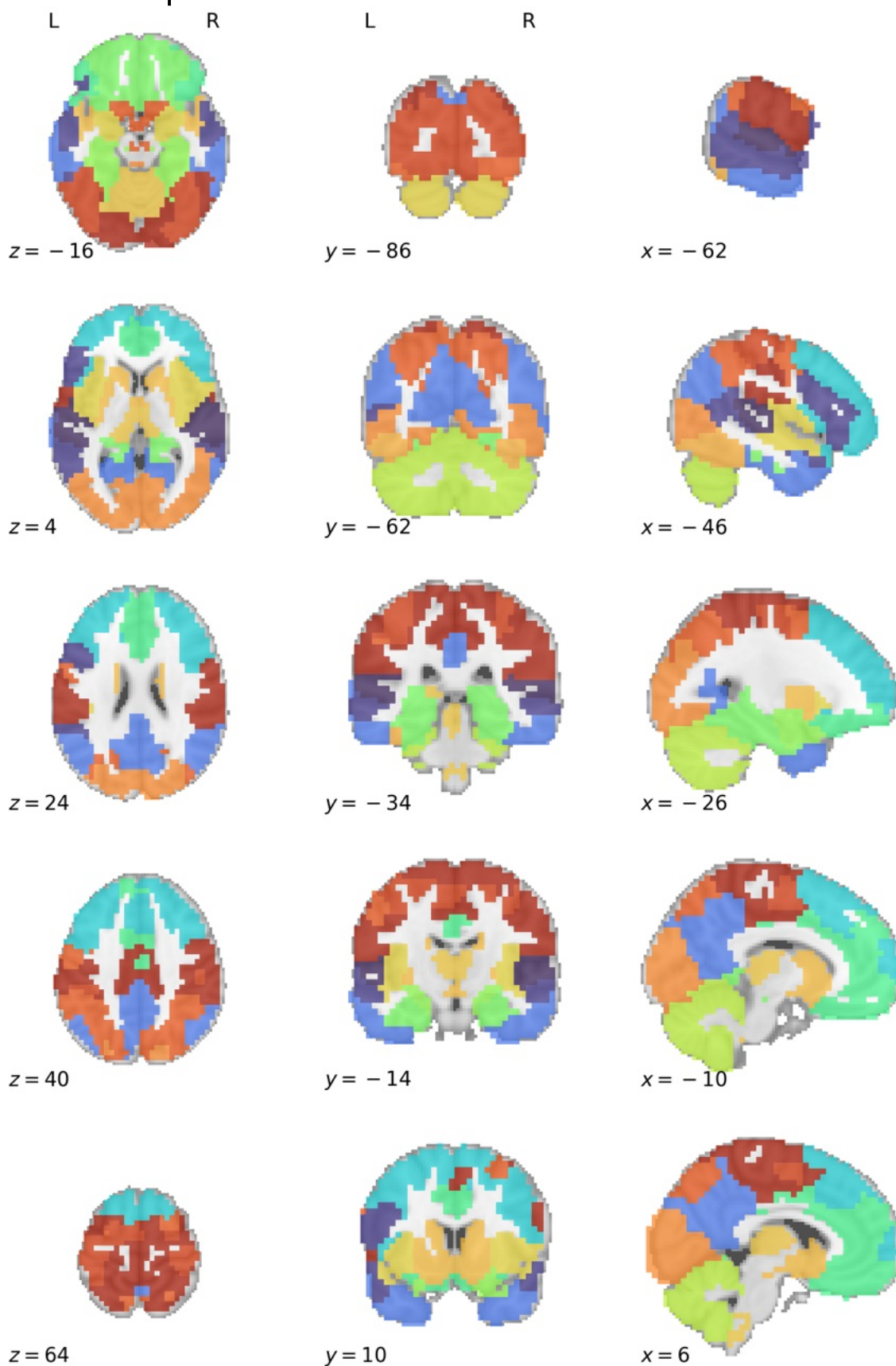


f



Surface rendering of the functional grey matter parcellation, with 16 distinct regions labelled by colour. The same colours are used in Figures 4, S1.2, and S2. The functional categories associated with each region are described in the coloured text of Figures 4, derived from the term lists in Figure S2. Each panel shows the same surface rendering from a different spatial perspective: **a**, left; **b**, right; **c**, anterior; **d**, posterior; **e**, superior; **f**, inferior.

S1.2: Functional parcellation axial slices



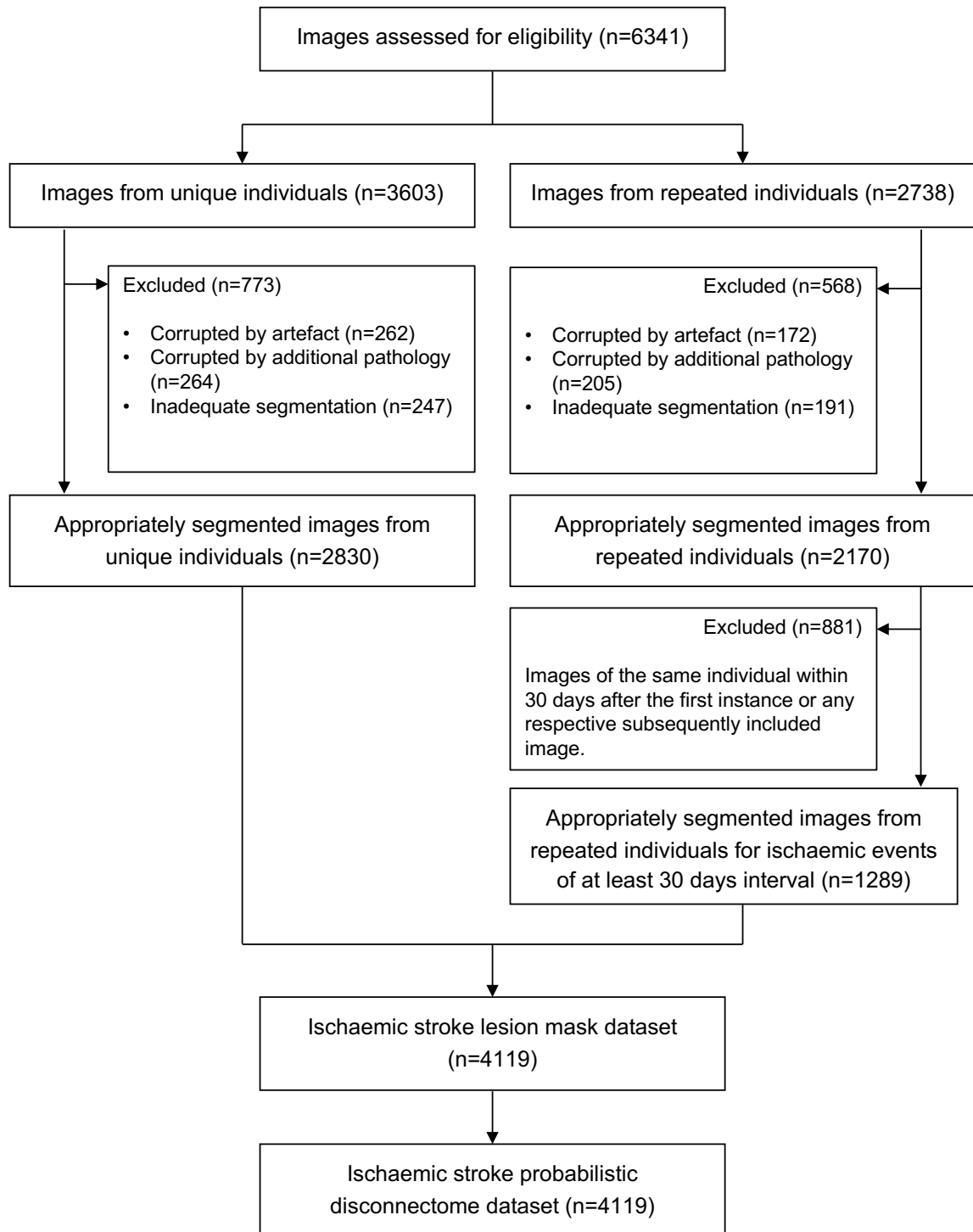
Axial slice visualisation of the functional grey matter parcellation, with 16 distinct regions labelled by colour, overlaid onto the standard MNI152 template. The slice co-ordinates refer to MNI space. The same colours are used in Figures 4, S1.1 and S2. The functional categories associated with each region are described in the coloured text of Figure 4, derived from the term lists in Figure S2.

S2: Ordered list of neurological terms for each functional network

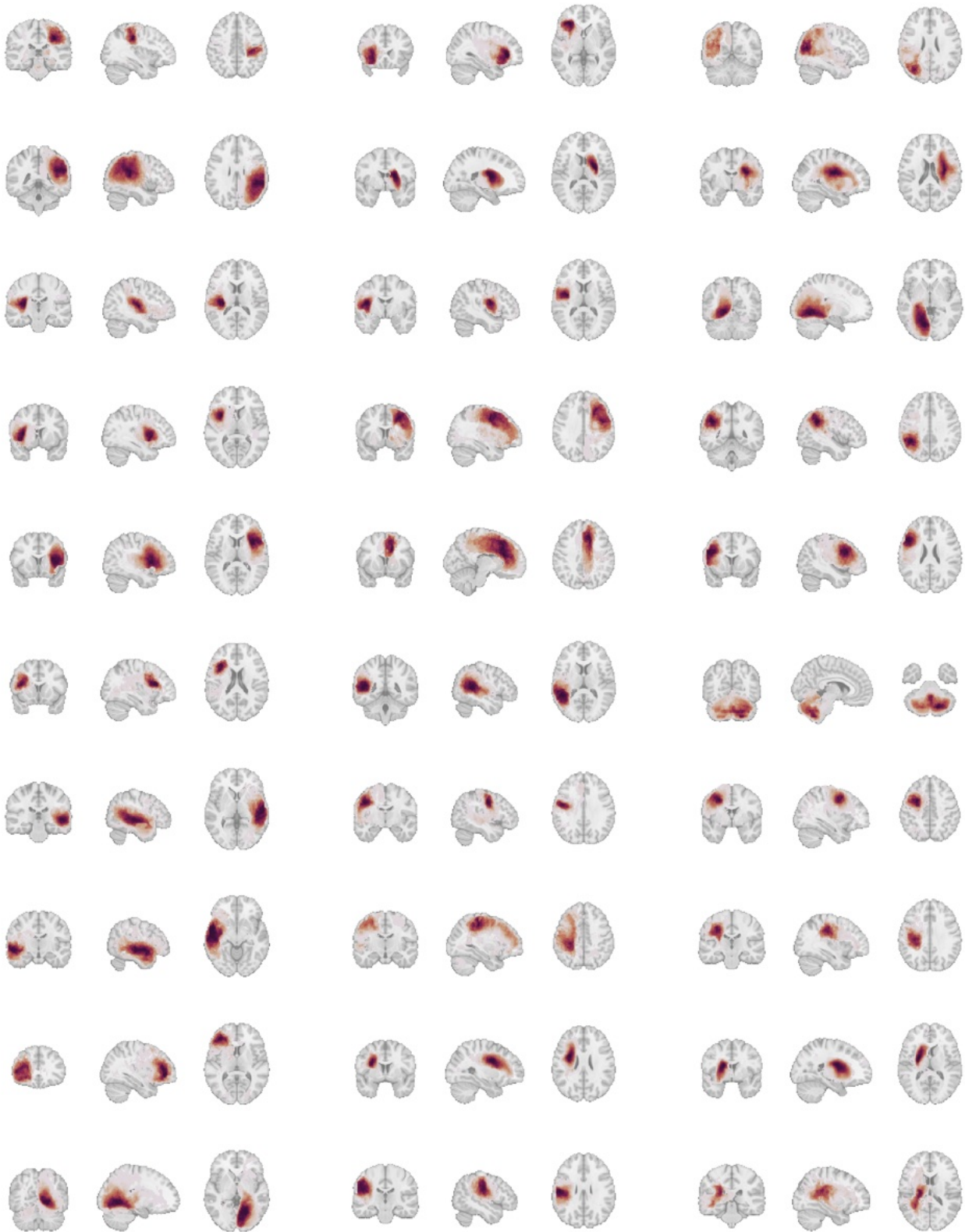
Hearing Auditory feedback Acoustic Auditory perception Acoustic processing Auditory stimuli Auditory stream segregation Vocalisation Hearing loss Melody	Lexical processing Phonological processing Linguistic Story Spoken Auditory sentence comp. Parsing Deafness Lexical Speaker	Self-referential Referential Mind Conscious Rumination Dream Narcissistic Self-control Schizotypal personality dis. Wandering	Sorting Cognitive control Handling Response execution Opiate dependence Primitive Psychological stress Inattentional blindness Reappraisal Punish
Compulsive behaviour Mood Mania Discipline Unipolar depression Reversal learning Suicidability Accountability Hoarding Awakening	Amnesia Novelty detection Active retrieval Spatial memory Spatial navigation Memory loss Navigation Cognitive symptom Encoding Maze	Fearful faces Fearful Temperament Aggressive Emotional stimuli Uninhibited Psychopathic personality Neutral stimuli Bereavement Separation anxiety	Tremor Orthostatic Corneal Dysmetria Incoordination Friedreich ataxia Uvula Gastrocnemius Ataxia Spatial organisation
Feeling Viscerosensory Interoceptive Destructive Hate Shyness Tachycardia Risk processing Gustation Disgust	Cataplexy Slow wave sleep Sleep latency Sleep Slow wave sleep REM sleep Sleep disordered breathing Memory acquisition Circadian rhythm Tiredness	Gratification Negative reinforcement Habit learning Habit Physical anhedonia Love Substance dependence Anhedonia Erotic Instrumental conditioning	Recognition Photographs Facial recognition Visual representation Prejudice Selective Agnosia Viewing Repetition suppression Recognised
Blindness Visual perception Sighted Blind Visual impairment Visual angle Blindsight Ambyopia Form perception Stereoscopic	Calculation Mathematical Visuospatial Mental arithmetic Procedural knowledge Acalculia Cue validity Capacity limitation Arithmetic processing Arithmetic	Flexor Extremity Extensor Finger movements Voluntary Paresis Execution Extension Dressing Isometric	Sensory perception Extremity Count Primary somatosensory Muscle Kinaesthetic Plantar Proprioceptive Embodied Reflex

Ordered lists of the 10 commonest functional labels associated with each grey matter network in the parcellation (as visualized in Figures 4 and S1) by dot product with the original meta-analytic statistical maps from NeuroQuery. The colours are unified with Figure 4 and S1, with the archetypal functional categories manually identified from the above to be: (upper row, left to right) hearing, language, introspection, cognition; (second row, left to right) mood, memory, aversion, co-ordination; (third row, left to right) interoception, sleep, reward, visual recognition and (lower row, left to right) visual perception, spatial reasoning, motor, somatosensory.

S3: CONSORT 2010 lesion dataset flow chart

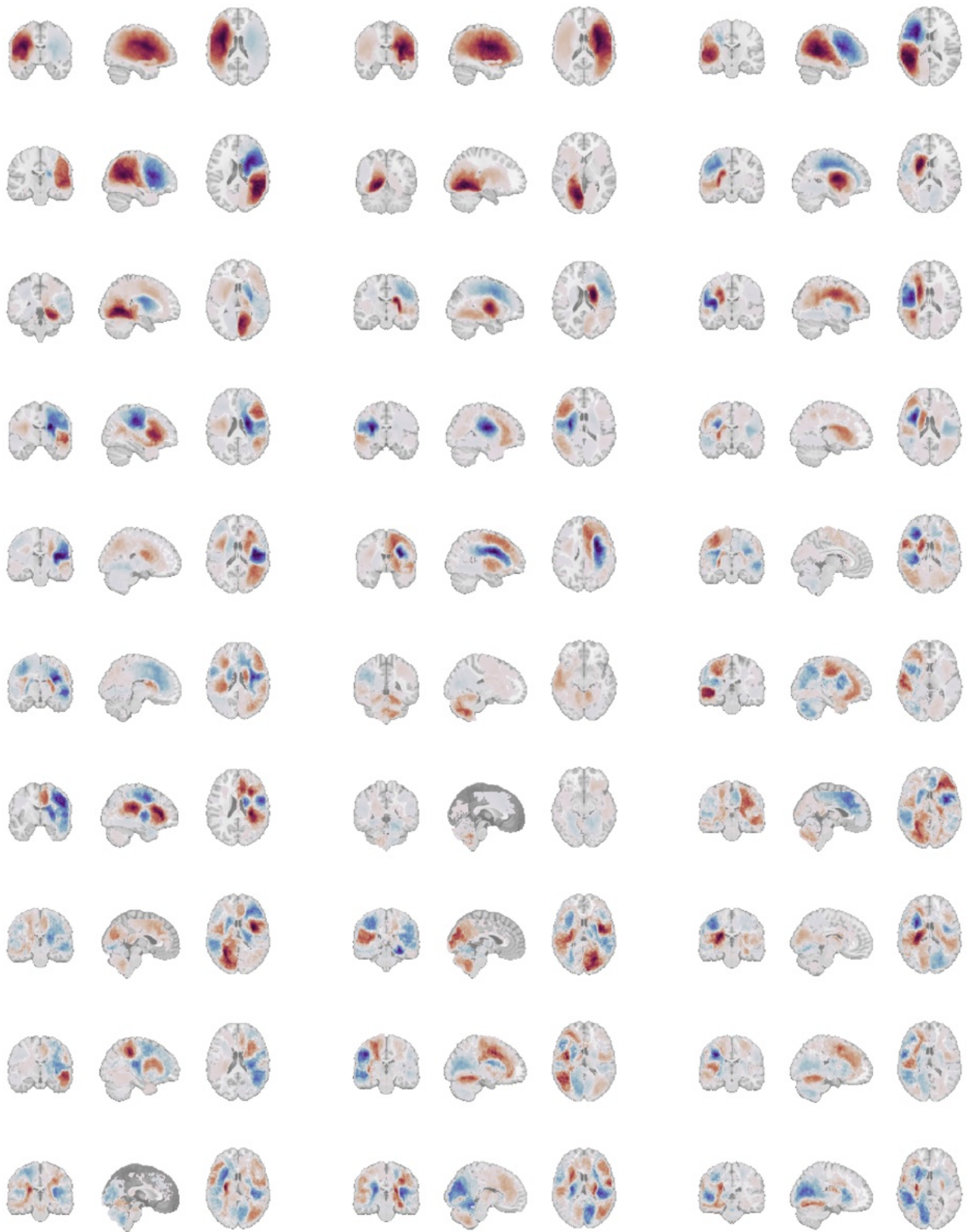


S4.1: Lesion NMF archetypes



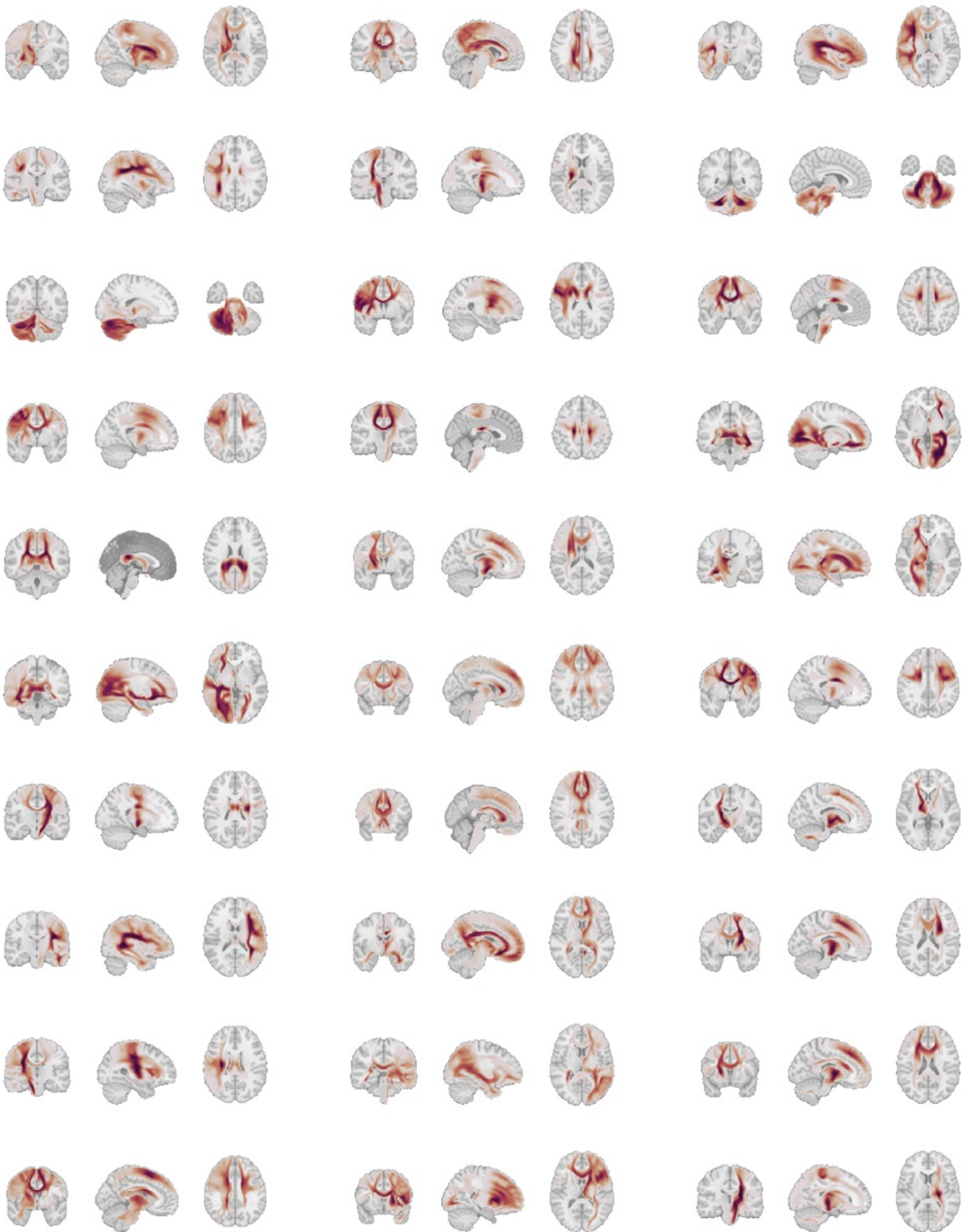
Spatial reconstructions of the latent factors from a 30-dimensional non-negative matrix factorisation of the lesion masks. The spatial distribution of each reconstruction is visualized. Coronal (left), sagittal (centre) and axial (right) slice are shown for each, with co-ordinates set to the location of maximum density.

S4.2: Lesion PCA archetypes



Spatial reconstructions of the latent factors from a 30-dimensional principal component analysis-derived representation of the lesion masks. The spatial distribution of each reconstruction is visualized. Coronal (left), sagittal (centre) and axial (right) slice are shown for each, with co-ordinates set to the location of maximum density.

S5.1: Disconnectome NMF archetypes



Spatial reconstructions of the latent factors from a 30-dimensional non-negative matrix factorisation of the disconnectomes. The spatial distribution of each reconstruction is visualized. Coronal (left), sagittal (centre) and axial (right) slice are shown for each, with co-ordinates set to the location of maximum density.

S5.2: Disconnectome PCA archetypes



Spatial reconstructions of the latent factors from a 30-dimensional principal component analysis-derived representation of the disconnectomes. The spatial distribution of each reconstruction is visualized. Coronal (left), sagittal (centre) and axial (right) slice are shown for each, with co-ordinates set to the location of maximum density.

S6: Linear separability, overlap, & sample sizes

Lesions, N = 4,119, threshold = 0.05

	Receptome				Transcriptome			
	Linear separability		Overlap	N	Linear separability		Overlap	N
	OR	XOR			OR	XOR		
Hearing	0.618	0.985	0.603	305	0.684	0.949	0.506	322
Language	0.567	NaN	0.463	240	0.991	0.991	0	264
Introspection	0.799	0.857	0.309	94	0.739	0.908	0.291	103
Cognition	0.546	0.500	0.321	196	0.653	0.919	0.548	168
Mood	0.593	0.667	0.516	31	0.938	1	0.194	31
Memory	0.580	0.643	0.779	136	0.593	0.954	0.650	157
Aversion	0.603	0.686	0.341	88	0.695	0.780	0.344	96
Coordination	0.816	0.950	0.413	109	0.648	0.883	0.543	105
Interoception	0.623	0.938	0.669	495	0.577	0.903	0.665	487
Sleep	0.702	0.938	0.337	83	0.722	0.908	0.372	102
Reward	0.694	0.900	0.355	304	0.550	0.667	0.039	356
Visual recognition	0.876	1	0.151	86	0.784	0.895	0.190	84
Visual perception	0.762	0.772	0.318	154	0.655	0.950	0.506	176
Spatial reasoning	0.658	0.925	0.594	207	0.819	0.955	0.339	239
Motor	0.737	0.940	0.403	278	0.993	0.993	0.006	324
Somatosensory	0.693	0.902	0.464	267	0.981	0.992	0.009	335

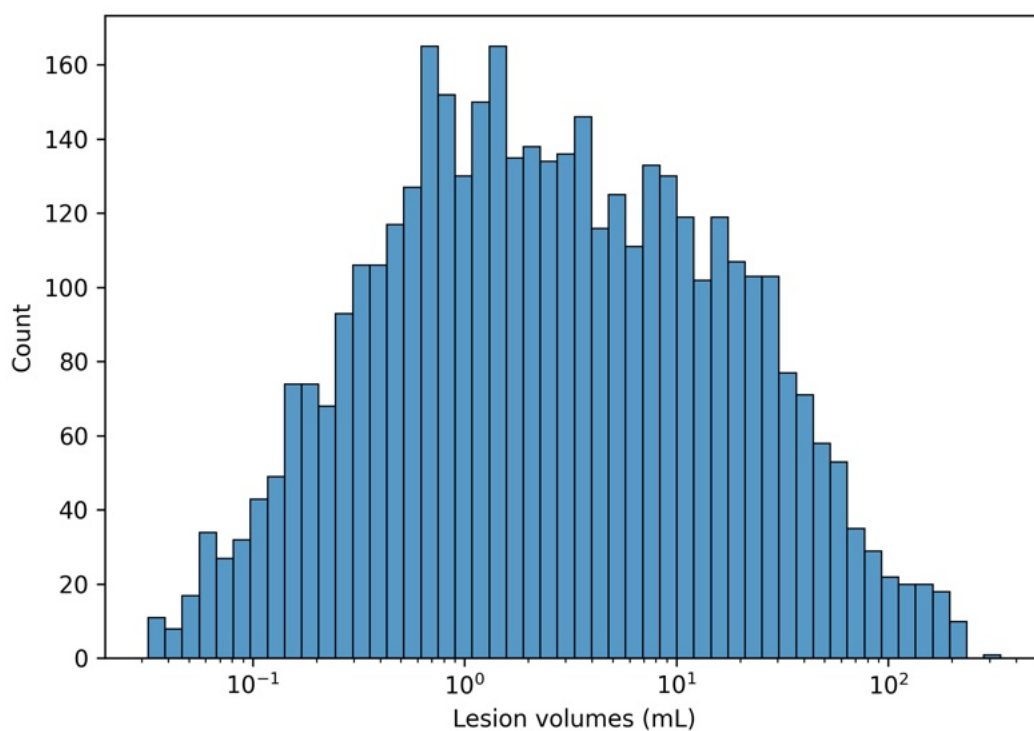
Separability, overlap and sample size characteristics of the virtual cohorts defined by functional subgroup and physiology type for lesion models. The *linear separability* column lists the balanced accuracy of a linear support vector machine trained to distinguish between “affected” and “unaffected” members of each cohort as defined by the intersection of the functional and physiological labels at a threshold of 0.05; the *overlap* column lists the proportion of lesions that exceed the threshold for both hypothetical treatments; and the *N* column lists the total number of patients from the dataset with lesions meeting the threshold for at least one subnetwork.

Disconnectomes, N = 4,119, threshold = 0.05, $p > 0.5$

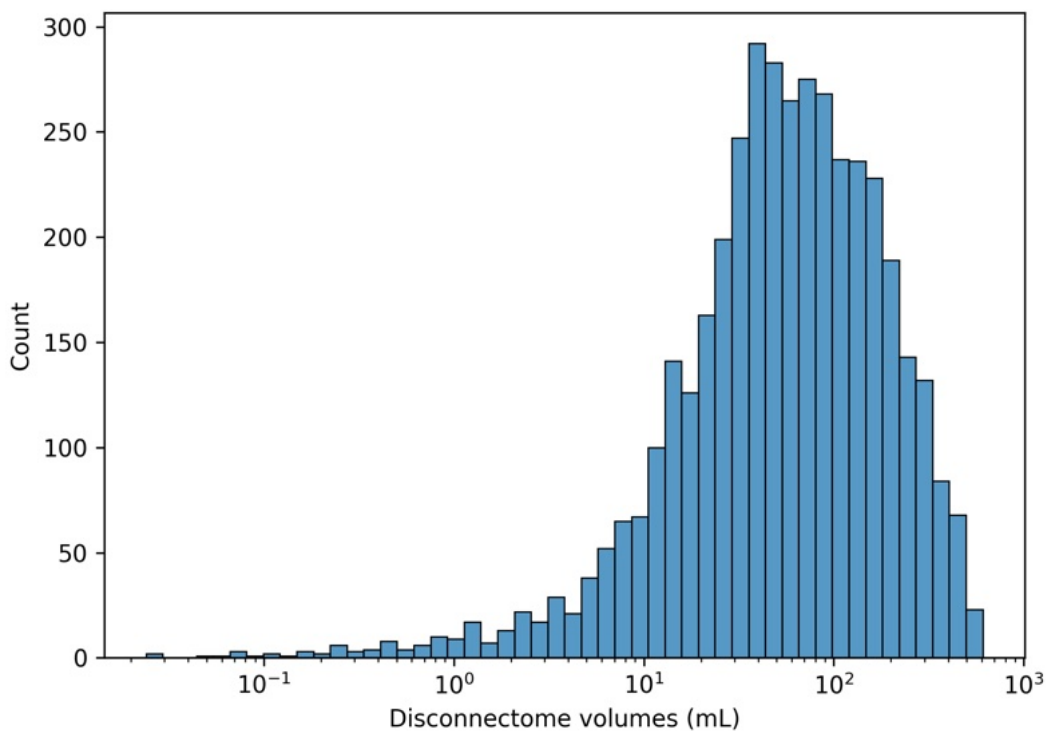
	Receptome				Transcriptome			
	Linear separability		Overlap	N	Linear separability		Overlap	N
	OR	XOR			OR	XOR		
Hearing	0.645	0.987	0.614	868	0.704	0.986	0.512	887
Language	0.593	0.500	0.660	688	0.989	0.998	0.009	851
Introspection	0.666	0.990	0.545	508	0.846	0.990	0.223	637
Cognition	0.574	0.800	0.573	853	0.580	0.982	0.743	829
Mood	0.605	0.988	0.604	364	0.645	0.949	0.588	381
Memory	0.617	NaN	0.409	978	0.566	0.958	0.708	955
Aversion	0.608	0.769	0.645	1503	0.556	0.953	0.800	1346
Coordination	0.529	0.772	0.698	325	0.607	0.943	0.616	378
Interoception	0.554	0.903	0.761	1806	0.583	0.823	0.675	1872
Sleep	0.652	0.939	0.553	3078	0.616	0.993	0.630	2781
Reward	0.629	0.974	0.658	1854	0.660	0.972	0.550	1993
Visual recognition	0.848	0.988	0.167	335	0.838	0.963	0.215	297
Visual perception	0.626	0.843	0.469	407	0.577	0.900	0.234	376
Spatial reasoning	0.662	0.972	0.408	1011	0.714	0.951	0.407	863
Motor	0.697	0.970	0.461	1230	0.903	0.998	0.157	1394
Somatosensory	0.700	0.966	0.452	1202	0.905	0.999	0.158	1427

Separability, overlap and sample size characteristics of the virtual cohorts defined by functional subgroup and physiology type for disconnectome models, where the disconnectome is binarized at a disconnection threshold of 0.5. The *linear separability* column lists the balanced accuracy of a linear support vector machine trained to distinguish between “affected” and “unaffected” members of each cohort as defined by the intersection of the functional and physiological labels at a threshold of 0.05; the *overlap* column lists the proportion of lesions that exceed the threshold for both hypothetical treatments; and the *N* column lists the total number of patients from the dataset with lesions meeting the threshold for at least one subnetwork.

S7: Lesion volume distribution

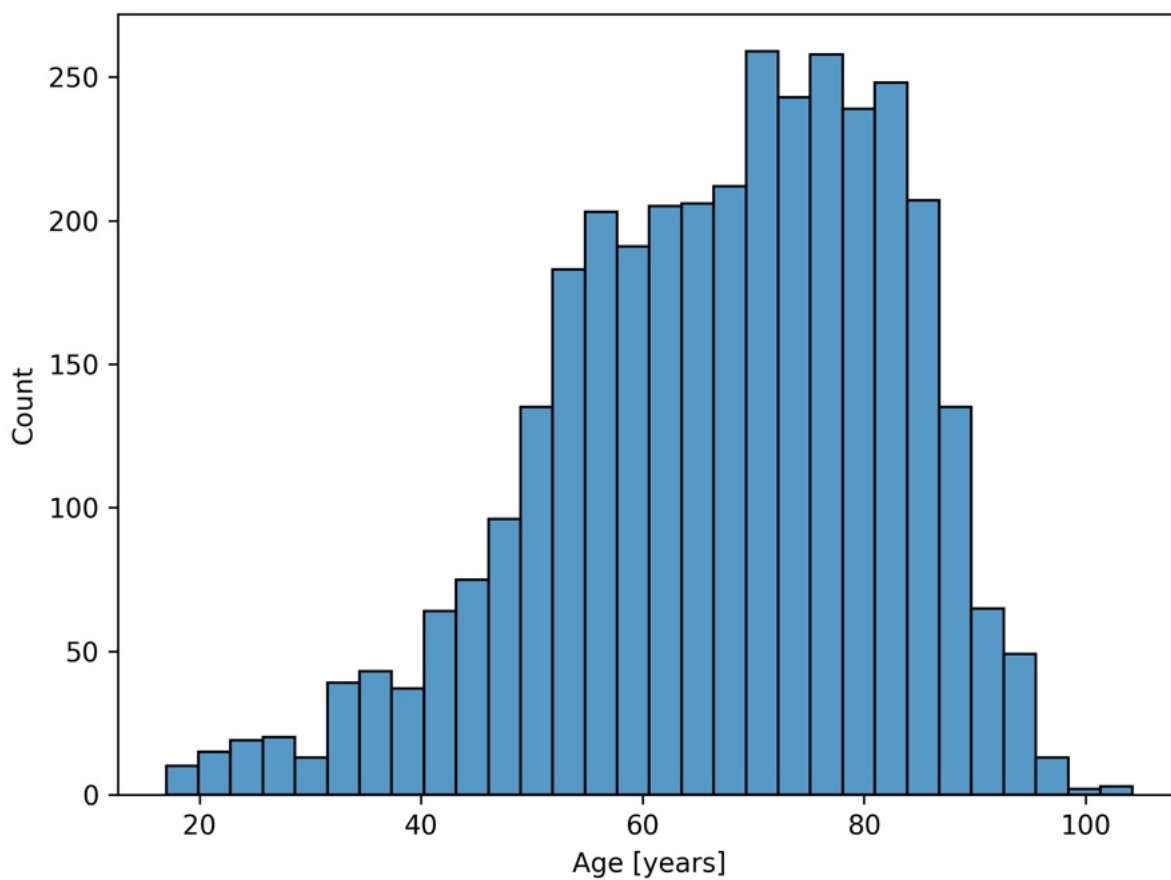


Histogram showing the distribution of lesion volumes for the dataset of 4,119 events, after non-linear registration to MNI space. The mean is 11.68 mL, with standard deviation of 25.49 mL. Note decimal log scale.



Histogram showing the distribution of binarized ($p > 0.5$) disconnectome volumes for the dataset of 4,119 events, after non-linear registration to MNI space. The mean is 94.26 mL, with standard deviation of 101.04 mL. Note decimal log scale.

S8: Patient age distribution



Histogram showing the distribution of patient age. Age data was available for 3487/4119 images and exhibited a mean of 67.042 years and standard deviation 15.46 years. From 3478/4119 images with complete data on patient sex, 1,960 were recorded as male (56.4%) and 1,518 as female (43.6%).

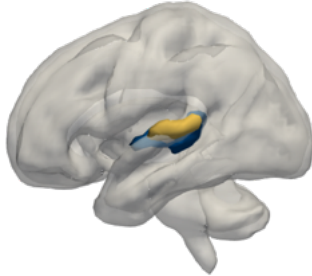
S9: Neurotransmitter receptome subnetworks

Functional Deficit	Primary receptor type	Secondary receptor type
Hearing	Noradrenaline	Glutamate
Language	Cannabinoid	Glutamate
Introspection	Glutamate	5HT
Cognition	Cannabinoid	Opioid
Mood	Opioid	Histamine
Memory	Dopamine	5HT
Aversion	Dopamine	Histamine
Coordination	Opioid	Acetylcholine
Interoception	Dopamine	Histamine
Sleep	Opioid	Noradrenaline
Reward	Dopamine	Histamine
Visual recognition	Cannabinoid	GABA
Visual perception	GABA	5HT
Spatial reasoning	Glutamate	Noradrenaline
Motor	Noradrenaline	Glutamate
Somatosensory	Noradrenaline	Glutamate

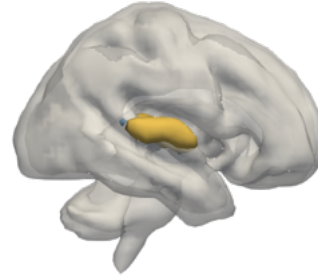
The primary and secondary receptor classes by preponderance within each of the functional networks, according to aggregation of Z-valued transformations of positron emission tomography data, each targeted to receptor subclasses. The preponderance was determined by the proportions of voxels from each functional network whose receptor type aggregated Z-value was maximal (primary) and second-maximal (secondary) over all others. The following figures show, for each functional network, the functional network subdivisions based upon neurotransmitter receptor preponderance, derived from positron emission tomography data made available by Hansen et al. (2022).

S9.1.1: *Hearing* subnetwork render

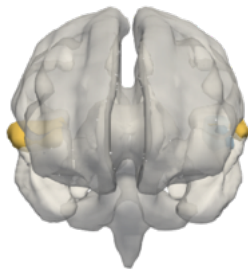
a



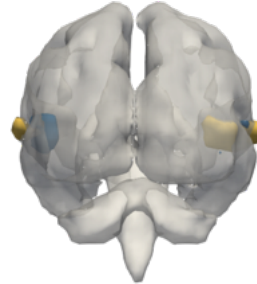
b



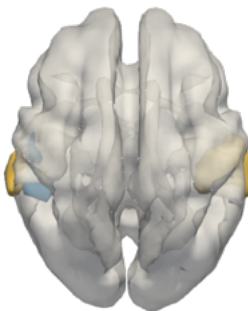
c



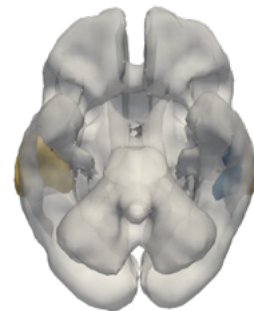
d



e

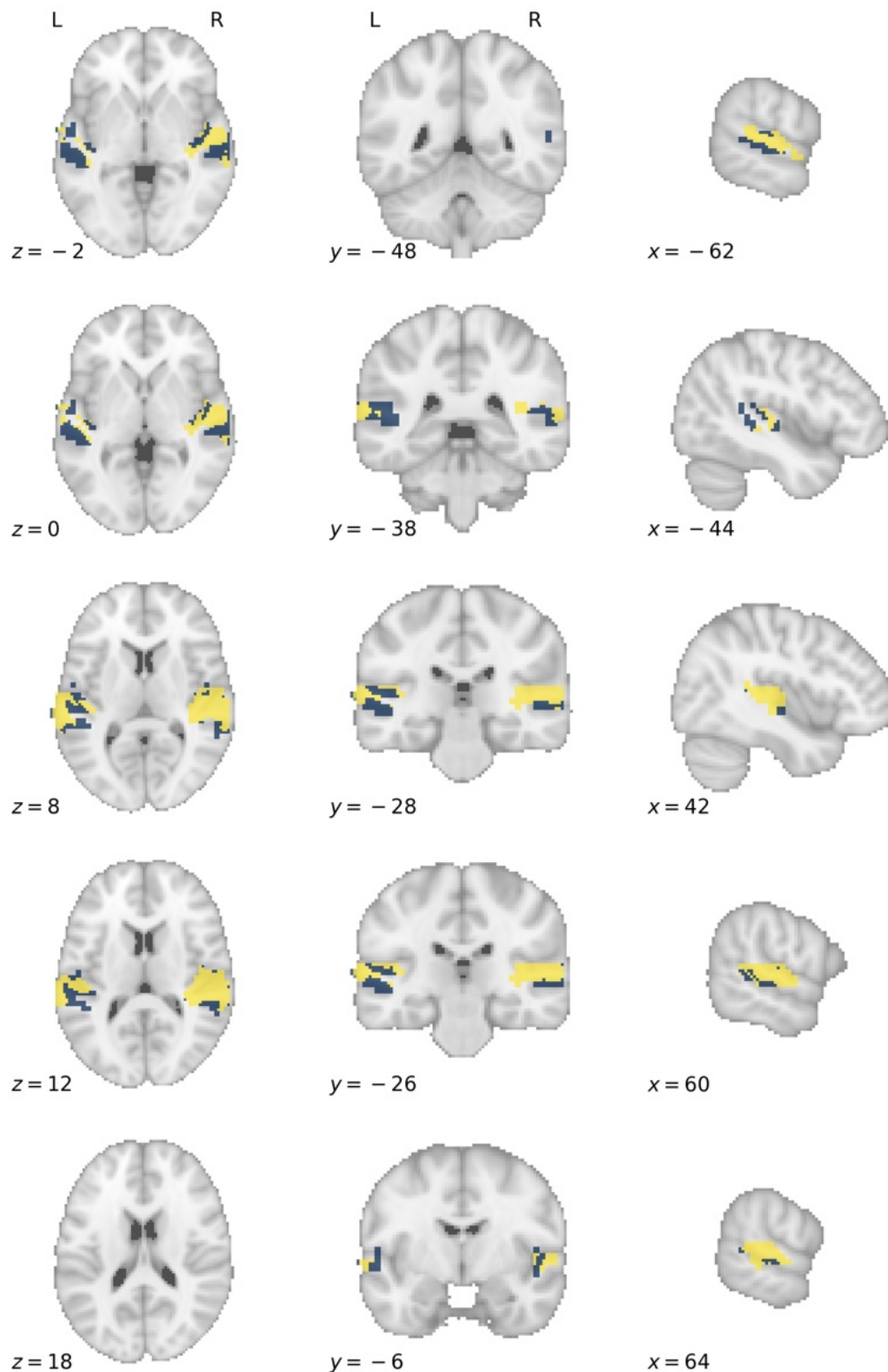


f



Three-dimensional rendering of the functional grey matter network representing *hearing*. The colours label functional subnetworks separated by neurotransmitter receptor distribution preponderance, here noradrenaline in yellow and glutamate in blue. This forms the basis upon which treatment effect heterogeneity is simulated, with hypothetical treatments selectively effective for lesions disrupting defined receptor territories. Each panel shows the same render from a different spatial perspective: **a**, left; **b**, right; **c**, anterior; **d**, posterior, **e**, superior; **f**, inferior. The underlay is a thresholded white matter template surface in MNI.

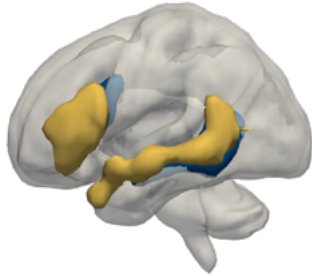
S9.1.2: *Hearing* subnetwork axial slices



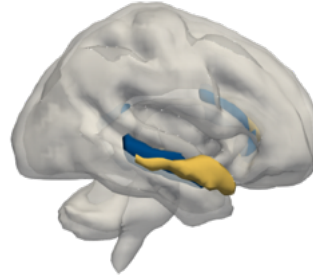
Axial slice visualisation of the functional grey matter network representing *hearing*, overlaid onto the standard MNI152 template. The labelled co-ordinates map to MNI space. The colours label functional subnetworks separated by neurotransmitter receptor distribution preponderance, here noradrenaline in yellow and glutamate in blue. This forms the basis upon which treatment effect heterogeneity is simulated, with hypothetical treatments selectively effective for lesions disrupting defined receptor territories.

S9.2.1: *Language* subnetwork render

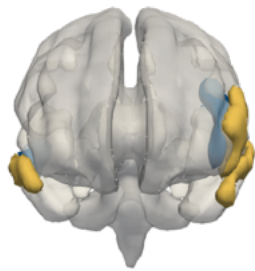
a



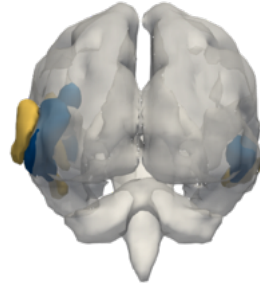
b



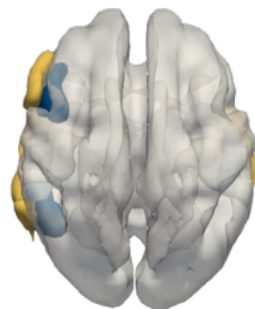
c



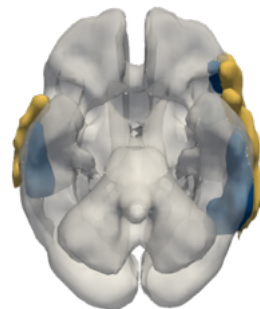
d



e

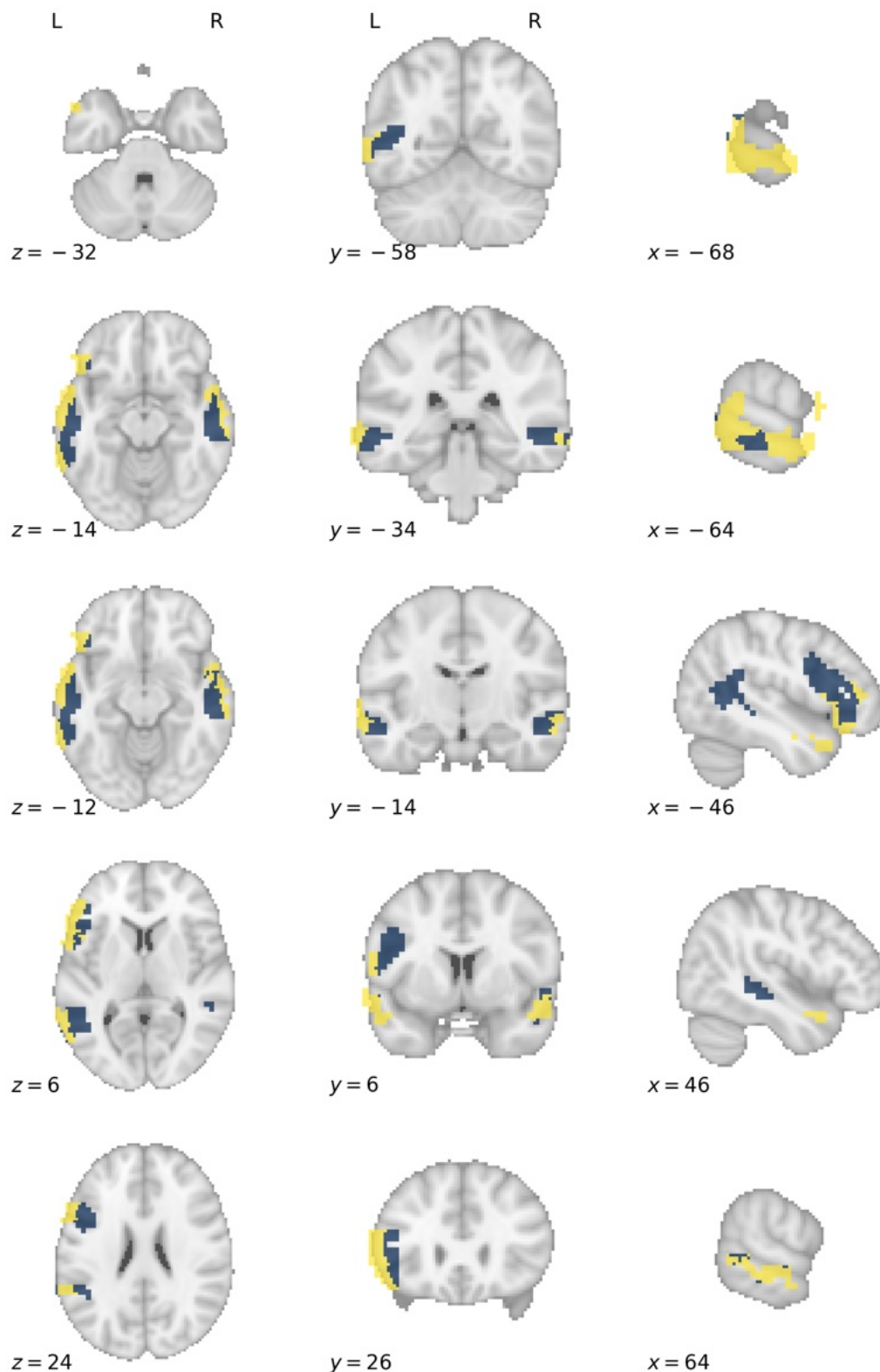


f



Three-dimensional rendering of the functional grey matter network representing *language*. The colours label functional subnetworks separated by neurotransmitter receptor distribution preponderance, here cannabinoid in yellow and glutamate in blue. This forms the basis upon which treatment effect heterogeneity is simulated, with hypothetical treatments selectively effective for lesions disrupting defined receptor territories. Each panel shows the same render from a different spatial perspective: **a**, left; **b**, right; **c**, anterior; **d**, posterior, **e**, superior; **f**, inferior. The underlay is a thresholded white matter template surface in MNI.

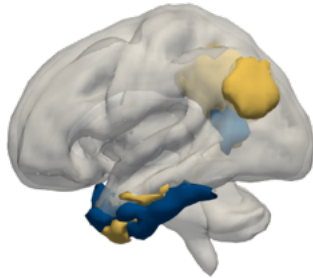
S9.2.2: *Language* subnetwork axial slices



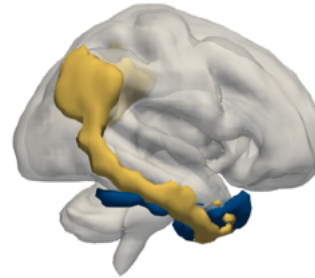
Axial slice visualisation of the functional grey matter network representing *language*, overlaid onto the standard MNI152 template. The labelled co-ordinates map to MNI space. The colours label functional subnetworks separated by neurotransmitter receptor distribution preponderance, here cannabinoid in yellow and glutamate in blue. This forms the basis upon which treatment effect heterogeneity is simulated, with hypothetical treatments selectively effective for lesions disrupting defined receptor territories.

S9.3.1: *Introspection* subnetwork render

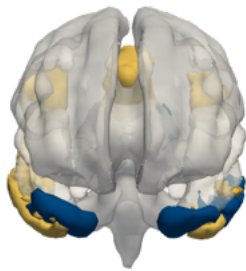
a



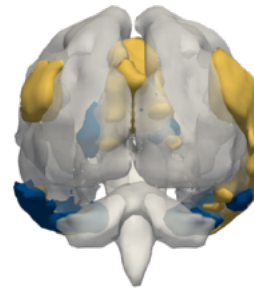
b



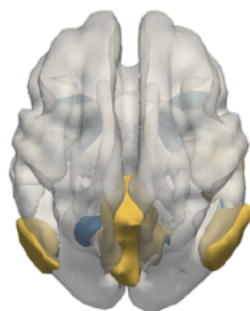
c



d



e

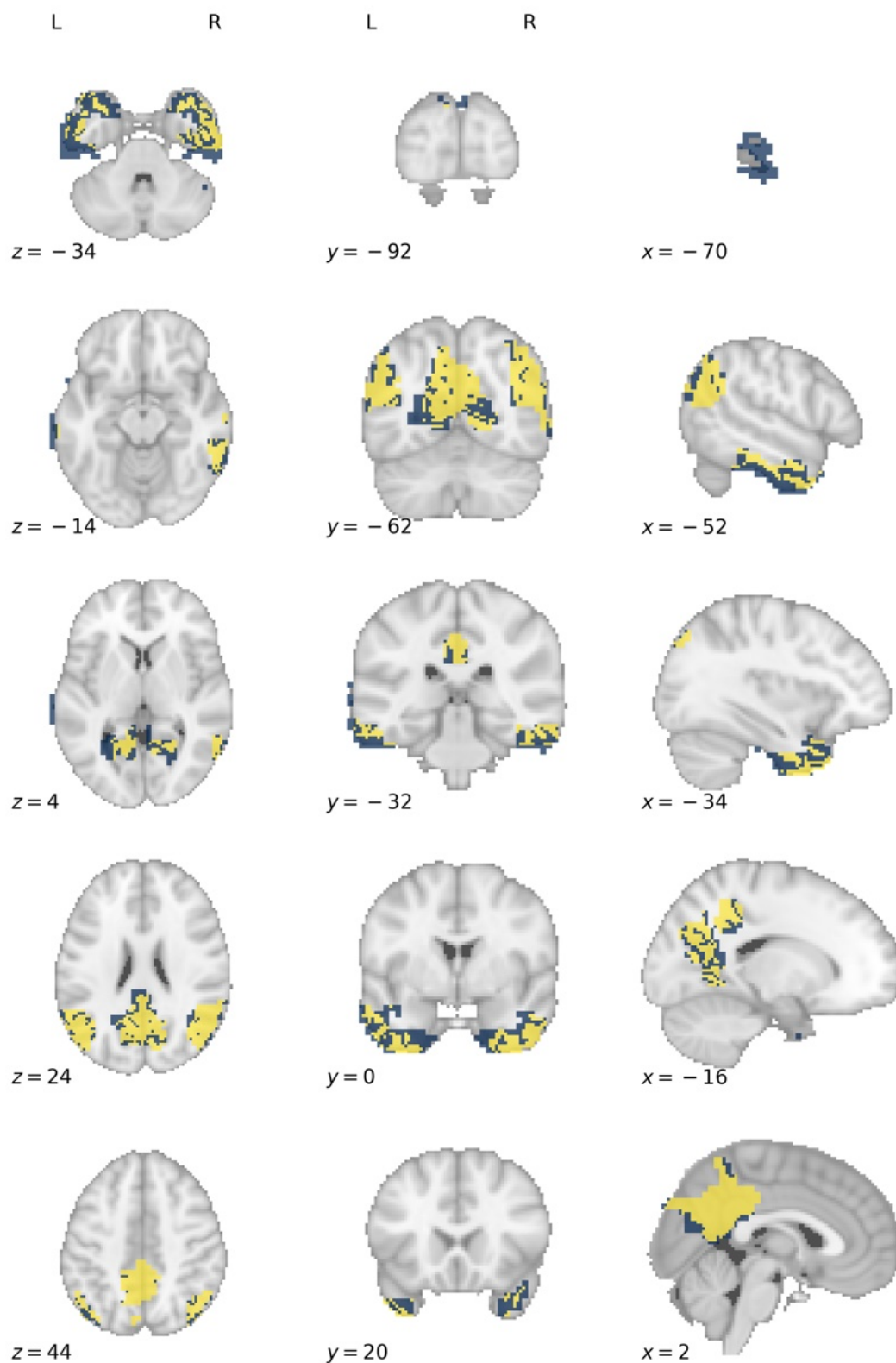


f



Three-dimensional rendering of the functional grey matter network representing *introspection*. The colours label functional subnetworks separated by neurotransmitter receptor distribution preponderance, here glutamate in yellow and 5HT in blue. This forms the basis upon which treatment effect heterogeneity is simulated, with hypothetical treatments selectively effective for lesions disrupting defined receptor territories. Each panel shows the same render from a different spatial perspective: **a**, left; **b**, right; **c**, anterior; **d**, posterior; **e**, superior; **f**, inferior. The underlay is a thresholded white matter template surface in MNI.

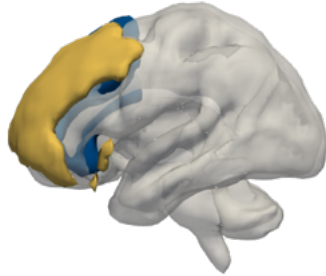
S9.3.2: *Introspection* subnetwork axial slices



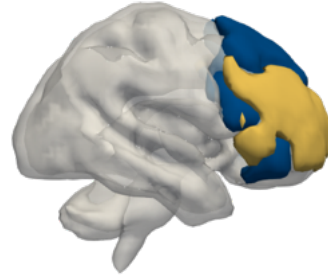
Axial slice visualisation of the functional grey matter network representing *introspection*, overlaid onto the standard MNI152 template. The labelled co-ordinates map to MNI space. The colours label functional subnetworks separated by neurotransmitter receptor distribution preponderance, here glutamate in yellow and 5HT in blue. This forms the basis upon which treatment effect heterogeneity is simulated, with hypothetical treatments selectively effective for lesions disrupting defined receptor territories.

S9.4.1: *Cognition* subnetwork render

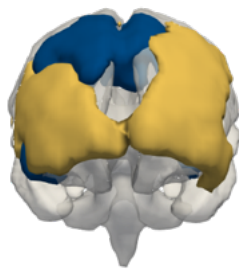
a



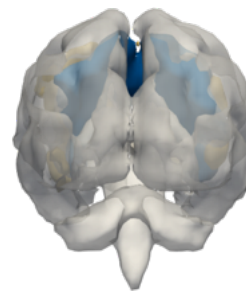
b



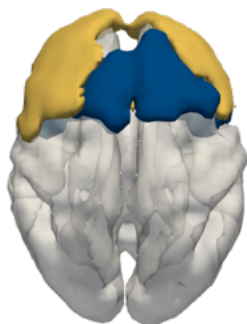
c



d



e

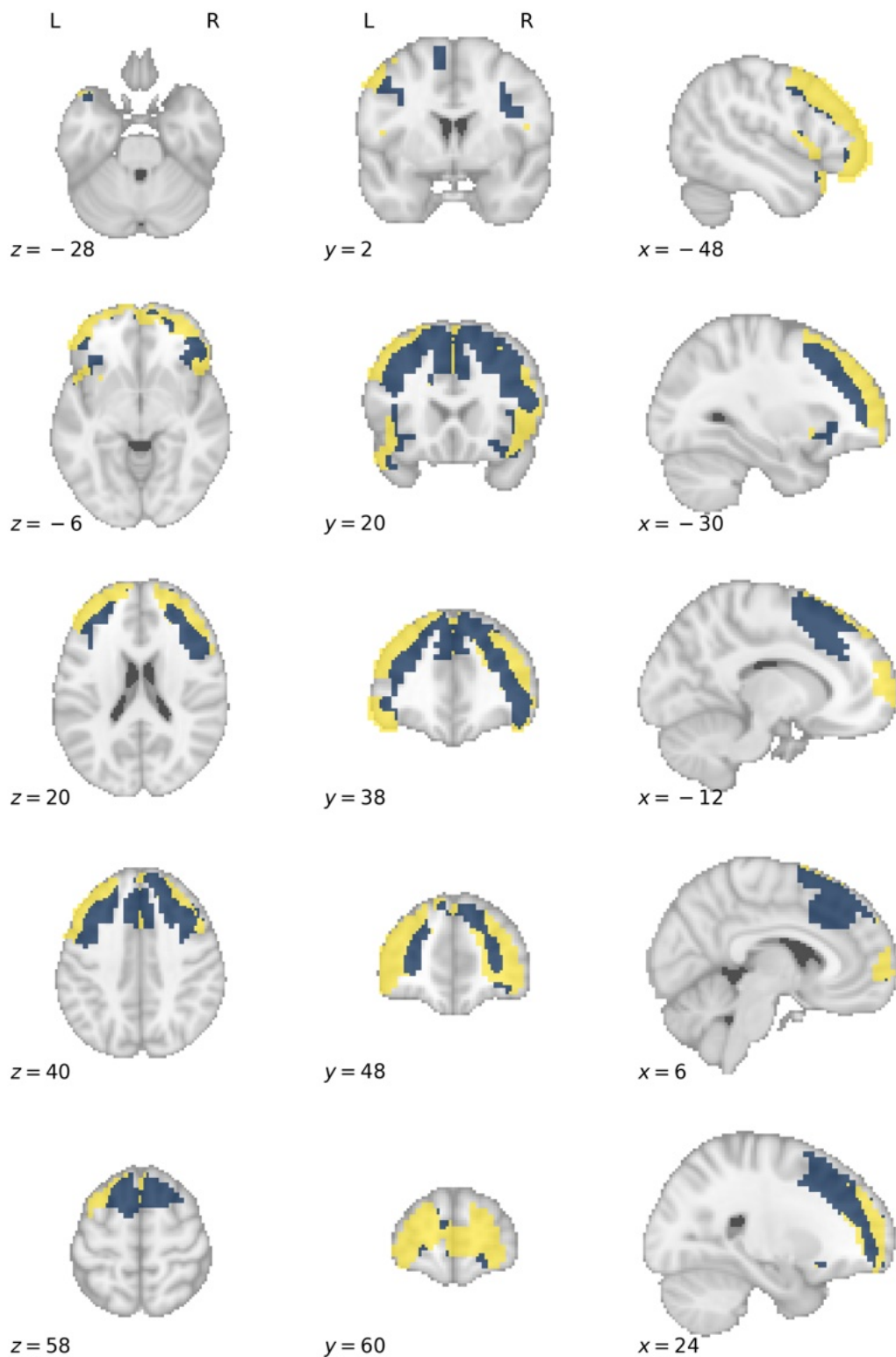


f



Three-dimensional rendering of the functional grey matter network representing *cognition*. The colours label functional subnetworks separated by neurotransmitter receptor distribution preponderance, here cannabinoid in yellow and opioid in blue. This forms the basis upon which treatment effect heterogeneity is simulated, with hypothetical treatments selectively effective for lesions disrupting defined receptor territories. Each panel shows the same render from a different spatial perspective: **a**, left; **b**, right; **c**, anterior; **d**, posterior, **e**, superior; **f**, inferior. The underlay is a thresholded white matter template surface in MNI.

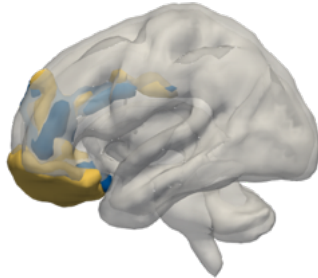
S9.4.2: *Cognition* subnetwork axial slices



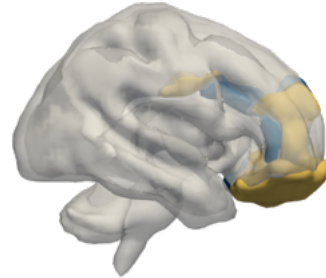
Axial slice visualisation of the functional grey matter network representing *cognition*, overlaid onto the standard MNI152 template. The labelled co-ordinates map to MNI space. The colours label functional subnetworks separated by neurotransmitter receptor distribution preponderance, here cannabinoid in yellow and opioid in blue. This forms the basis upon which treatment effect heterogeneity is simulated, with hypothetical treatments selectively effective for lesions disrupting defined receptor territories.

S9.5.1: *Mood* subnetwork render

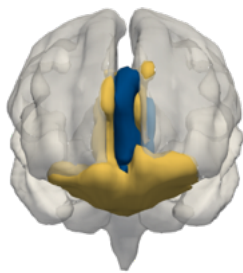
a



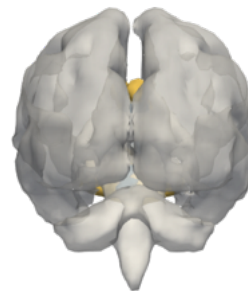
b



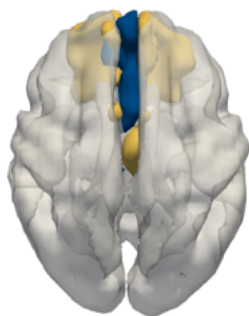
c



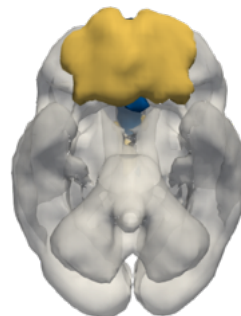
d



e

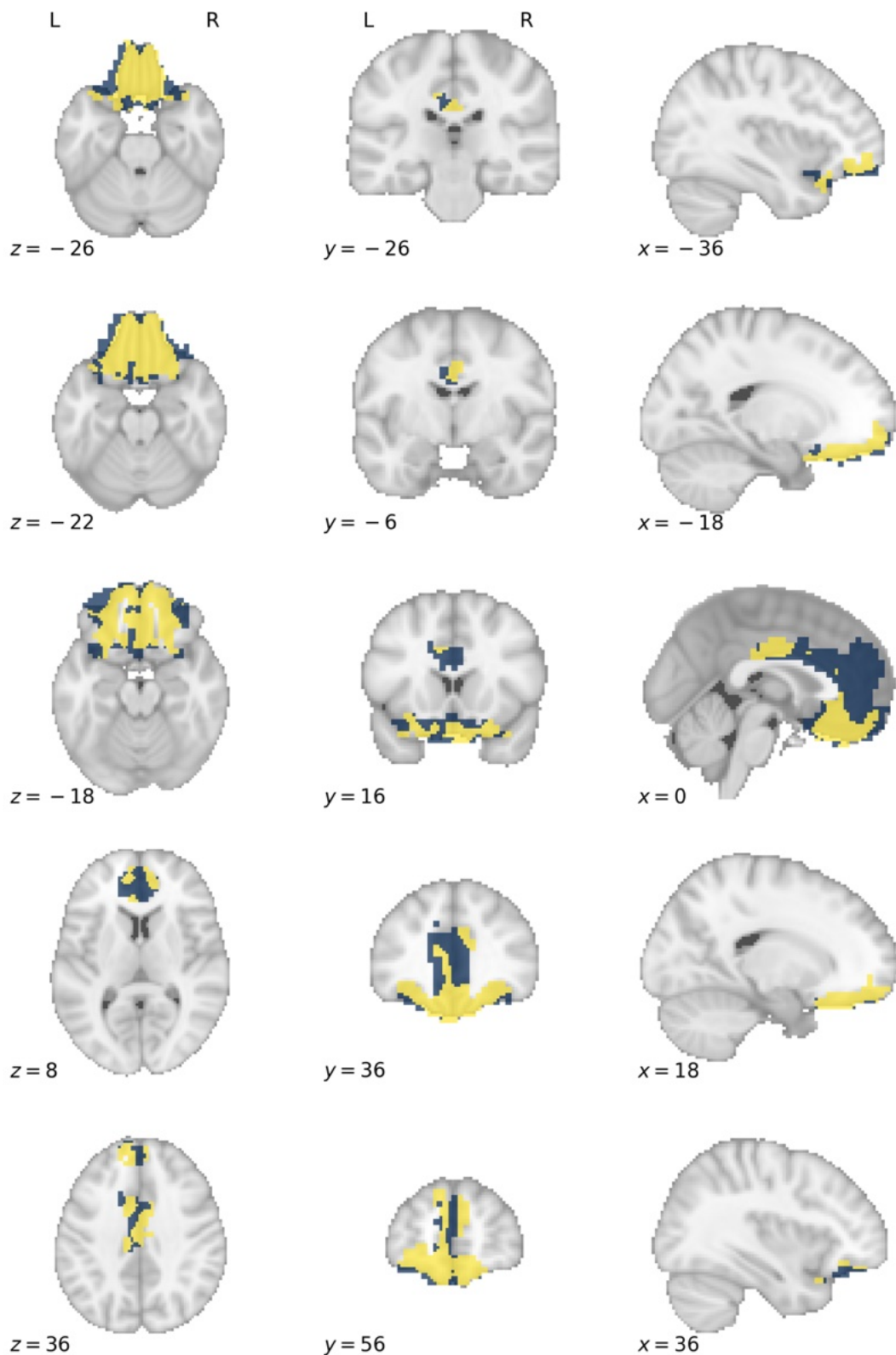


f



Three-dimensional rendering of the functional grey matter network representing *mood*. The colours label functional subnetworks separated by neurotransmitter receptor distribution preponderance, here opioid in yellow and histamine in blue. This forms the basis upon which treatment effect heterogeneity is simulated, with hypothetical treatments selectively effective for lesions disrupting defined receptor territories. Each panel shows the same render from a different spatial perspective: **a**, left; **b**, right; **c**, anterior; **d**, posterior; **e**, superior; **f**, inferior. The underlay is a thresholded white matter template surface in MNI.

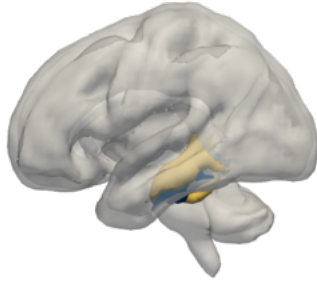
S9.5.2: *Mood* subnetwork axial slices



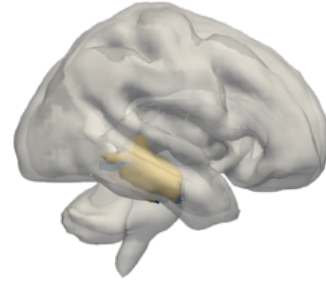
Axial slice visualisation of the functional grey matter network representing *mood*, overlaid onto the standard MNI152 template. The labelled co-ordinates map to MNI space. The colours label functional subnetworks separated by neurotransmitter receptor distribution preponderance, here opioid in yellow and histamine in blue. This forms the basis upon which treatment effect heterogeneity is simulated, with hypothetical treatments selectively effective for lesions disrupting defined receptor territories.

S9.6.1: *Memory* subnetwork render

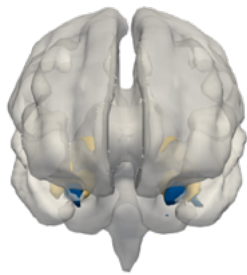
c



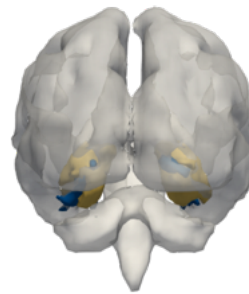
d



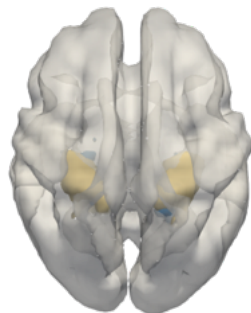
c



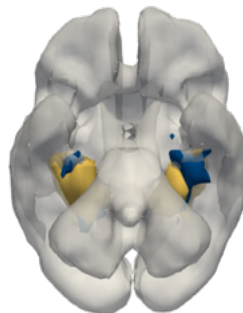
d



e

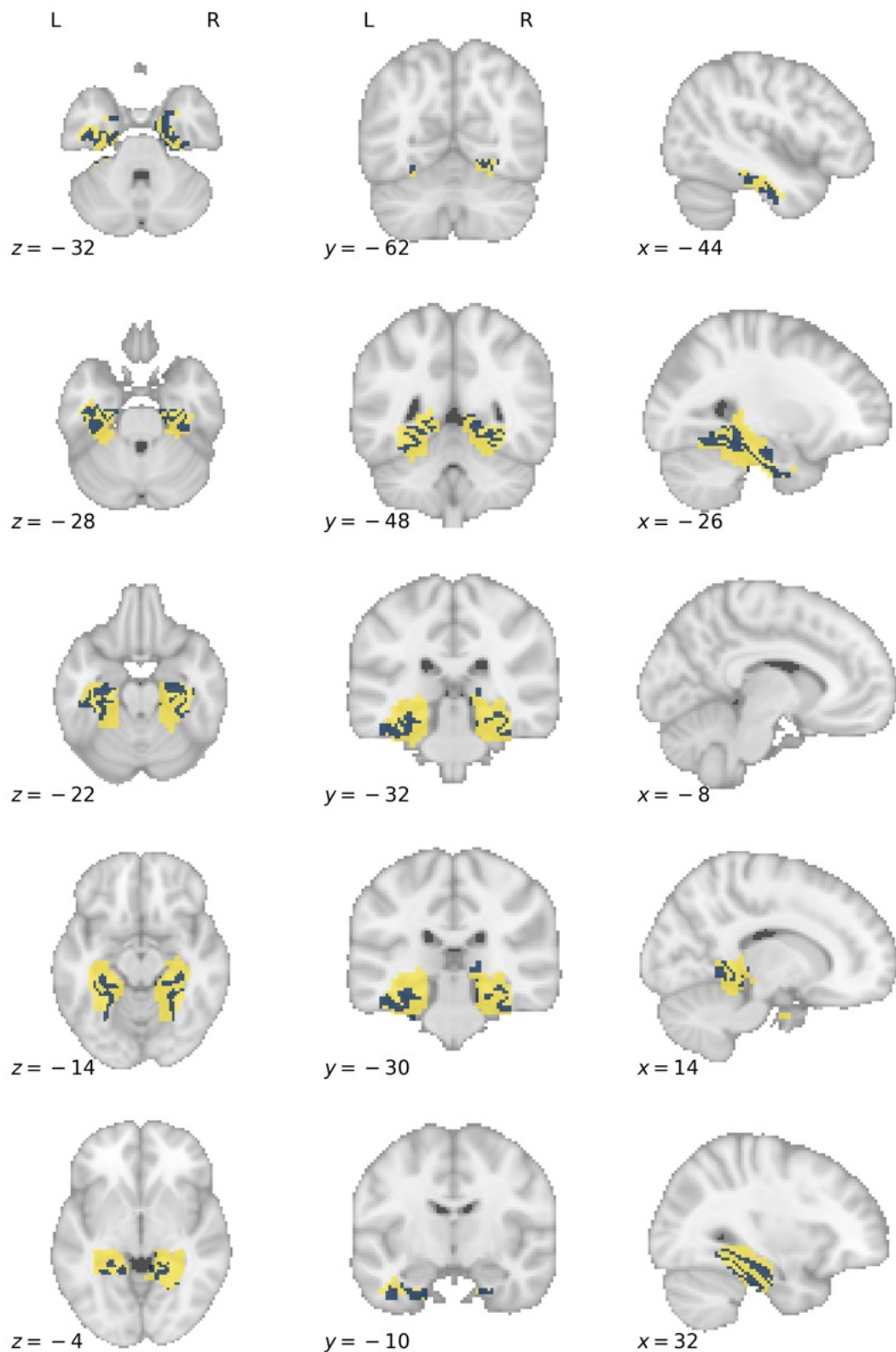


f



Three-dimensional rendering of the functional grey matter network representing *memory*. The colours label functional subnetworks separated by neurotransmitter receptor distribution preponderance, here dopamine in yellow and 5HT in blue. This forms the basis upon which treatment effect heterogeneity is simulated, with hypothetical treatments selectively effective for lesions disrupting defined receptor territories. Each panel shows the same render from a different spatial perspective: **a**, left; **b**, right; **c**, anterior; **d**, posterior; **e**, superior; **f**, inferior. The underlay is a thresholded white matter template surface in MNI.

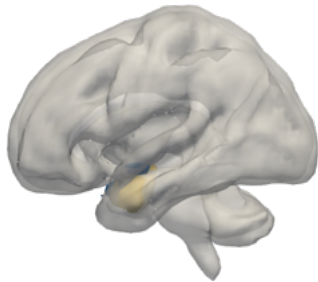
S9.6.2: *Memory* subnetwork axial slices



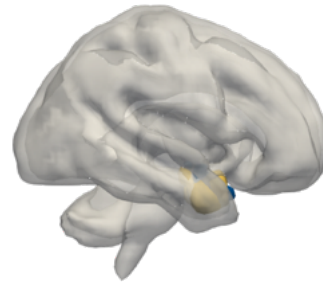
Axial slice visualisation of the functional grey matter network representing *memory*, overlaid onto the standard MNI152 template. The labelled co-ordinates map to MNI space. The colours label functional subnetworks separated by neurotransmitter receptor distribution preponderance, here dopamine in yellow and 5HT in blue. This forms the basis upon which treatment effect heterogeneity is simulated, with hypothetical treatments selectively effective for lesions disrupting defined receptor territories.

S9.7.1: *Aversion* subnetwork render

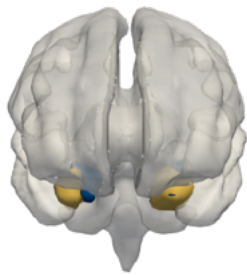
a



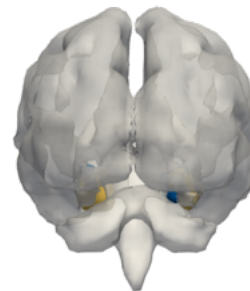
b



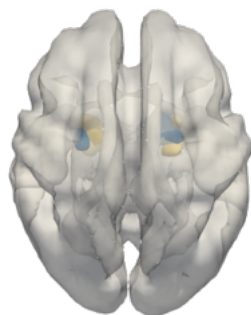
c



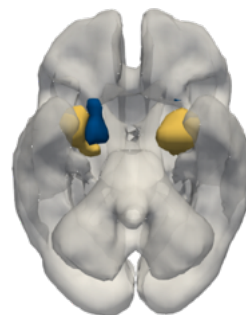
d



e

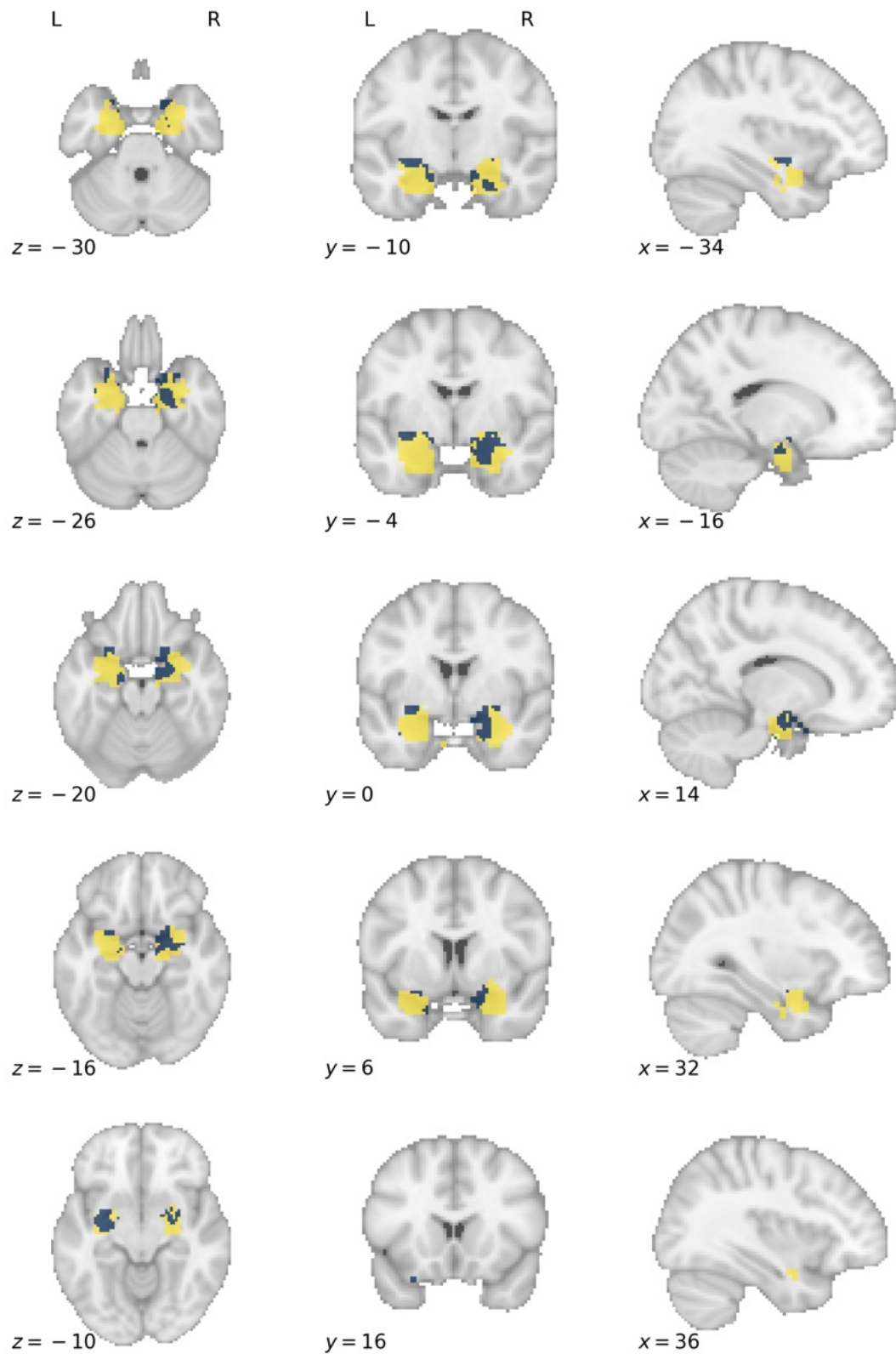


f



Three-dimensional rendering of the functional grey matter network representing *aversion*. The colours label functional subnetworks separated by neurotransmitter receptor distribution preponderance, here dopamine in yellow and histamine in blue. This forms the basis upon which treatment effect heterogeneity is simulated, with hypothetical treatments selectively effective for lesions disrupting defined receptor territories. Each panel shows the same render from a different spatial perspective: **a**, left; **b**, right; **c**, anterior; **d**, posterior, **e**, superior; **f**, inferior. The underlay is a thresholded white matter template surface in MNI.

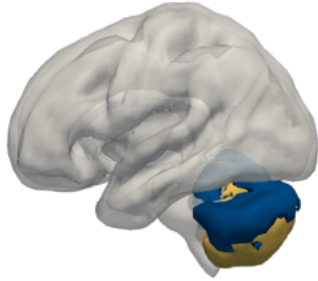
S9.7.2: *Aversion* subnetwork axial slices



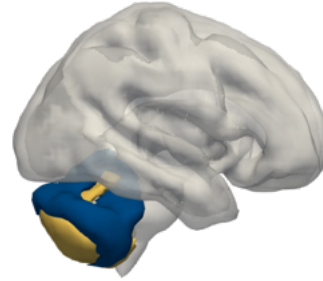
Axial slice visualisation of the functional grey matter network representing *aversion*, overlaid onto the standard MNI152 template. The labelled co-ordinates map to MNI space. The colours label functional subnetworks separated by neurotransmitter receptor distribution preponderance, here dopamine in yellow and histamine in blue. This forms the basis upon which treatment effect heterogeneity is simulated, with hypothetical treatments selectively effective for lesions disrupting defined receptor territories.

S9.8.1: *Coordination* subnetwork render

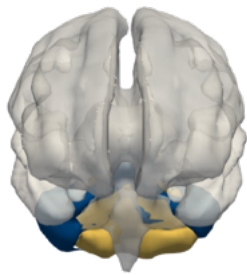
a



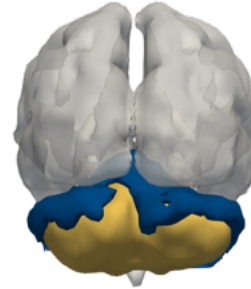
b



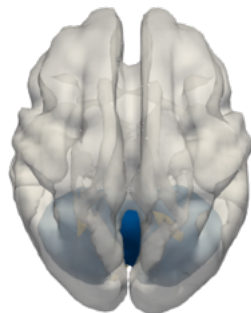
c



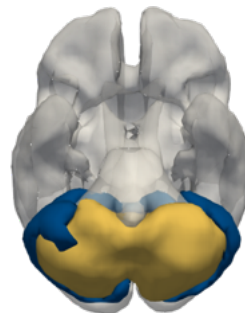
d



e

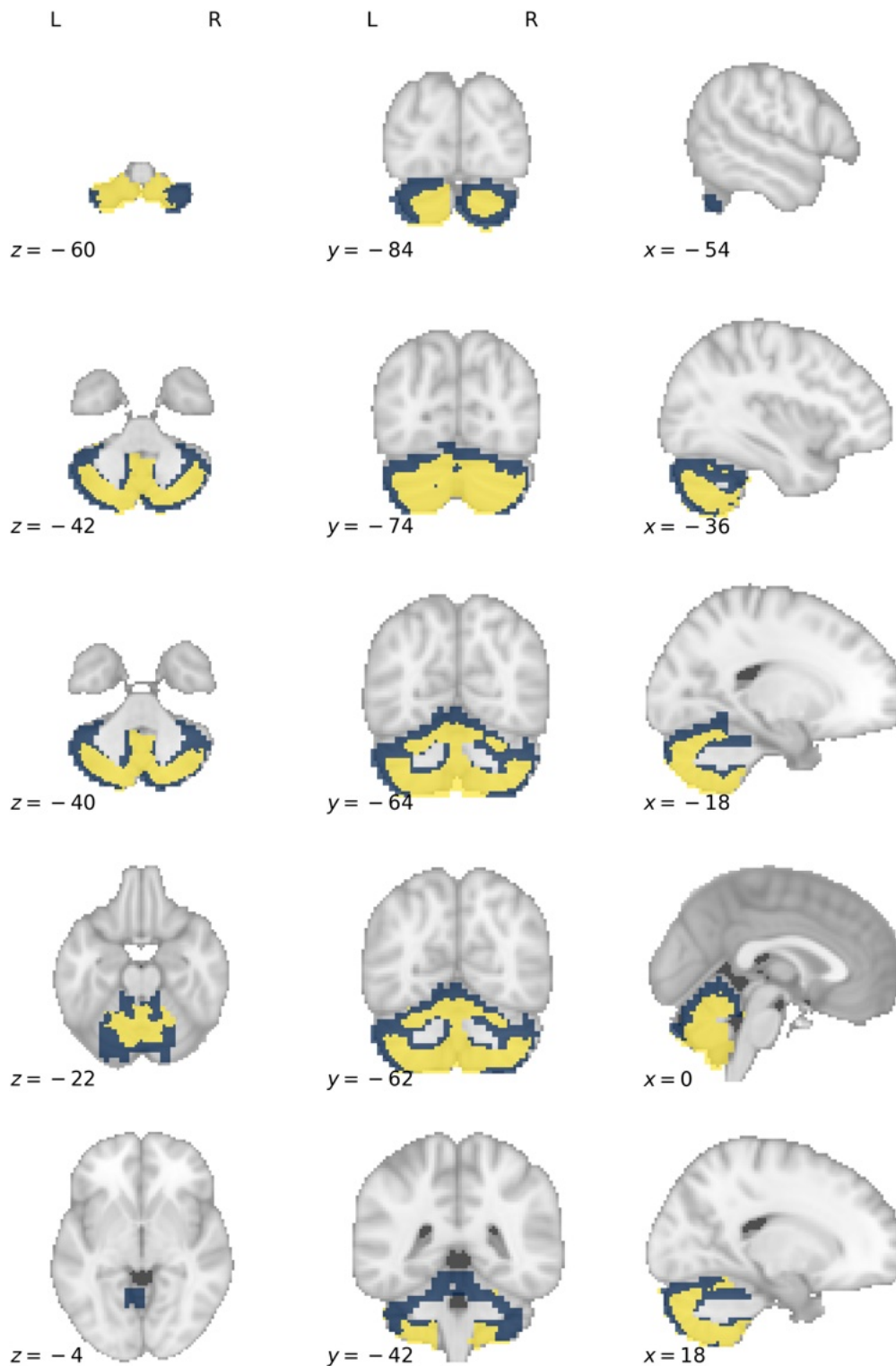


f



Three-dimensional rendering of the functional grey matter network representing *coordination*. The colours label functional subnetworks separated by neurotransmitter receptor distribution preponderance, here opioid in yellow and acetylcholine in blue. This forms the basis upon which treatment effect heterogeneity is simulated, with hypothetical treatments selectively effective for lesions disrupting defined receptor territories. Each panel shows the same render from a different spatial perspective: **a**, left; **b**, right; **c**, anterior; **d**, posterior, **e**, superior; **f**, inferior. The underlay is a thresholded white matter template surface in MNI.

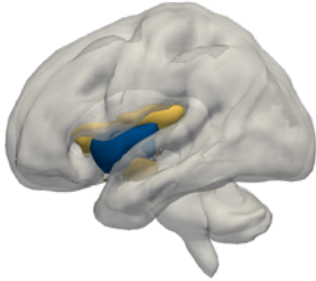
S9.8.2: *Coordination* subnetwork axial slices



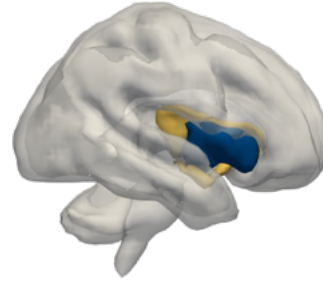
Axial slice visualisation of the functional grey matter network representing *coordination*, overlaid onto the standard MNI152 template. The labelled co-ordinates map to MNI space. The colours label functional subnetworks separated by neurotransmitter receptor distribution preponderance, here opioid in yellow and acetylcholine in blue. This forms the basis upon which treatment effect heterogeneity is simulated, with hypothetical treatments selectively effective for lesions disrupting defined receptor territories.

S9.9.1: *Interoception* subnetwork render

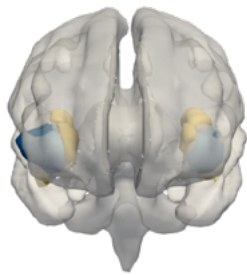
a



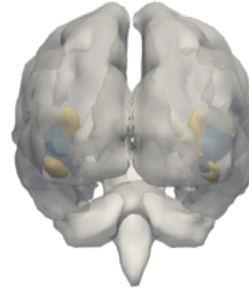
b



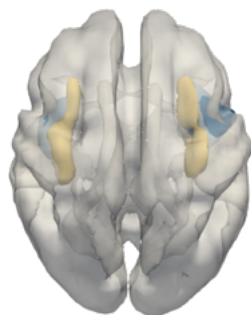
c



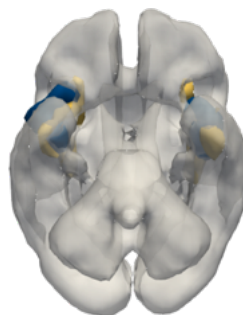
d



e

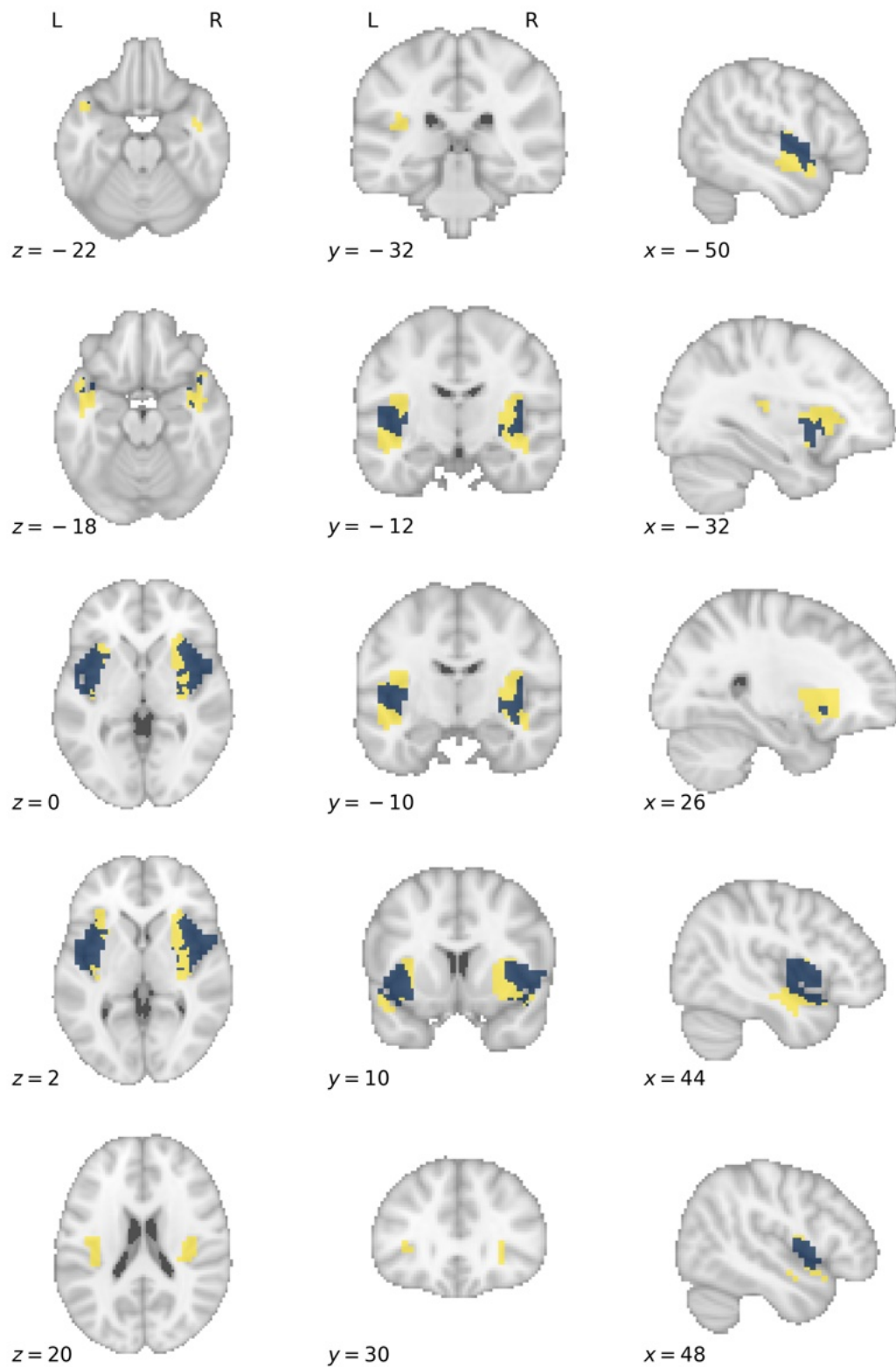


f



Three-dimensional rendering of the functional grey matter network representing *interoception*. The colours label functional subnetworks separated by neurotransmitter receptor distribution preponderance, here dopamine in yellow and histamine in blue. This forms the basis upon which treatment effect heterogeneity is simulated, with hypothetical treatments selectively effective for lesions disrupting defined receptor territories. Each panel shows the same render from a different spatial perspective: **a**, left; **b**, right; **c**, anterior; **d**, posterior, **e**, superior; **f**, inferior. The underlay is a thresholded white matter template surface in MNI.

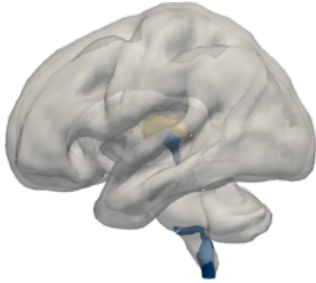
S9.9.2: *Interoception* subnetwork axial slices



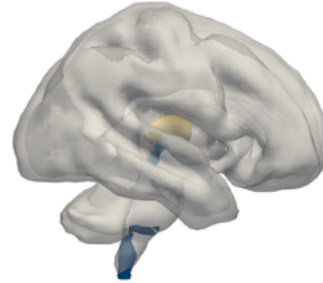
Axial slice visualisation of the functional grey matter network representing *interoception*, overlaid onto the standard MNI152 template. The labelled co-ordinates map to MNI space. The colours label functional subnetworks separated by neurotransmitter receptor distribution preponderance, here dopamine in yellow and histamine in blue. This forms the basis upon which treatment effect heterogeneity is simulated, with hypothetical treatments selectively effective for lesions disrupting defined receptor territories.

S9.10.1: *Sleep* subnetwork render

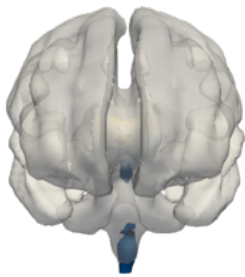
a



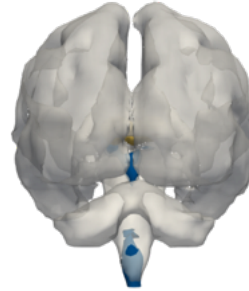
b



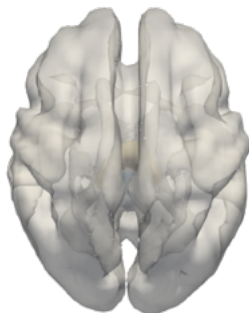
c



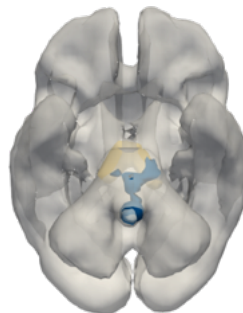
d



e

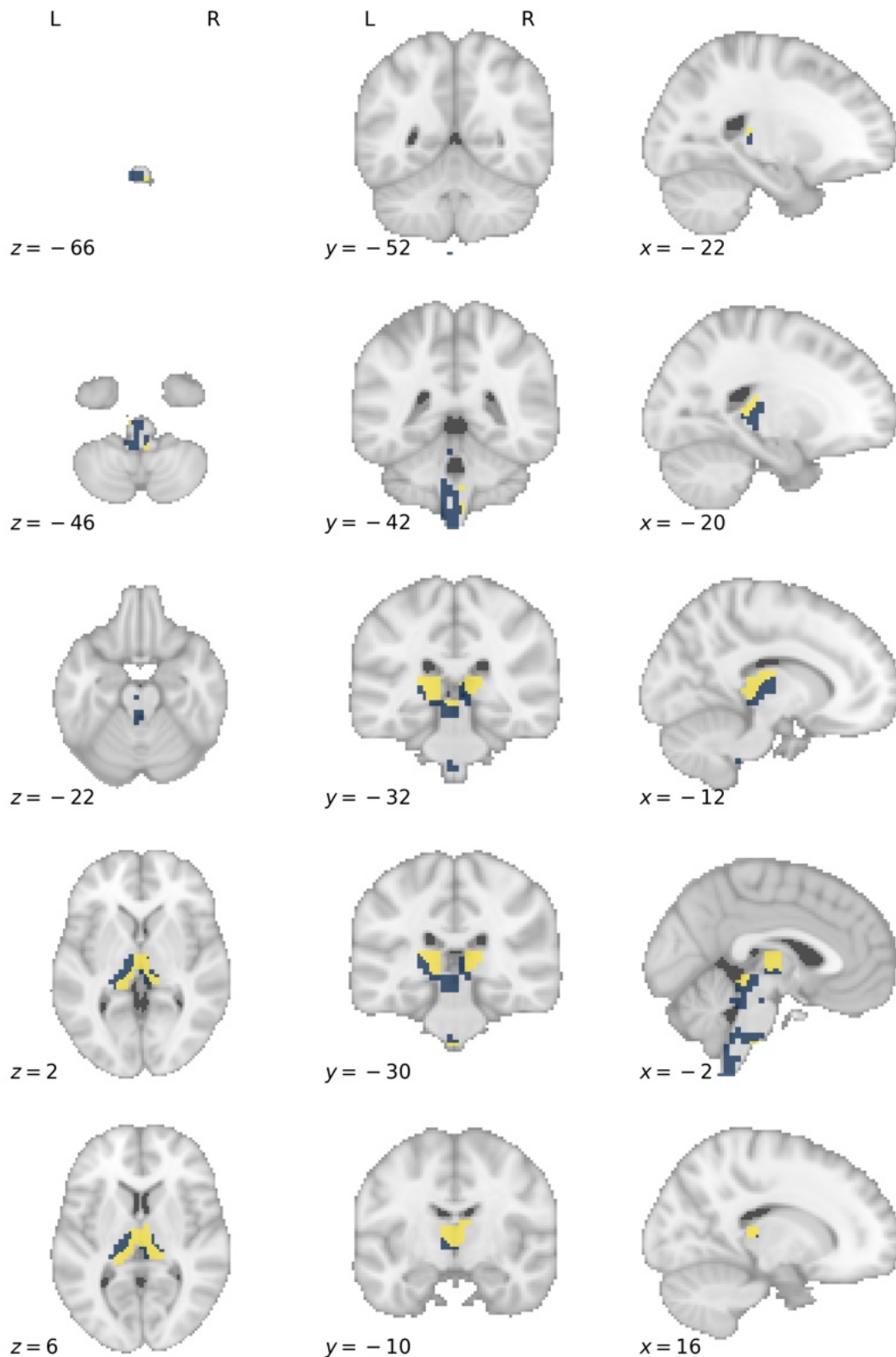


f



Three-dimensional rendering of the functional grey matter network representing *sleep*. The colours label functional subnetworks separated by neurotransmitter receptor distribution preponderance, here opioid in yellow and noradrenaline in blue. This forms the basis upon which treatment effect heterogeneity is simulated, with hypothetical treatments selectively effective for lesions disrupting defined receptor territories. Each panel shows the same render from a different spatial perspective: **a**, left; **b**, right; **c**, anterior; **d**, posterior, **e**, superior; **f**, inferior. The underlay is a thresholded white matter template surface in MNI.

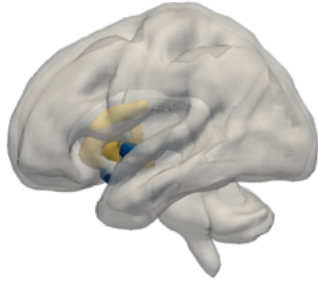
S9.10.2: *Sleep* subnetwork axial slices



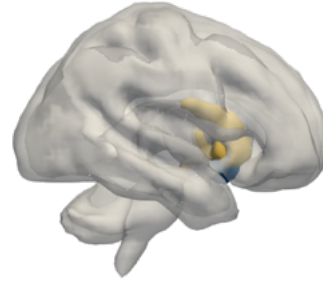
Axial slice visualisation of the functional grey matter network representing *sleep*, overlaid onto the standard MNI152 template. The labelled co-ordinates map to MNI space. The colours label functional subnetworks separated by neurotransmitter receptor distribution preponderance, here opioid in yellow and noradrenaline in blue. This forms the basis upon which treatment effect heterogeneity is simulated, with hypothetical treatments selectively effective for lesions disrupting defined receptor territories.

S9.11.1: *Reward* subnetwork render

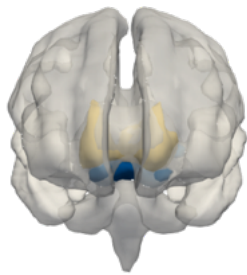
a



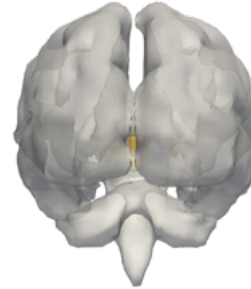
b



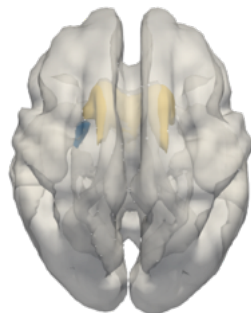
c



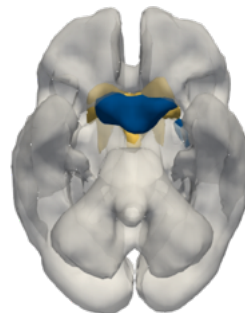
d



e

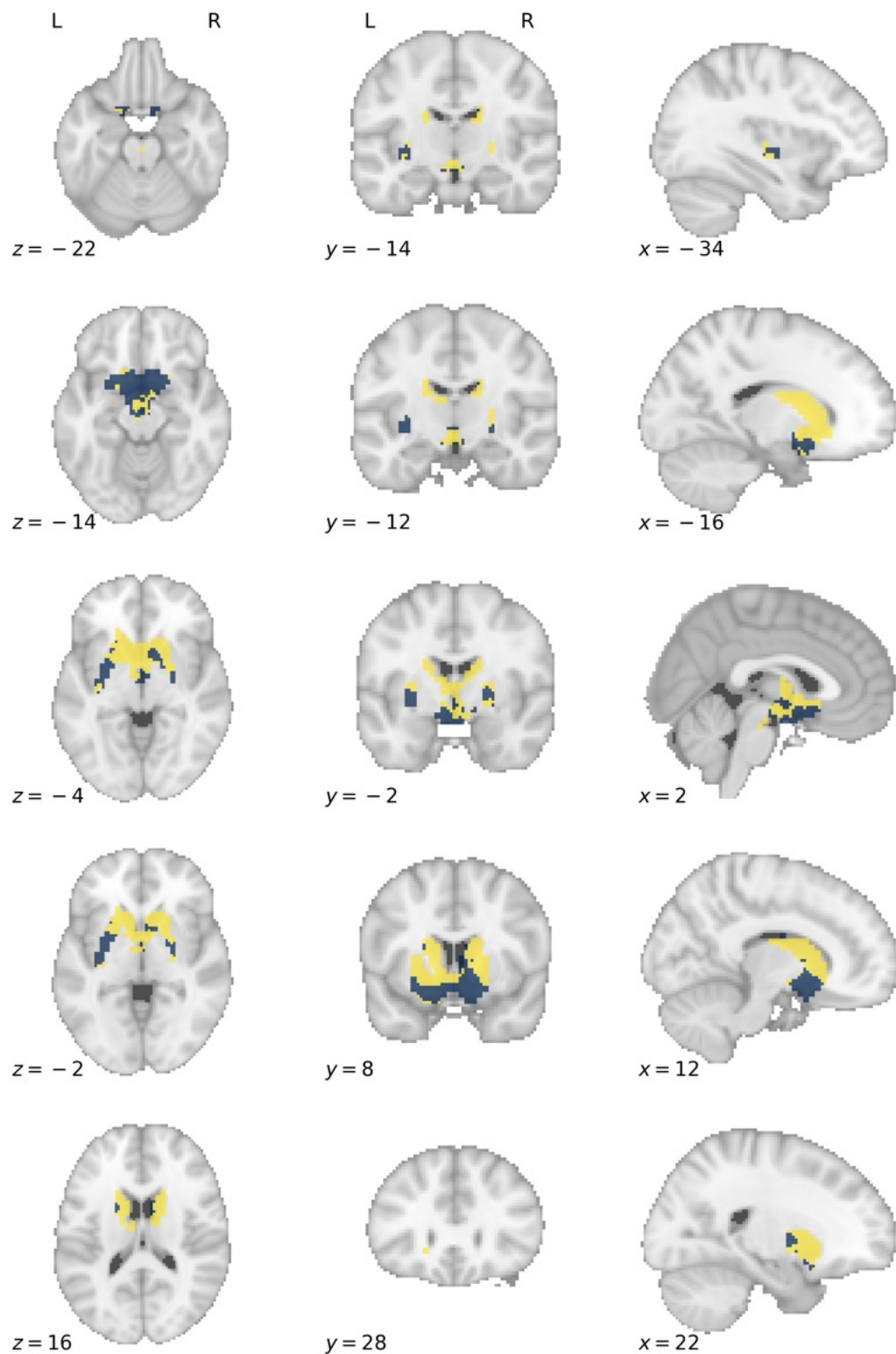


f



Three-dimensional rendering of the functional grey matter network representing *reward*. The colours label functional subnetworks separated by neurotransmitter receptor distribution preponderance, here dopamine in yellow and histamine in blue. This forms the basis upon which treatment effect heterogeneity is simulated, with hypothetical treatments selectively effective for lesions disrupting defined receptor territories. Each panel shows the same render from a different spatial perspective: **a**, left; **b**, right; **c**, anterior; **d**, posterior, **e**, superior; **f**, inferior. The underlay is a thresholded white matter template surface in MNI.

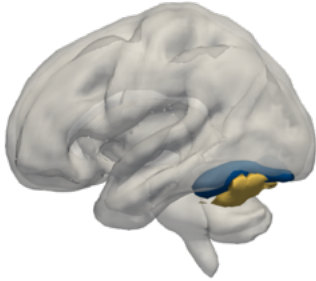
S9.11.2: *Reward* subnetwork axial slices



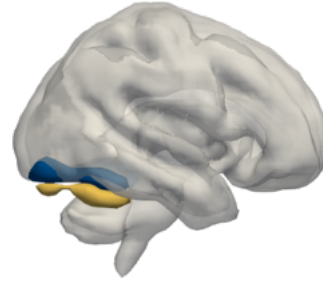
Axial slice visualisation of the functional grey matter network representing *reward*, overlaid onto the standard MNI152 template. The labelled co-ordinates map to MNI space. The colours label functional subnetworks separated by neurotransmitter receptor distribution preponderance, here dopamine in yellow and histamine in blue. This forms the basis upon which treatment effect heterogeneity is simulated, with hypothetical treatments selectively effective for lesions disrupting defined receptor territories.

S9.12.1: *Visual Recognition* subnetwork render

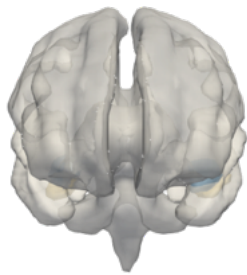
a



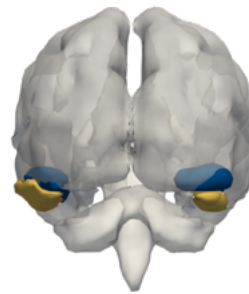
b



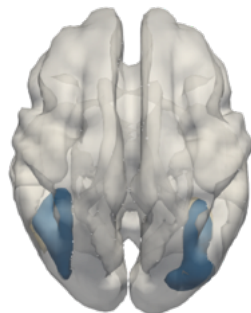
c



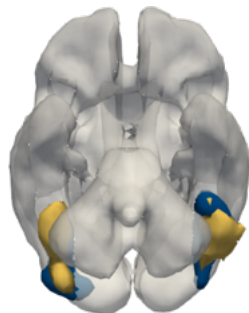
d



e

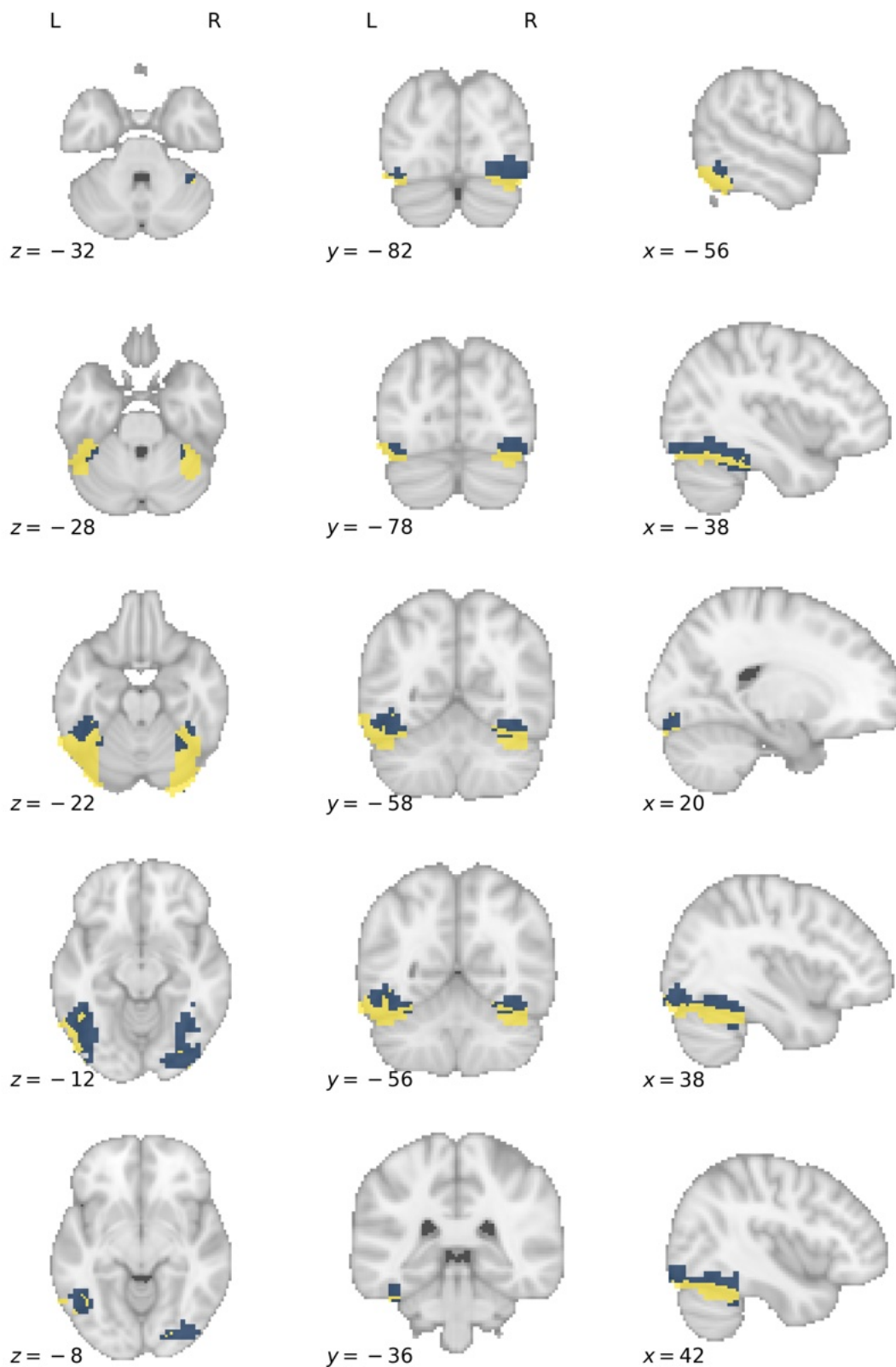


f



Three-dimensional rendering of the functional grey matter network representing *visual recognition*. The colours label functional subnetworks separated by neurotransmitter receptor distribution preponderance, here cannabinoid in yellow and GABA in blue. This forms the basis upon which treatment effect heterogeneity is simulated, with hypothetical treatments selectively effective for lesions disrupting defined receptor territories. Each panel shows the same render from a different spatial perspective: **a**, left; **b**, right; **c**, anterior; **d**, posterior, **e**, superior; **f**, inferior. The underlay is a thresholded white matter template surface in MNI.

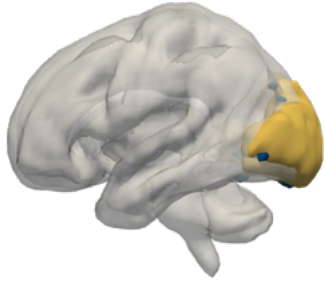
S9.12.2: *Visual Recognition* subnetwork axial slices



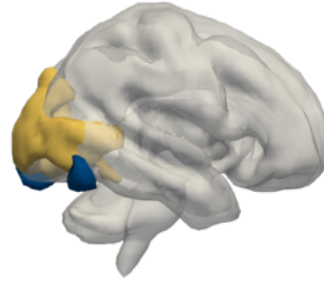
Axial slice visualisation of the functional grey matter network representing *visual recognition*, overlaid onto the standard MNI152 template. The labelled co-ordinates map to MNI space. The colours label functional subnetworks separated by neurotransmitter receptor distribution preponderance, here cannabinoid in yellow and GABA in blue. This forms the basis upon which treatment effect heterogeneity is simulated, with hypothetical treatments selectively effective for lesions disrupting defined receptor territories.

S9.13.1: *Visual Perception* subnetwork render

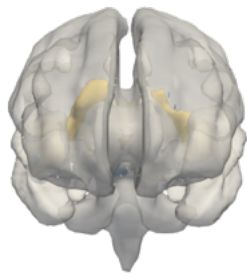
a



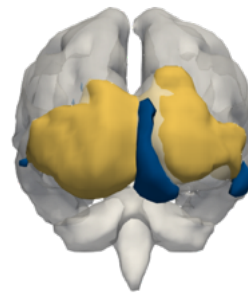
b



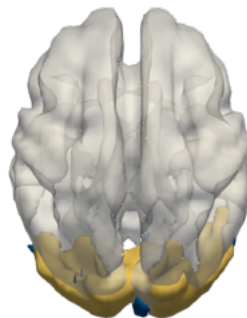
c



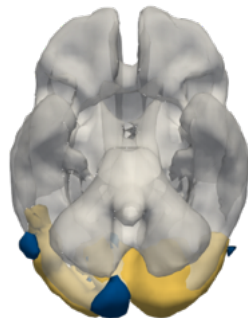
d



e

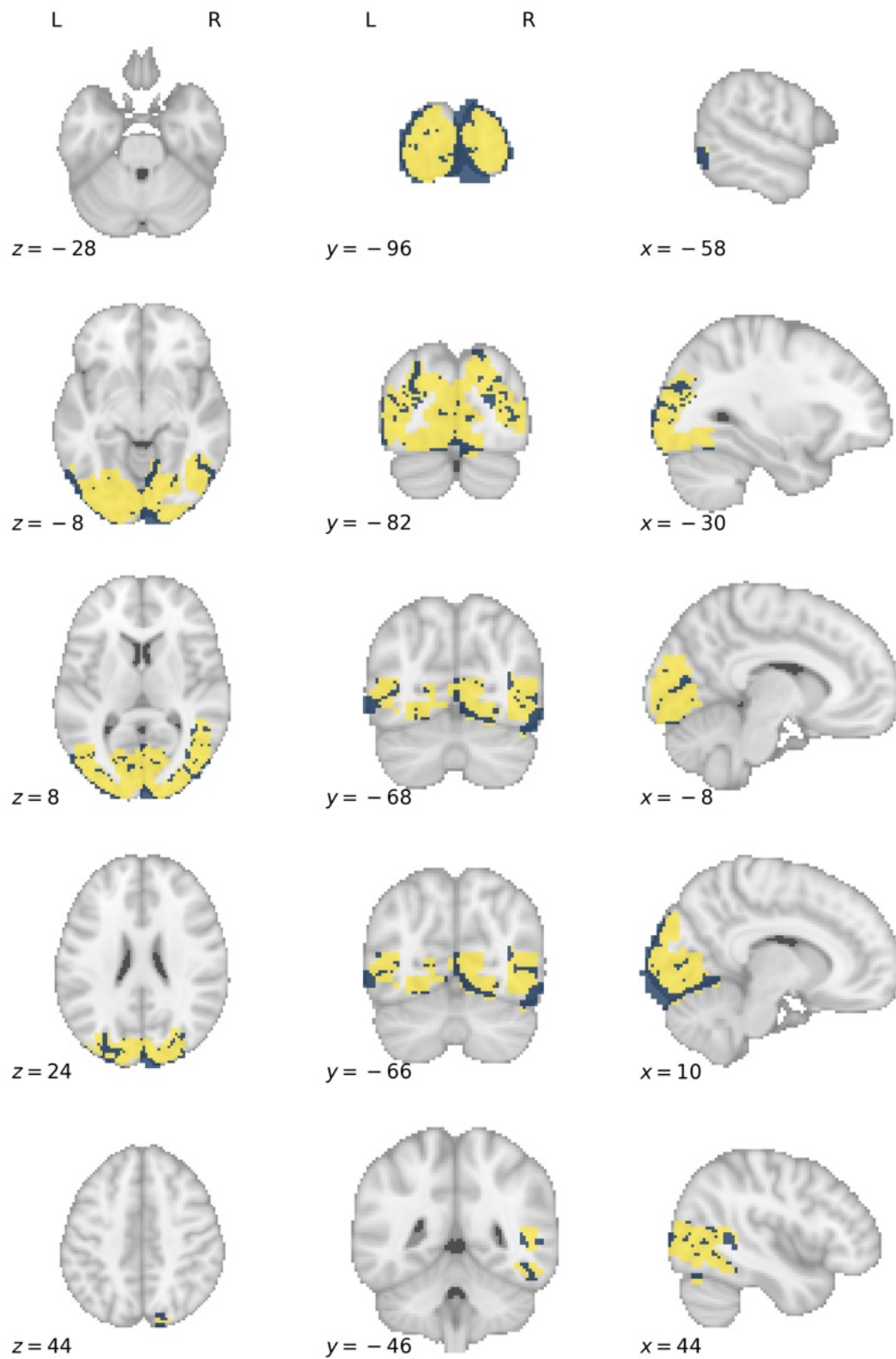


f



Three-dimensional rendering of the functional grey matter network representing *visual perception*. The colours label functional subnetworks separated by neurotransmitter receptor distribution preponderance, here GABA in yellow and 5HT in blue. This forms the basis upon which treatment effect heterogeneity is simulated, with hypothetical treatments selectively effective for lesions disrupting defined receptor territories. Each panel shows the same render from a different spatial perspective: **a**, left; **b**, right; **c**, anterior; **d**, posterior, **e**, superior; **f**, inferior. The underlay is a thresholded white matter template surface in MNI.

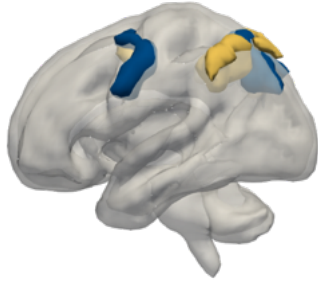
S9.13.2: *Visual Perception* subnetwork axial slices



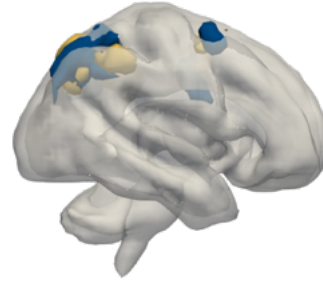
Axial slice visualisation of the functional grey matter network representing *visual perception*, overlaid onto the standard MNI152 template. The labelled co-ordinates map to MNI space. The colours label functional subnetworks separated by neurotransmitter receptor distribution preponderance, here GABA in yellow and 5HT in blue. This forms the basis upon which treatment effect heterogeneity is simulated, with hypothetical treatments selectively effective for lesions disrupting defined receptor territories.

S9.14.1: *Spatial Reasoning* subnetwork render

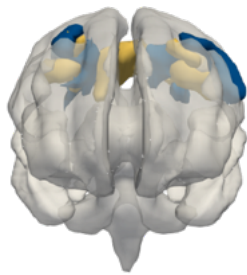
a



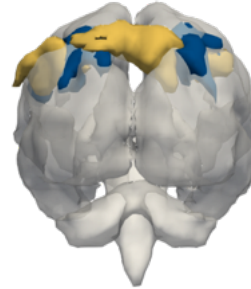
b



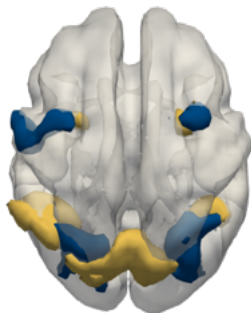
c



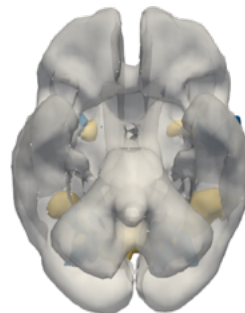
d



e

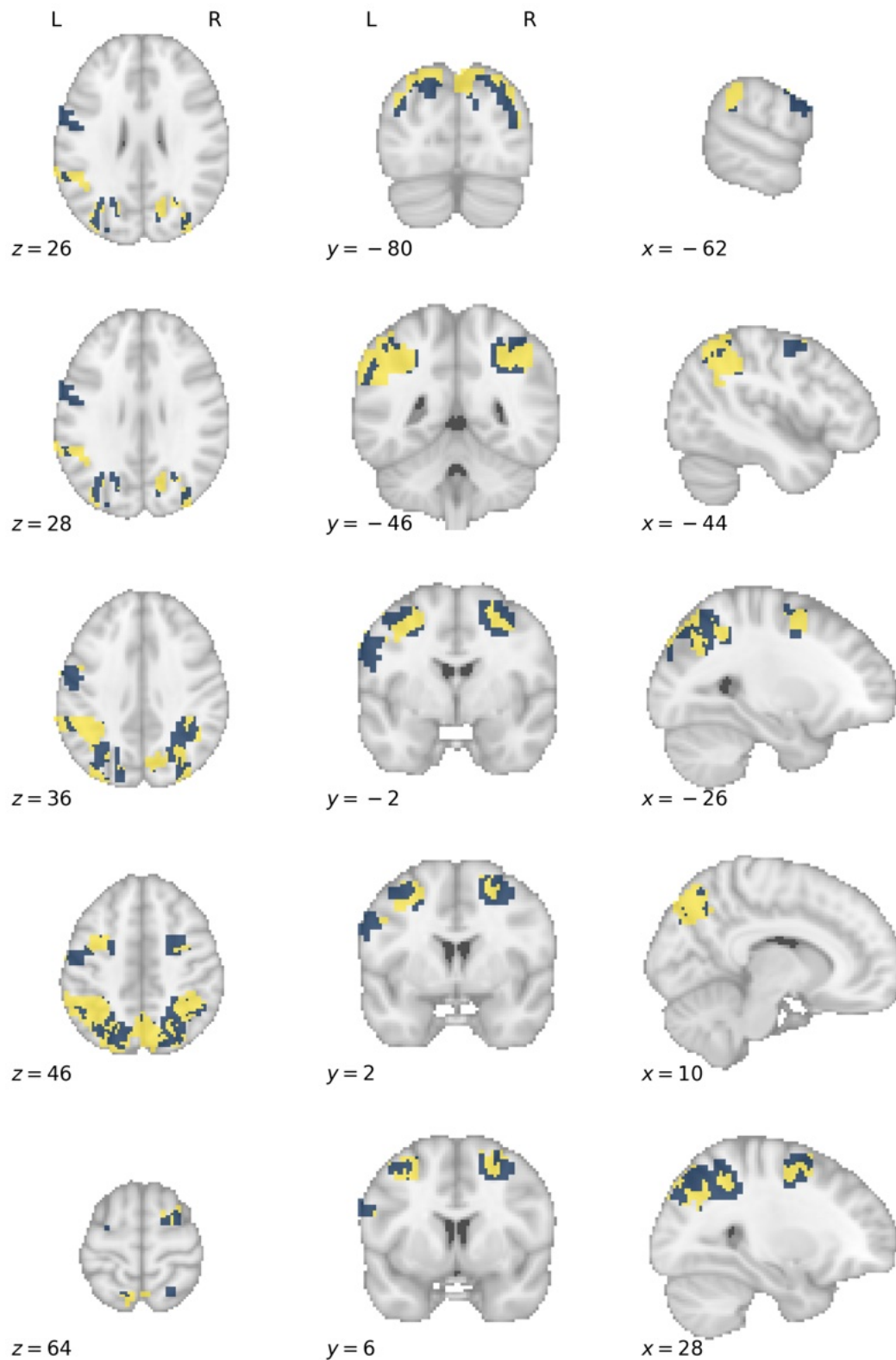


f



Three-dimensional rendering of the functional grey matter network representing *spatial reasoning*. The colours label functional subnetworks separated by neurotransmitter receptor distribution preponderance, here glutamate in yellow and noradrenaline in blue. This forms the basis upon which treatment effect heterogeneity is simulated, with hypothetical treatments selectively effective for lesions disrupting defined receptor territories. Each panel shows the same render from a different spatial perspective: **a**, left; **b**, right; **c**, anterior; **d**, posterior; **e**, superior; **f**, inferior. The underlay is a thresholded white matter template surface in MNI.

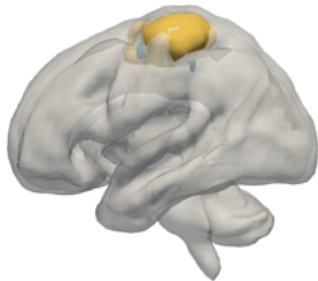
S9.14.2: *Spatial Reasoning* subnetwork axial slices



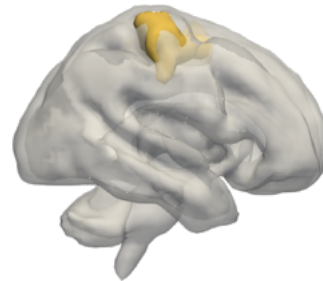
Axial slice visualisation of the functional grey matter network representing *spatial reasoning*, overlaid onto the standard MNI152 template. The labelled co-ordinates map to MNI space. The colours label functional subnetworks separated by neurotransmitter receptor distribution preponderance, here glutamate in yellow and noradrenaline in blue. This forms the basis upon which treatment effect heterogeneity is simulated, with hypothetical treatments selectively effective for lesions disrupting defined receptor territories.

S9.15.1: *Motor* subnetwork render

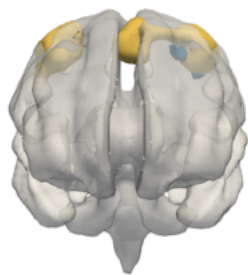
a



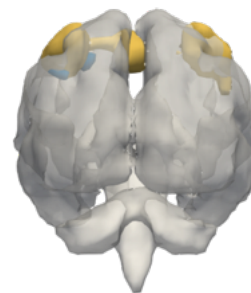
b



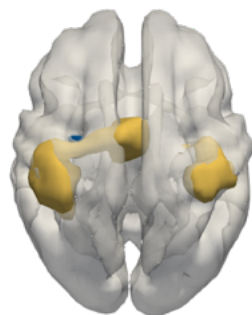
c



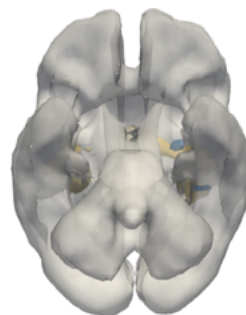
d



e

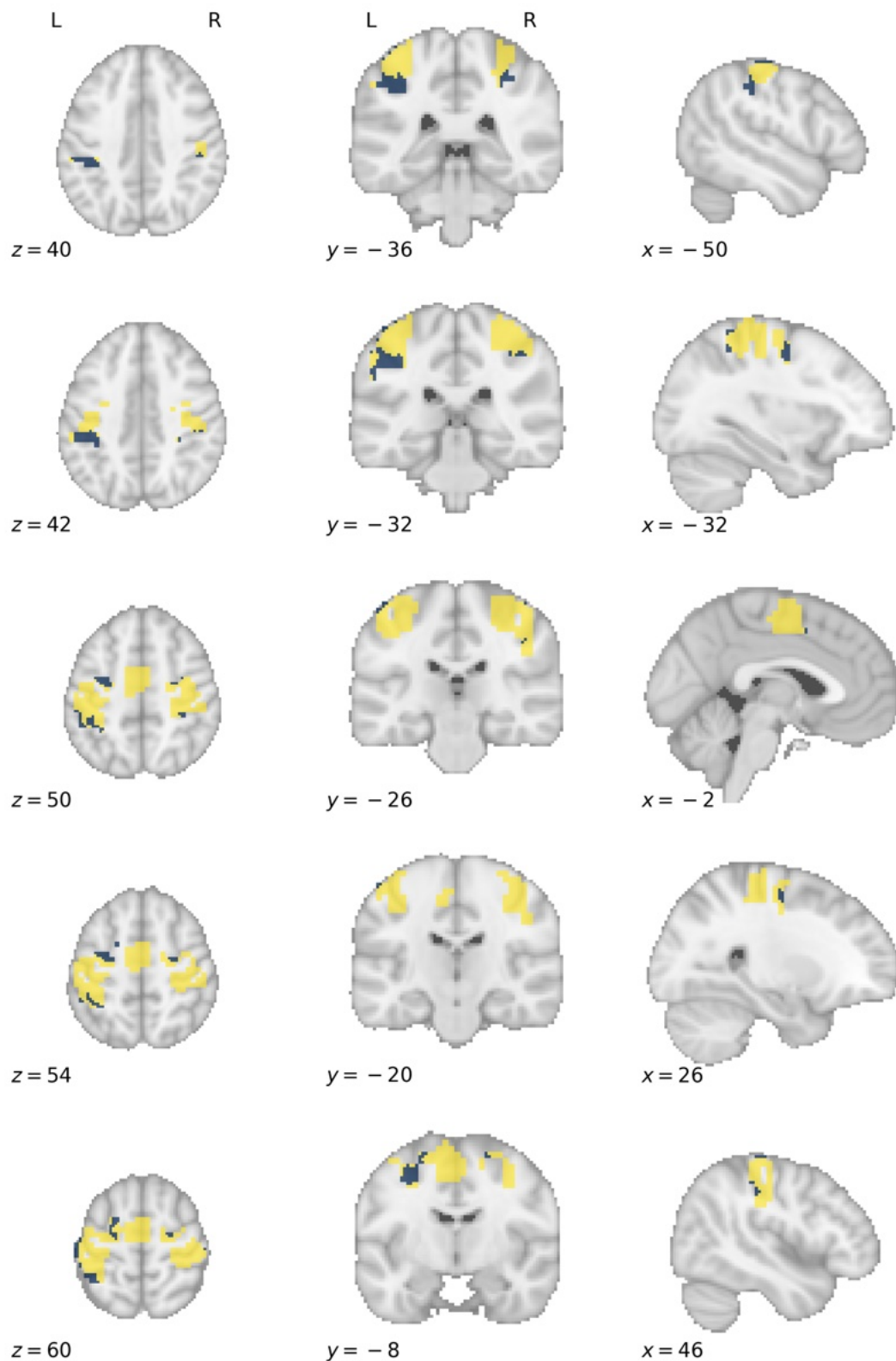


f



Three-dimensional rendering of the functional grey matter network representing *motor behaviour*. The colours label functional subnetworks separated by neurotransmitter receptor distribution preponderance, here noradrenaline in yellow and glutamate in blue. This forms the basis upon which treatment effect heterogeneity is simulated, with hypothetical treatments selectively effective for lesions disrupting defined receptor territories. Each panel shows the same render from a different spatial perspective: **a**, left; **b**, right; **c**, anterior; **d**, posterior; **e**, superior; **f**, inferior. The underlay is a thresholded white matter template surface in MNI.

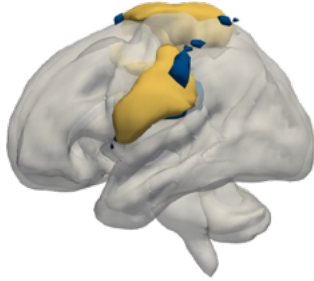
S9.15.2: *Motor* subnetwork axial slices



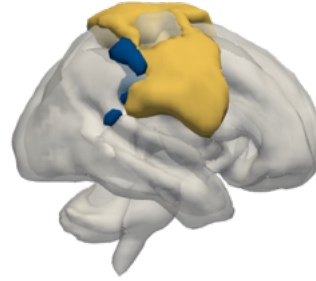
Axial slice visualisation of the functional grey matter network representing *motor behaviour*, overlaid onto the standard MNI152 template. The labelled co-ordinates map to MNI space. The colours label functional subnetworks separated by neurotransmitter receptor distribution preponderance, here noradrenaline in yellow and glutamate in blue. This forms the basis upon which treatment effect heterogeneity is simulated, with hypothetical treatments selectively effective for lesions disrupting defined receptor territories.

S9.16.1: *Somatosensory* subnetwork render

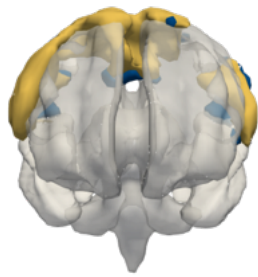
a



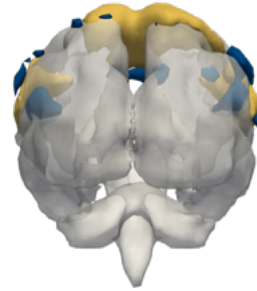
b



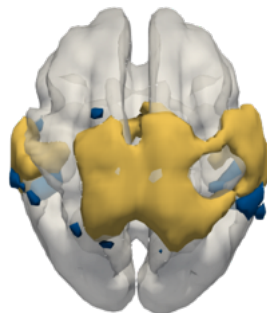
c



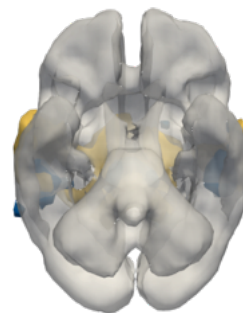
d



e

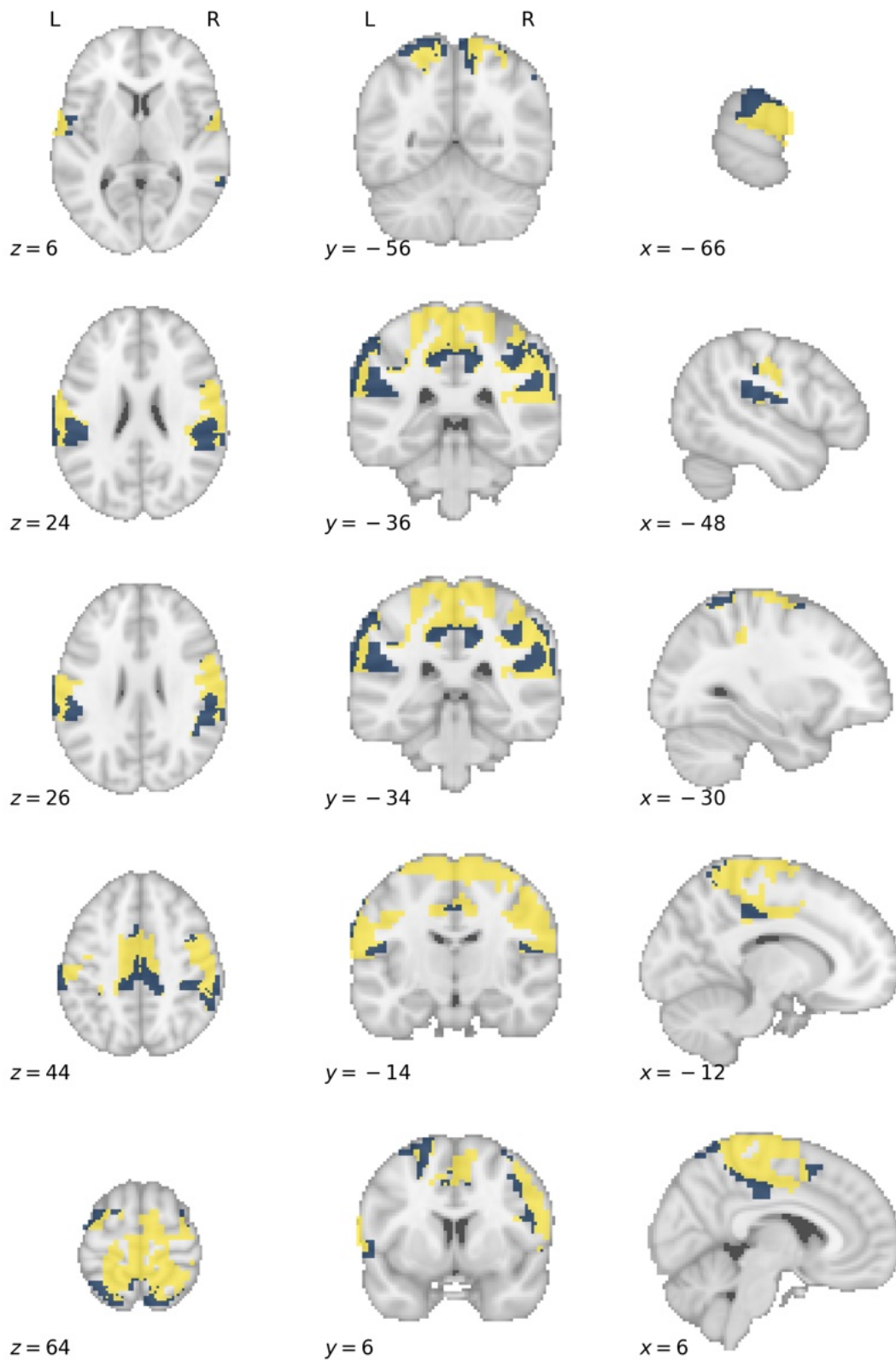


f



Three-dimensional rendering of the functional grey matter network representing *somatosensory function*. The colours label functional subnetworks separated by neurotransmitter receptor distribution preponderance, here noradrenaline in yellow and glutamate in blue. This forms the basis upon which treatment effect heterogeneity is simulated, with hypothetical treatments selectively effective for lesions disrupting defined receptor territories. Each panel shows the same render from a different spatial perspective: **a**, left; **b**, right; **c**, anterior; **d**, posterior; **e**, superior; **f**, inferior. The underlay is a thresholded white matter template surface in MNI.

S9.16.2: Somatosensory subnetwork axial slices



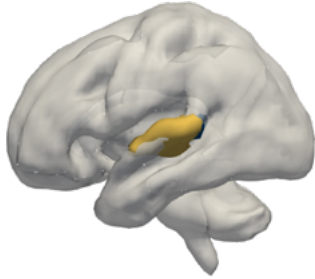
Axial slice visualisation of the functional grey matter network representing *somatosensory function*, overlaid onto the standard MNI152 template. The labelled co-ordinates map to MNI space. The colours label functional subnetworks separated by neurotransmitter receptor distribution preponderance, here noradrenaline in yellow and glutamate in blue. This forms the basis upon which treatment effect heterogeneity is simulated, with hypothetical treatments selectively effective for lesions disrupting defined receptor territories.

S10: Transcriptome subnetworks

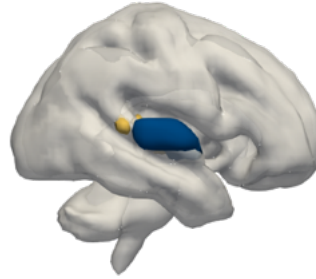
The following figures show, for each functional network, divisions into two subnetworks based on agglomerative clustering of microarray gene expression data (Hawrylycz et al., 2012). The assignment of unlabelled voxels was guided by the three-dimensional Gaussian distributions of the labelled voxels as described in the Methods section of the paper.

S10.1.1: *Hearing* subnetwork render

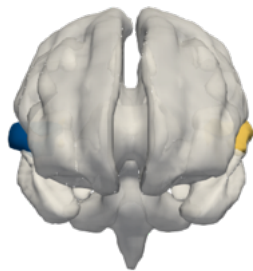
a



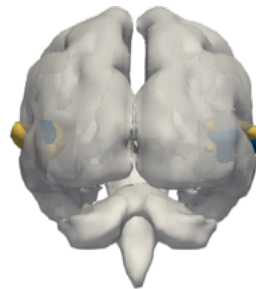
b



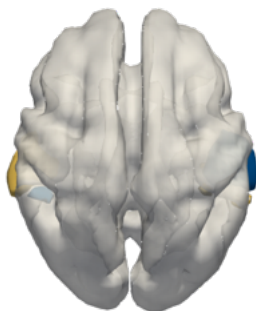
c



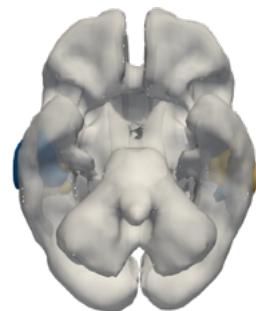
d



e

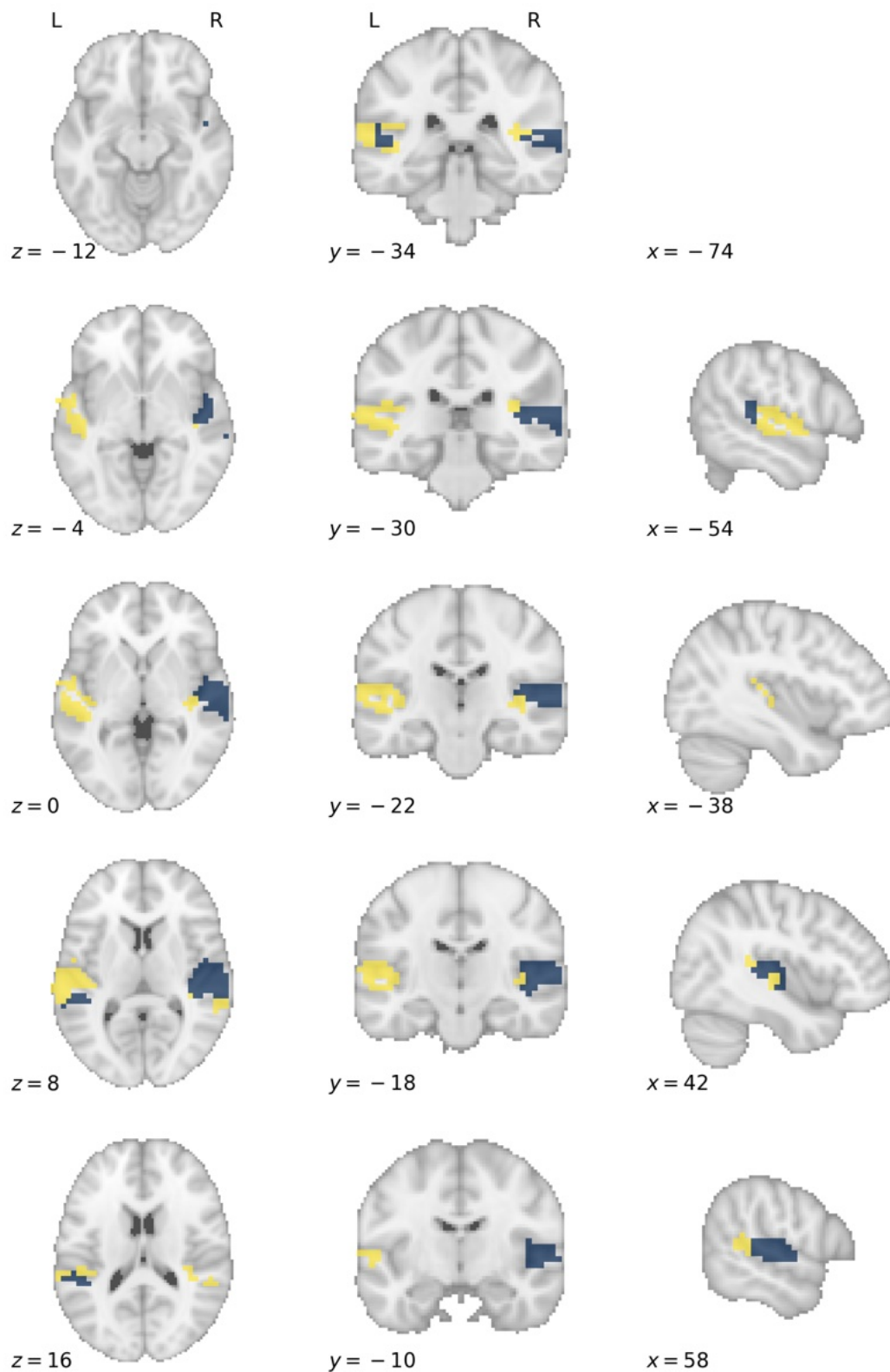


f



Three-dimensional rendering of the functional grey matter network representing *hearing*. The colours label functional subnetworks separated by microarray gene expression data, here represented in yellow and blue. This forms the basis upon which treatment effect heterogeneity is simulated, with hypothetical treatments selectively effective for lesions disrupting defined subnetworks. Each panel shows the same render from a different spatial perspective: **a**, left; **b**, right; **c**, anterior; **d**, posterior, **e**, superior; **f**, inferior.

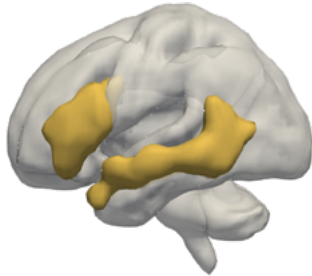
S10.1.2: *Hearing* subnetwork axial slices



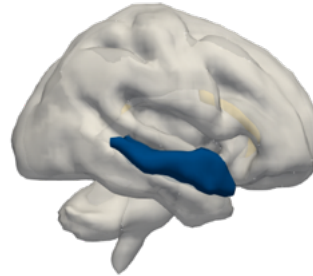
Axial slice visualisation of the functional grey matter network representing *hearing*, overlaid onto the standard MNI152 template. The labelled co-ordinates map to MNI space. The colours label functional subnetworks separated by microarray gene expression, here represented in yellow and blue. This forms the basis upon which treatment effect heterogeneity is simulated, with hypothetical treatments selectively effective for lesions disrupting defined subnetworks.

S10.2.1: *Language* subnetwork render

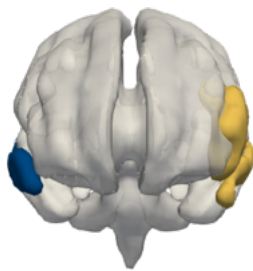
a



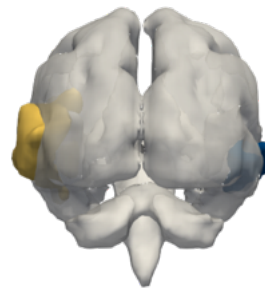
b



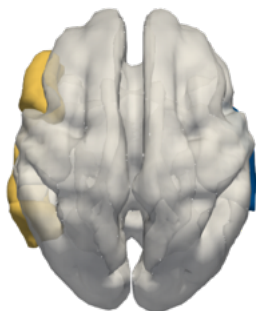
c



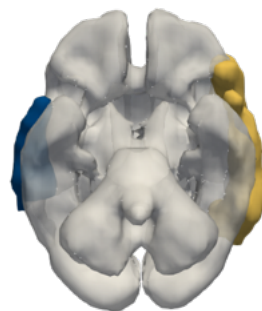
d



e

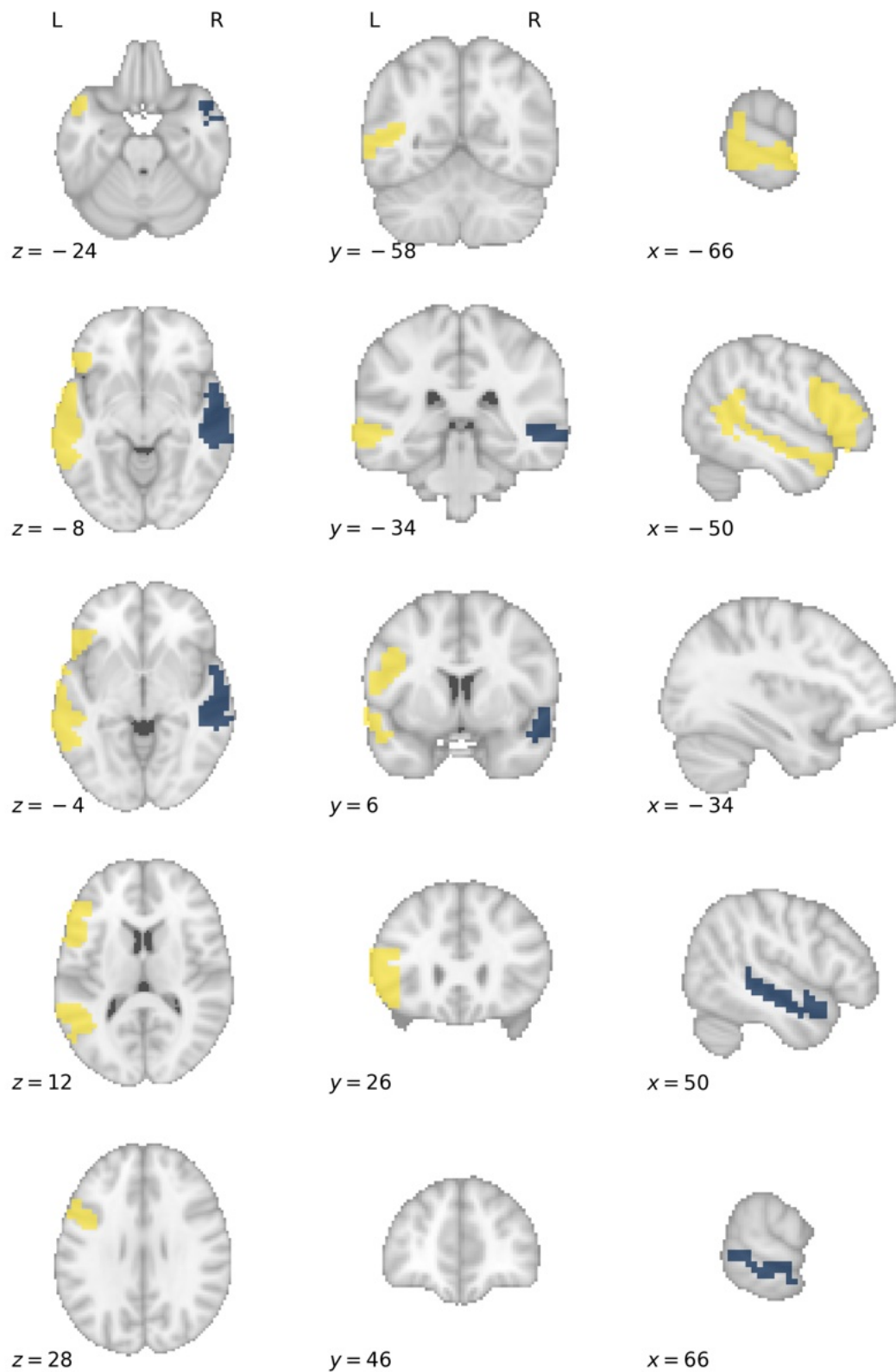


f



Three-dimensional rendering of the functional grey matter network representing *language*. The colours label functional subnetworks separated by microarray gene expression data, here represented in yellow and blue. This forms the basis upon which treatment effect heterogeneity is simulated, with hypothetical treatments selectively effective for lesions disrupting defined subnetworks. Each panel shows the same render from a different spatial perspective: **a**, left; **b**, right; **c**, anterior; **d**, posterior, **e**, superior; **f**, inferior.

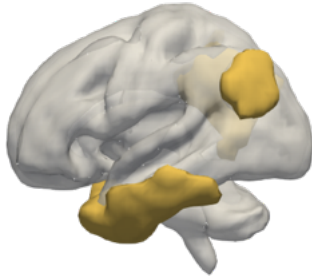
S10.2.2: *Language* subnetwork axial slices



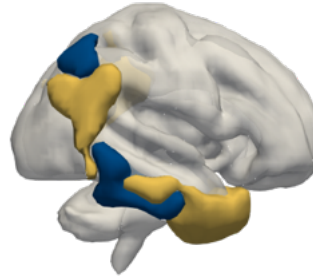
Axial slice visualisation of the functional grey matter network representing *language*, overlaid onto the standard MNI152 template. The labelled co-ordinates map to MNI space. The colours label functional subnetworks separated by microarray gene expression, here represented in yellow and blue. This forms the basis upon which treatment effect heterogeneity is simulated, with hypothetical treatments selectively effective for lesions disrupting defined subnetworks.

S10.3.1: *Introspection* subnetwork render

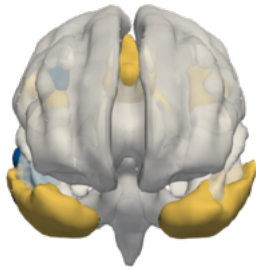
a



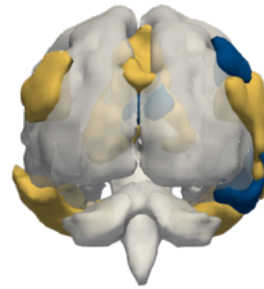
b



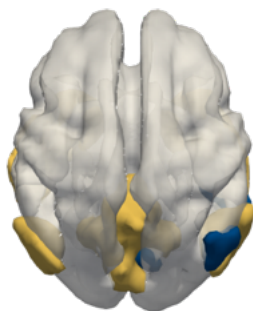
c



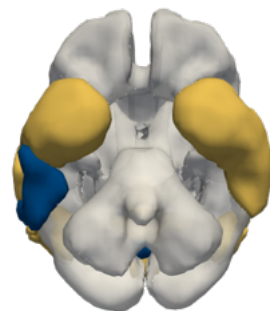
d



e

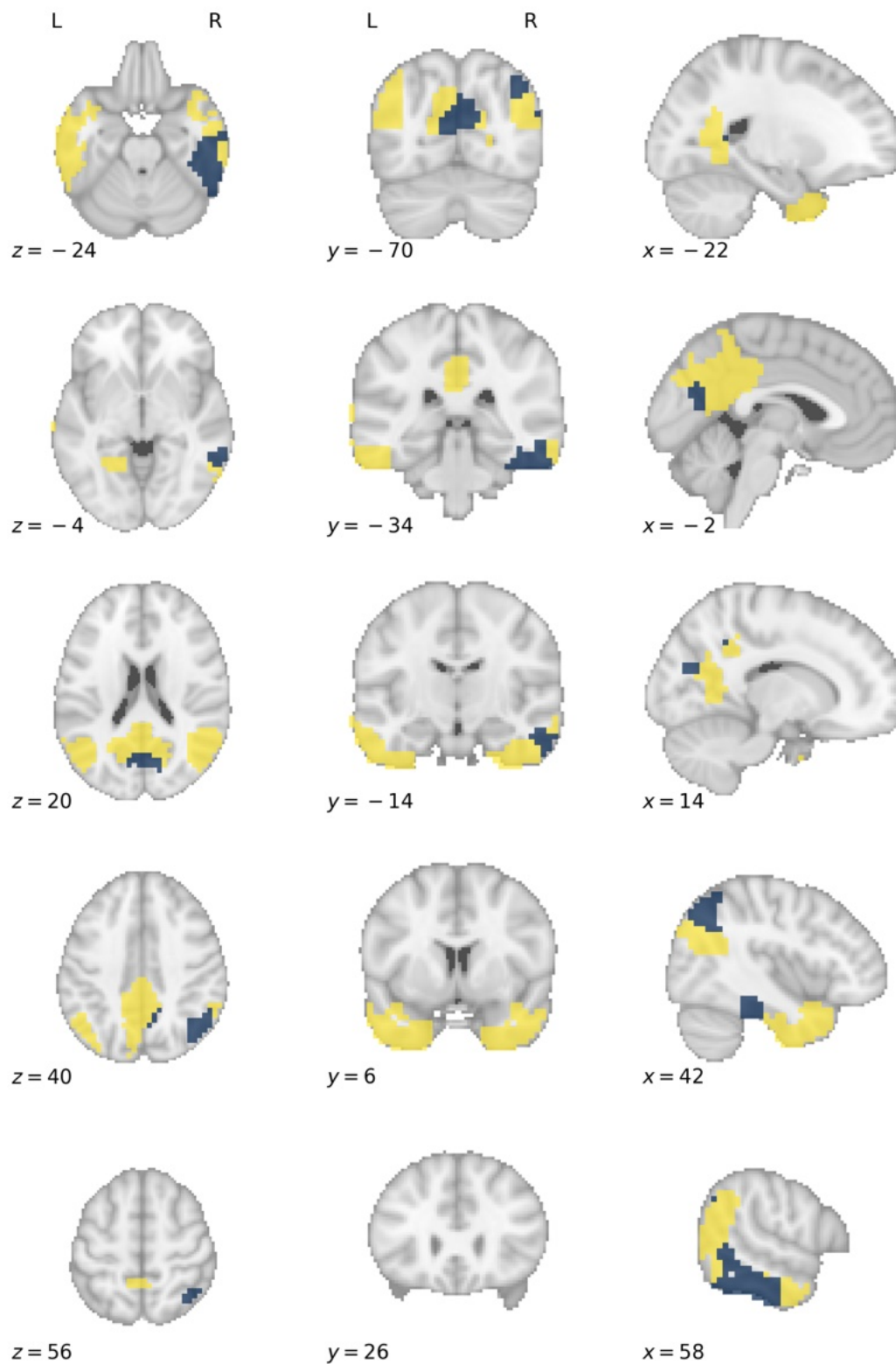


f



Three-dimensional rendering of the functional grey matter network representing *introspection*. The colours label functional subnetworks separated by microarray gene expression data, here represented in yellow and blue. This forms the basis upon which treatment effect heterogeneity is simulated, with hypothetical treatments selectively effective for lesions disrupting defined subnetworks. Each panel shows the same render from a different spatial perspective: **a**, left; **b**, right; **c**, anterior; **d**, posterior, **e**, superior; **f**, inferior.

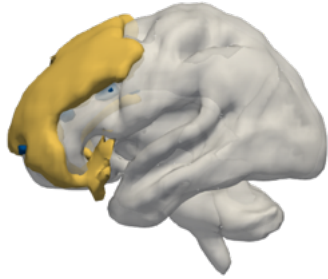
S10.3.2: *Introspection* subnetwork axial slices



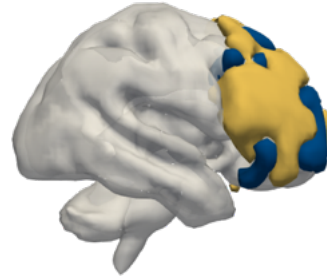
Axial slice visualisation of the functional grey matter network representing *introspection*, overlaid onto the standard MNI152 template. The labelled co-ordinates map to MNI space. The colours label functional subnetworks separated by microarray gene expression, here represented in yellow and blue. This forms the basis upon which treatment effect heterogeneity is simulated, with hypothetical treatments selectively effective for lesions disrupting defined subnetworks.

S10.4.1: *Cognition* subnetwork render

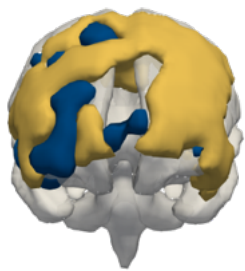
a



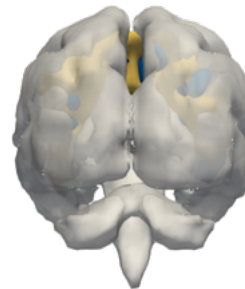
b



c



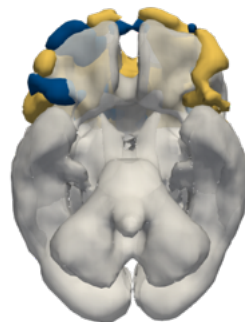
d



e

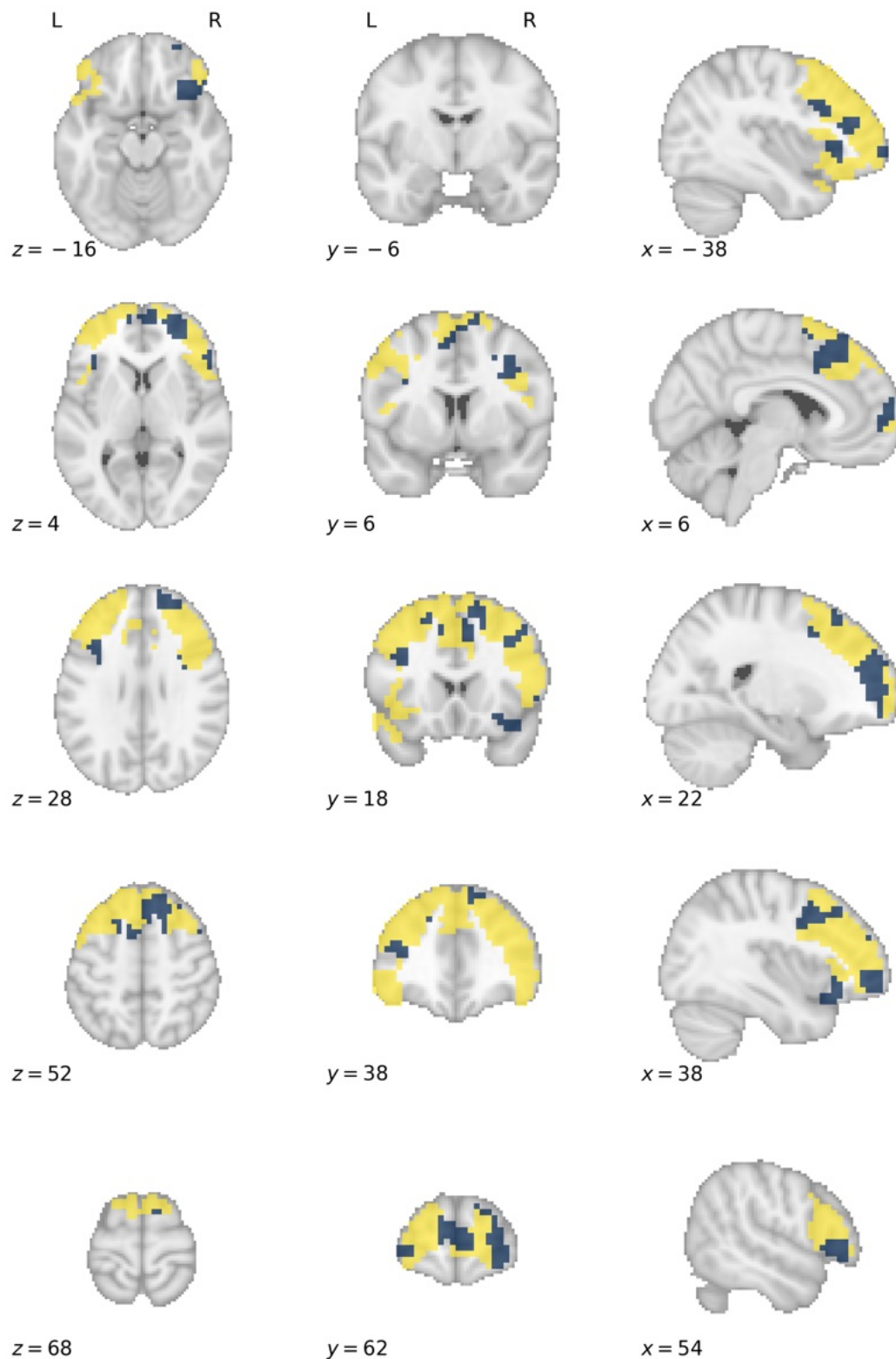


f



Three-dimensional rendering of the functional grey matter network representing *cognition*. The colours label functional subnetworks separated by microarray gene expression data, here represented in yellow and blue. This forms the basis upon which treatment effect heterogeneity is simulated, with hypothetical treatments selectively effective for lesions disrupting defined subnetworks. Each panel shows the same render from a different spatial perspective: **a**, left; **b**, right; **c**, anterior; **d**, posterior, **e**, superior; **f**, inferior.

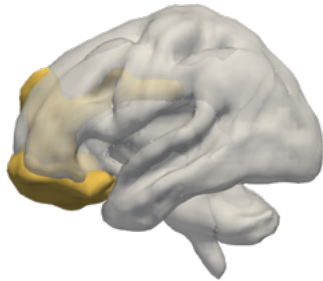
S10.4.2: *Cognition* subnetwork axial slices



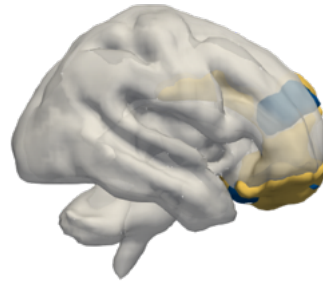
Axial slice visualisation of the functional grey matter network representing *cognition*, overlaid onto the standard MNI152 template. The labelled co-ordinates map to MNI space. The colours label functional subnetworks separated by microarray gene expression, here represented in yellow and blue. This forms the basis upon which treatment effect heterogeneity is simulated, with hypothetical treatments selectively effective for lesions disrupting defined subnetworks.

S10.5.1: *Mood* subnetwork render

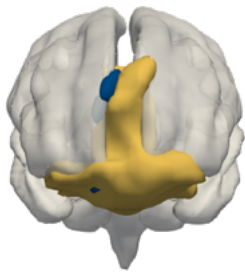
a



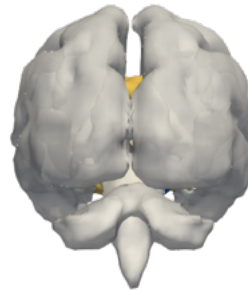
b



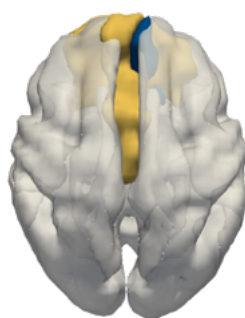
c



d



e

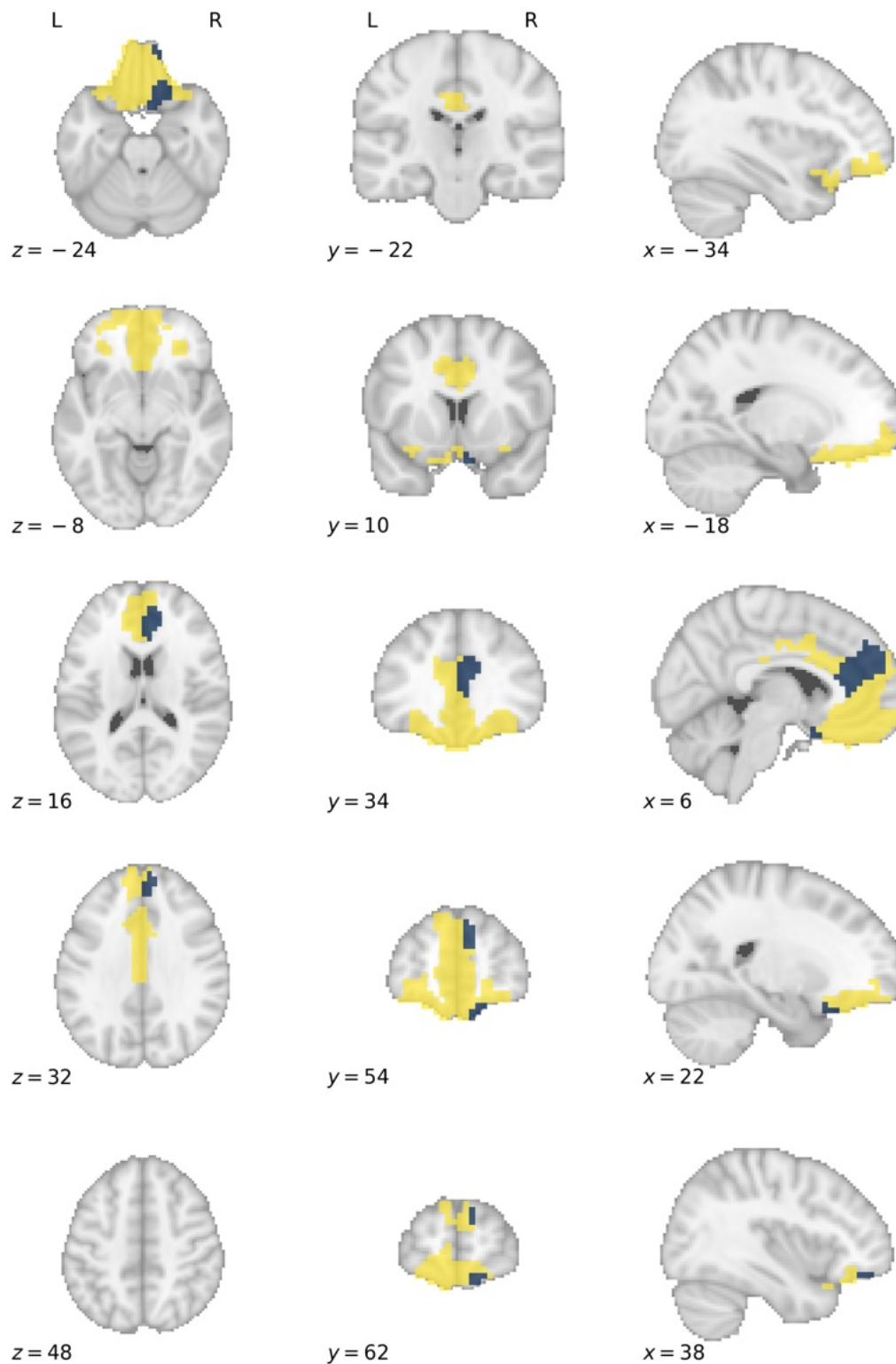


f



Three-dimensional rendering of the functional grey matter network representing *mood*. The colours label functional subnetworks separated by microarray gene expression data, here represented in yellow and blue. This forms the basis upon which treatment effect heterogeneity is simulated, with hypothetical treatments selectively effective for lesions disrupting defined subnetworks. Each panel shows the same render from a different spatial perspective: **a**, left; **b**, right; **c**, anterior; **d**, posterior; **e**, superior; **f**, inferior.

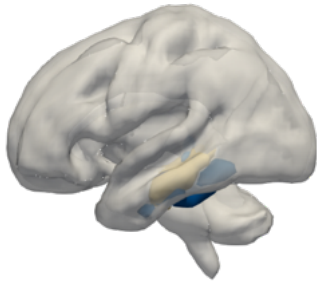
S10.5.2: *Mood* subnetwork axial slices



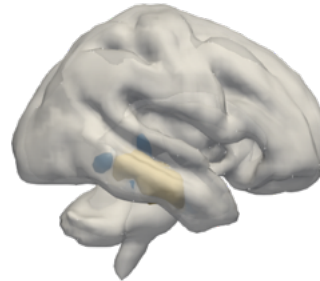
Axial slice visualisation of the functional grey matter network representing *mood*, overlaid onto the standard MNI152 template. The labelled co-ordinates map to MNI space. The colours label functional subnetworks separated by microarray gene expression, here represented in yellow and blue. This forms the basis upon which treatment effect heterogeneity is simulated, with hypothetical treatments selectively effective for lesions disrupting defined subnetworks.

S10.6.1: *Memory* subnetwork render

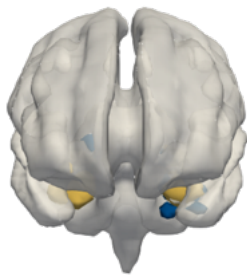
a



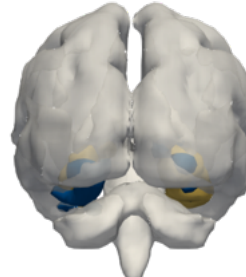
b



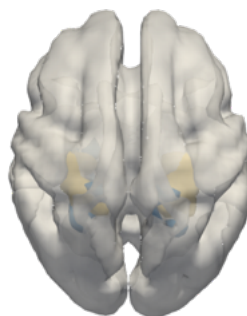
c



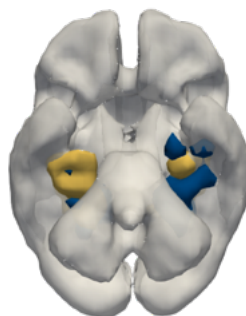
d



e

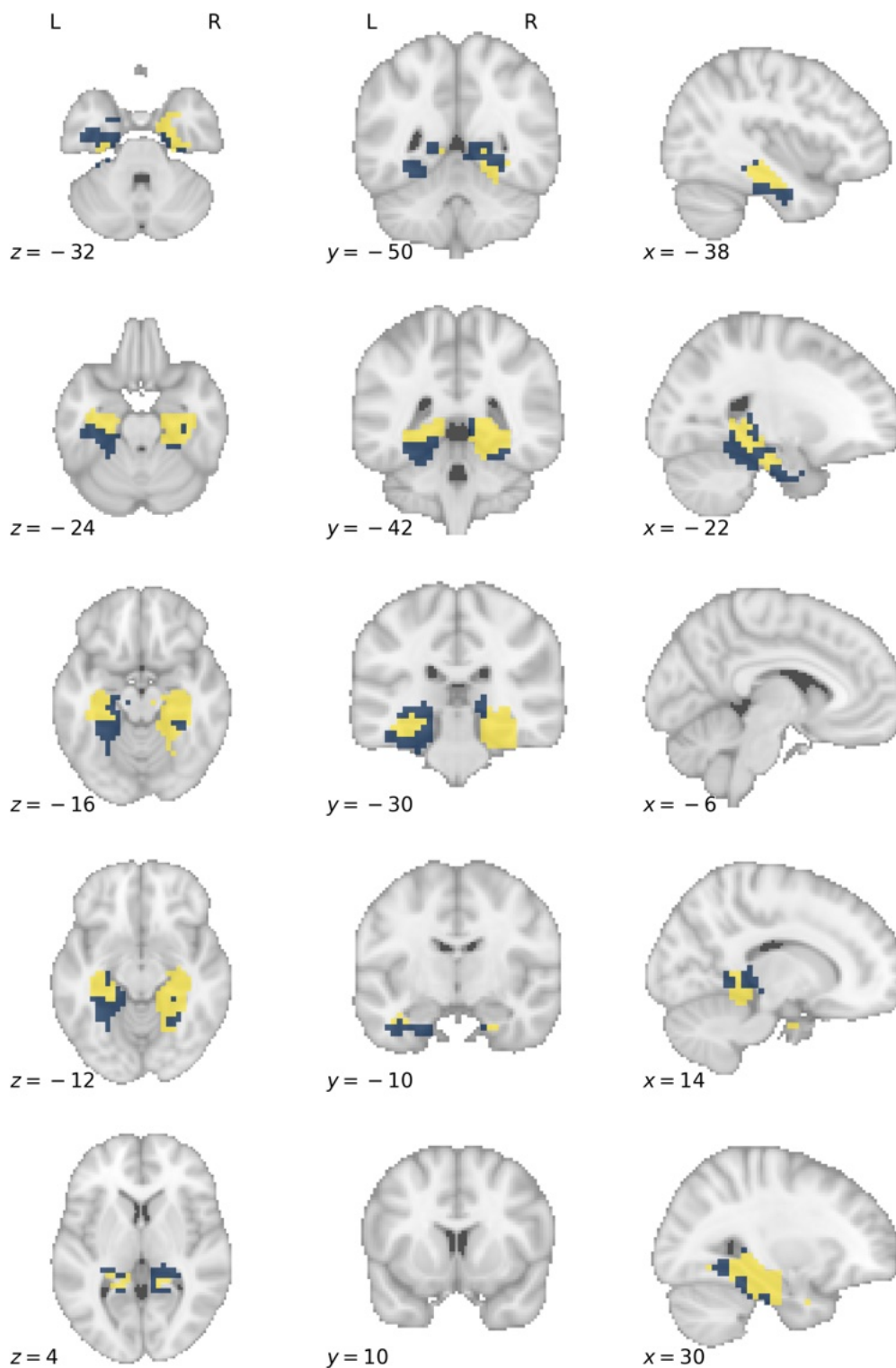


f



Three-dimensional rendering of the functional grey matter network representing *memory*. The colours label functional subnetworks separated by microarray gene expression data, here represented in yellow and blue. This forms the basis upon which treatment effect heterogeneity is simulated, with hypothetical treatments selectively effective for lesions disrupting defined subnetworks. Each panel shows the same render from a different spatial perspective: **a**, left; **b**, right; **c**, anterior; **d**, posterior; **e**, superior; **f**, inferior.

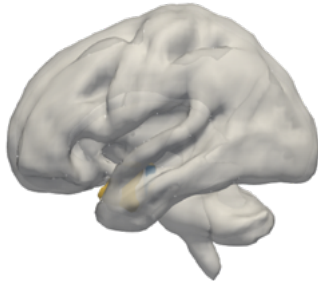
S10.6.2: *Memory* subnetwork axial slices



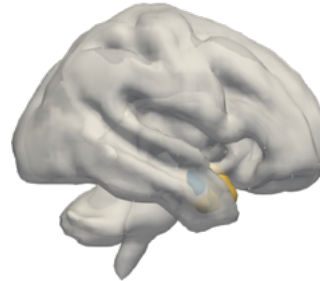
Axial slice visualisation of the functional grey matter network representing *memory*, overlaid onto the standard MNI152 template. The labelled co-ordinates map to MNI space. The colours label functional subnetworks separated by microarray gene expression, here represented in yellow and blue. This forms the basis upon which treatment effect heterogeneity is simulated, with hypothetical treatments selectively effective for lesions disrupting defined subnetworks.

S10.7.1: *Aversion* subnetwork render

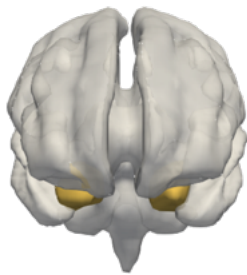
a



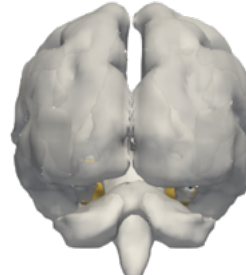
b



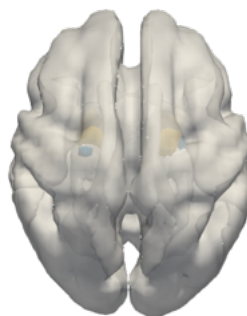
c



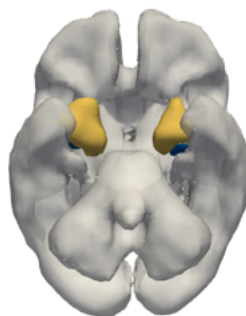
d



e

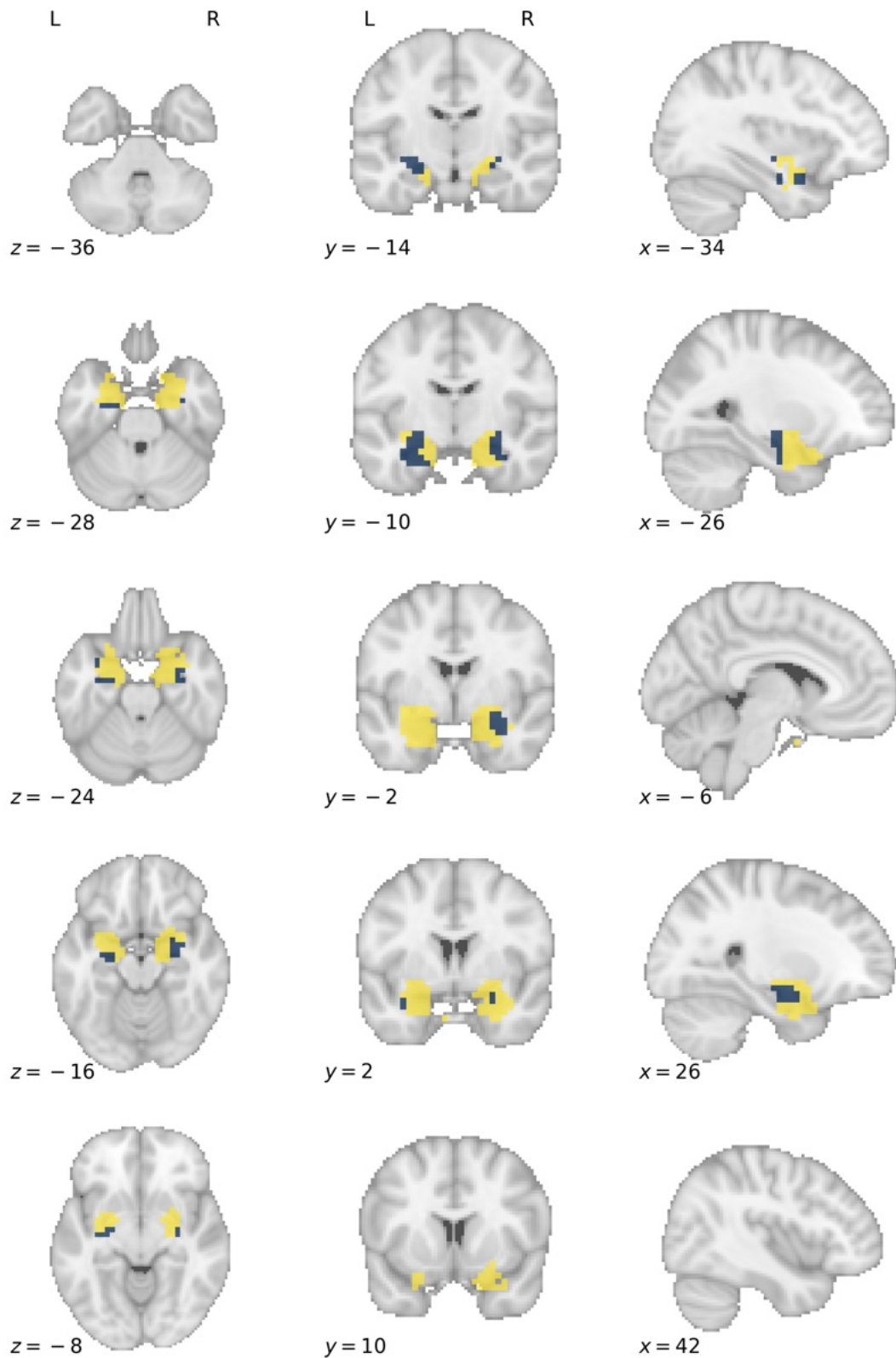


f



Three-dimensional rendering of the functional grey matter network representing *aversion*. The colours label functional subnetworks separated by microarray gene expression data, here represented in yellow and blue. This forms the basis upon which treatment effect heterogeneity is simulated, with hypothetical treatments selectively effective for lesions disrupting defined subnetworks. Each panel shows the same render from a different spatial perspective: **a**, left; **b**, right; **c**, anterior; **d**, posterior; **e**, superior; **f**, inferior.

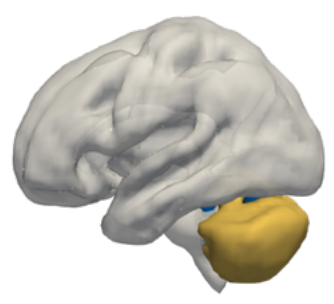
S10.7.2: *Aversion* subnetwork axial slices



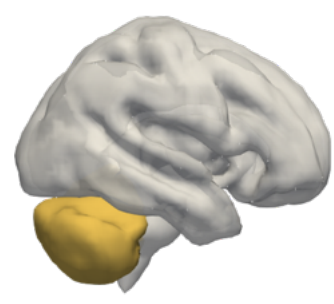
Axial slice visualisation of the functional grey matter network representing *aversion*, overlaid onto the standard MNI152 template. The labelled co-ordinates map to MNI space. The colours label functional subnetworks separated by microarray gene expression, here represented in yellow and blue. This forms the basis upon which treatment effect heterogeneity is simulated, with hypothetical treatments selectively effective for lesions disrupting defined subnetworks.

S10.8.1: *Coordination* subnetwork render

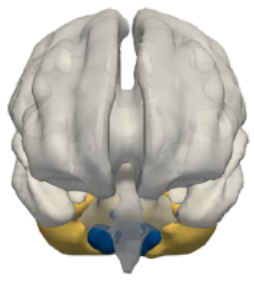
a



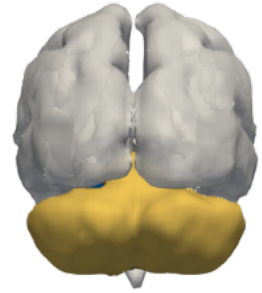
b



c



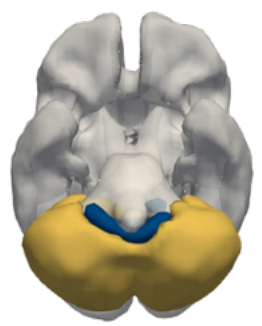
d



e

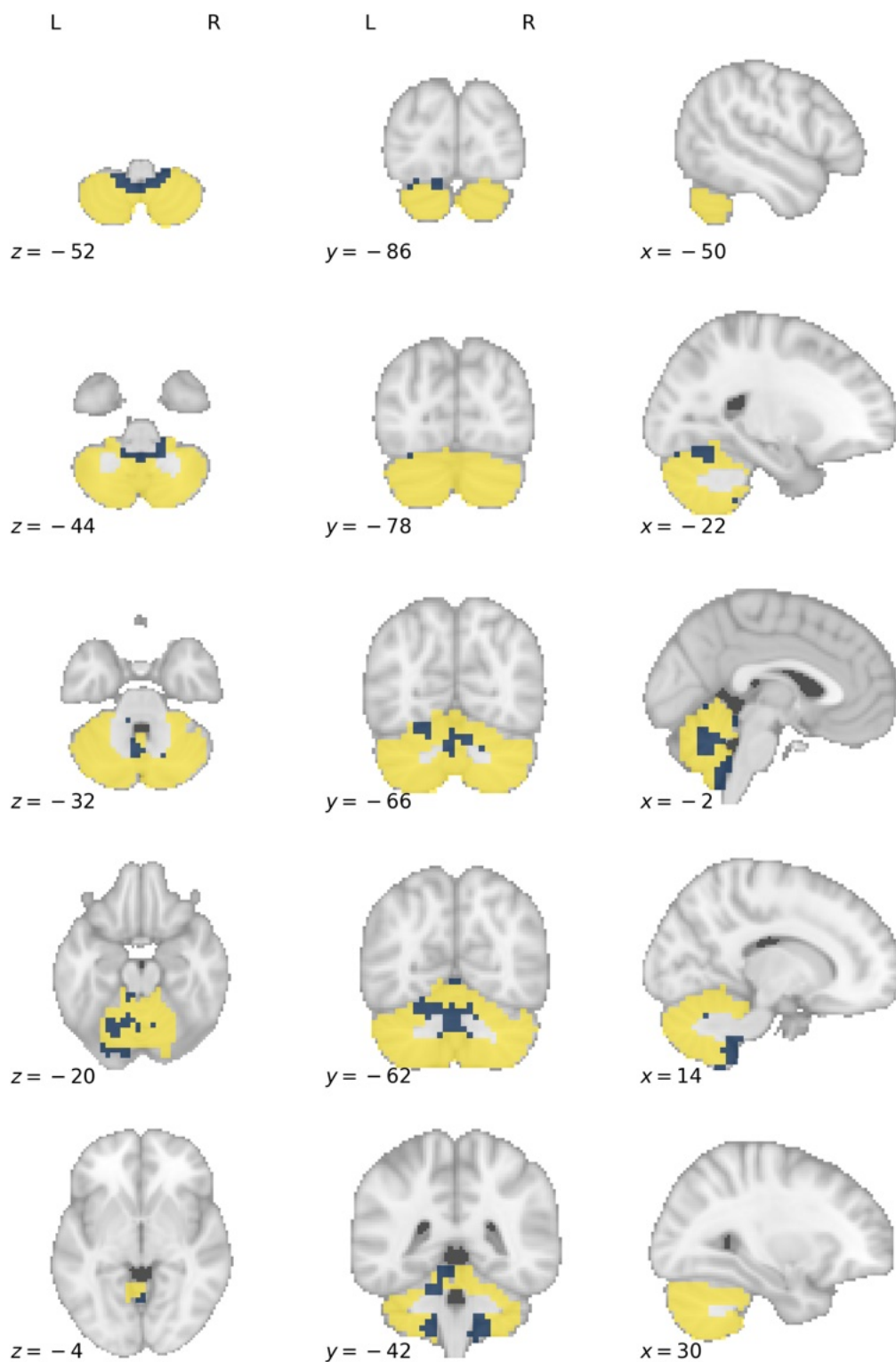


f



Three-dimensional rendering of the functional grey matter network representing *coordination*. The colours label functional subnetworks separated by microarray gene expression data, here represented in yellow and blue. This forms the basis upon which treatment effect heterogeneity is simulated, with hypothetical treatments selectively effective for lesions disrupting defined subnetworks. Each panel shows the same render from a different spatial perspective: **a**, left; **b**, right; **c**, anterior; **d**, posterior; **e**, superior; **f**, inferior.

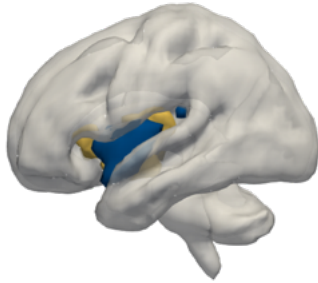
S10.8.2: *Coordination* subnetwork axial slices



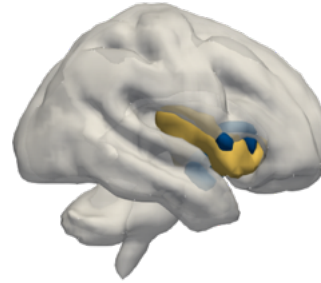
Axial slice visualisation of the functional grey matter network representing *coordination*, overlaid onto the standard MNI152 template. The labelled co-ordinates map to MNI space. The colours label functional subnetworks separated by microarray gene expression, here represented in yellow and blue. This forms the basis upon which treatment effect heterogeneity is simulated, with hypothetical treatments selectively effective for lesions disrupting defined subnetworks.

S10.9.1: *Interoception* subnetwork render

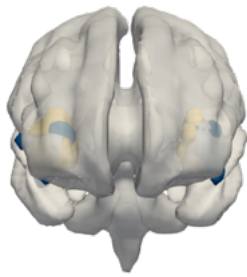
a



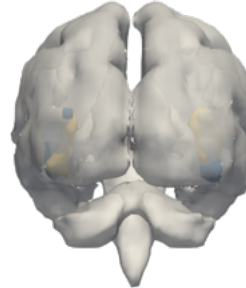
b



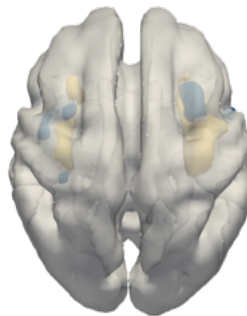
c



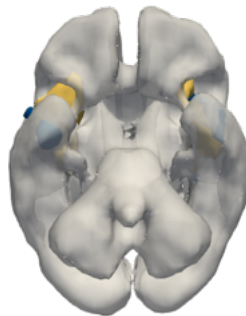
d



e

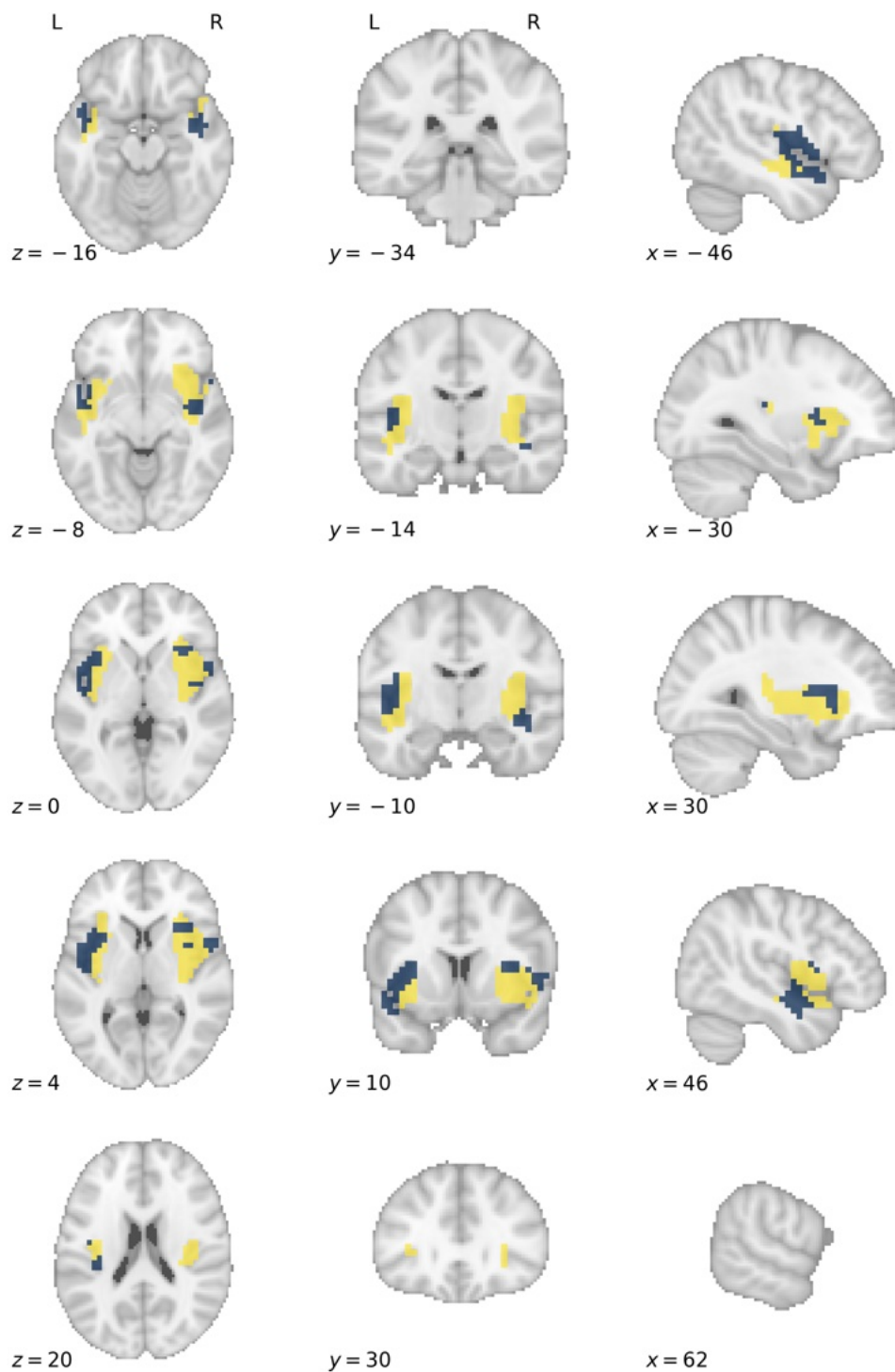


f



Three-dimensional rendering of the functional grey matter network representing *interoception*. The colours label functional subnetworks separated by microarray gene expression data, here represented in yellow and blue. This forms the basis upon which treatment effect heterogeneity is simulated, with hypothetical treatments selectively effective for lesions disrupting defined subnetworks. Each panel shows the same render from a different spatial perspective: **a**, left; **b**, right; **c**, anterior; **d**, posterior; **e**, superior; **f**, inferior.

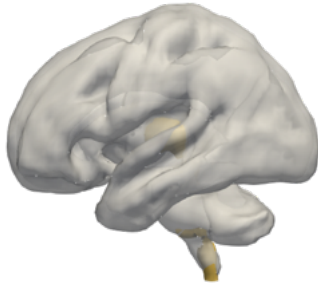
S10.9.2: *Interoception* subnetwork axial slices



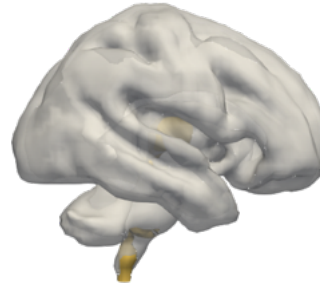
Axial slice visualisation of the functional grey matter network representing *interoception*, overlaid onto the standard MNI152 template. The labelled co-ordinates map to MNI space. The colours label functional subnetworks separated by microarray gene expression, here represented in yellow and blue. This forms the basis upon which treatment effect heterogeneity is simulated, with hypothetical treatments selectively effective for lesions disrupting defined subnetworks.

S10.10.1: *Sleep* subnetwork render

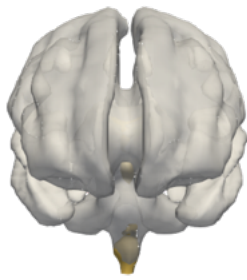
a



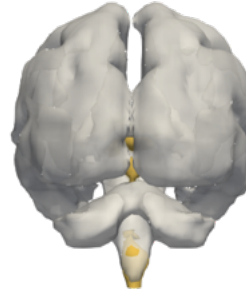
b



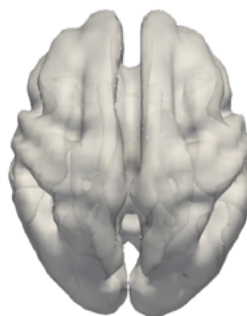
c



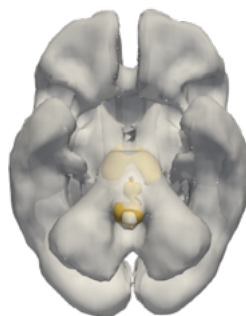
d



e

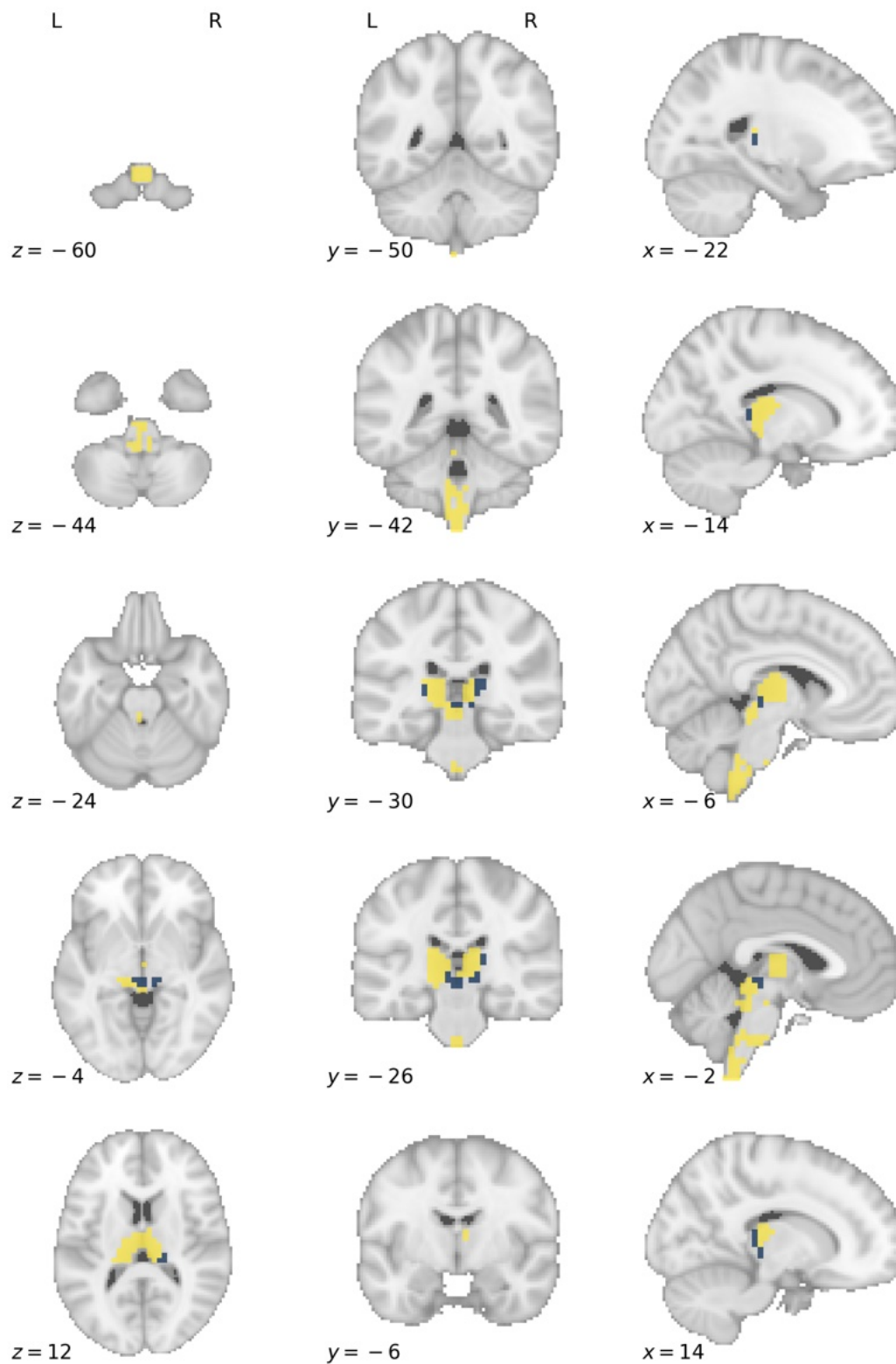


f



Three-dimensional rendering of the functional grey matter network representing *sleep*. The colours label functional subnetworks separated by microarray gene expression data, here represented in yellow and blue. This forms the basis upon which treatment effect heterogeneity is simulated, with hypothetical treatments selectively effective for lesions disrupting defined subnetworks. Each panel shows the same render from a different spatial perspective: **a**, left; **b**, right; **c**, anterior; **d**, posterior; **e**, superior; **f**, inferior.

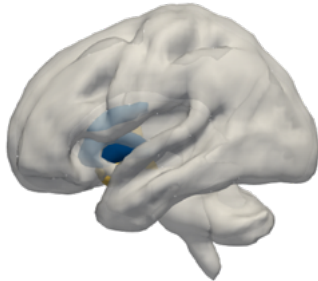
S10.10.2: *Sleep* subnetwork axial slices



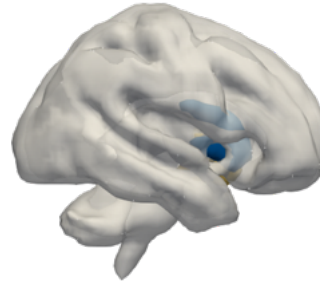
Axial slice visualisation of the functional grey matter network representing *sleep*, overlaid onto the standard MNI152 template. The labelled co-ordinates map to MNI space. The colours label functional subnetworks separated by microarray gene expression, here represented in yellow and blue. This forms the basis upon which treatment effect heterogeneity is simulated, with hypothetical treatments selectively effective for lesions disrupting defined subnetworks.

S10.11.1: *Reward* subnetwork render

a



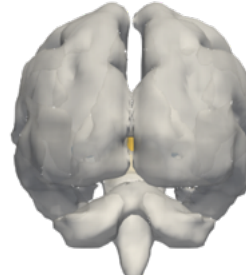
b



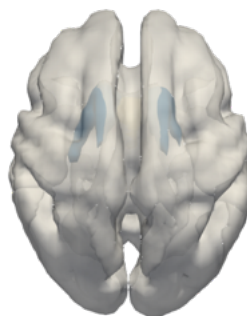
c



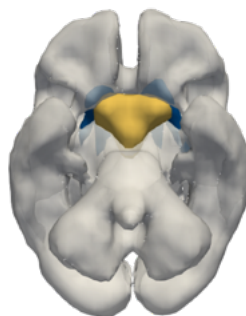
d



e

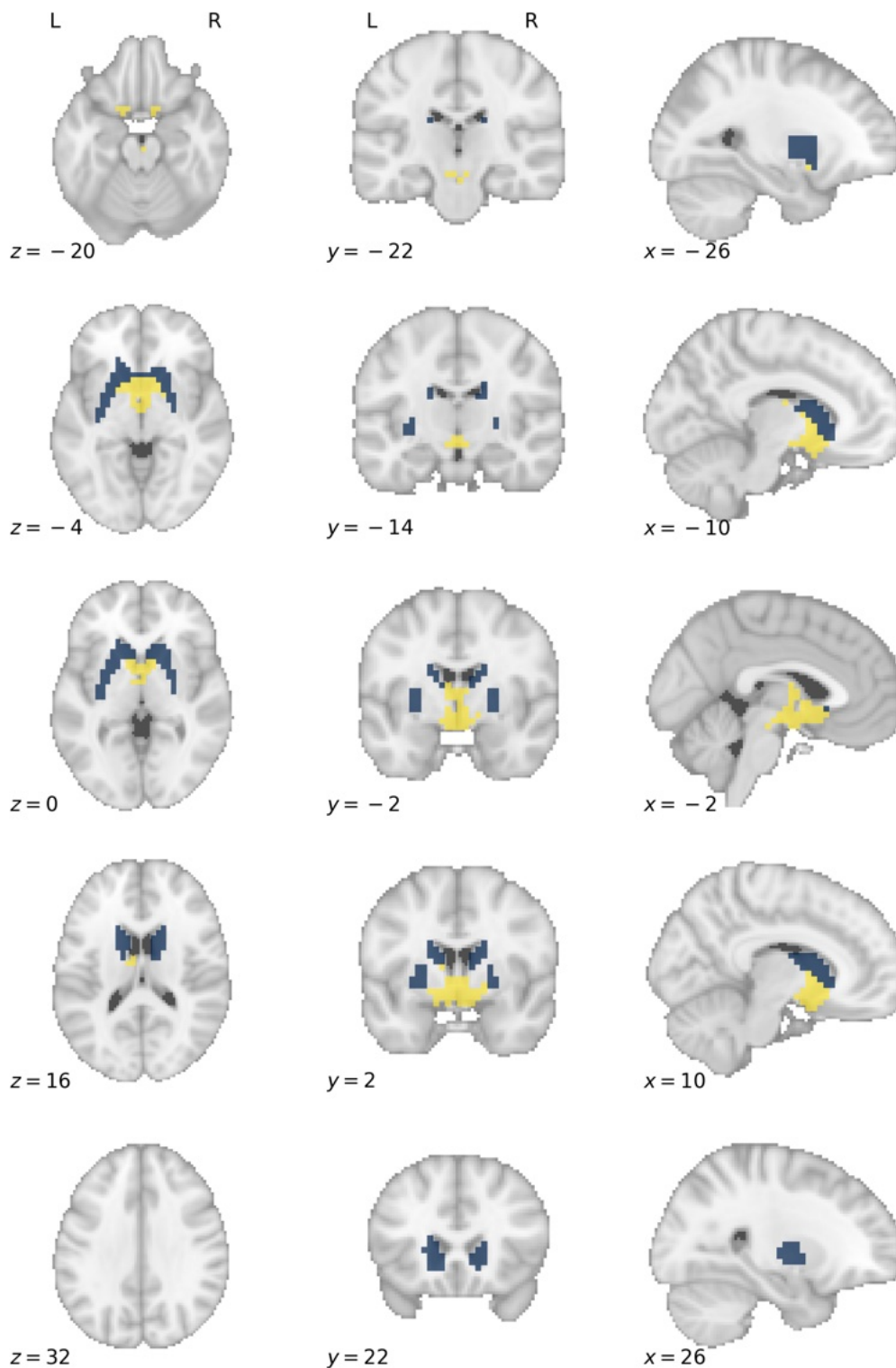


f



Three-dimensional rendering of the functional grey matter network representing *reward*. The colours label functional subnetworks separated by microarray gene expression data, here represented in yellow and blue. This forms the basis upon which treatment effect heterogeneity is simulated, with hypothetical treatments selectively effective for lesions disrupting defined subnetworks. Each panel shows the same render from a different spatial perspective: **a**, left; **b**, right; **c**, anterior; **d**, posterior, **e**, superior; **f**, inferior.

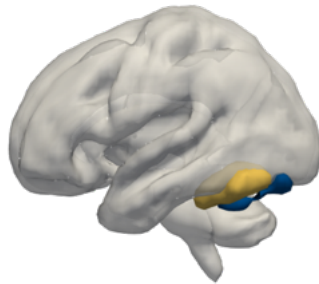
S10.11.2: *Reward* subnetwork axial slices



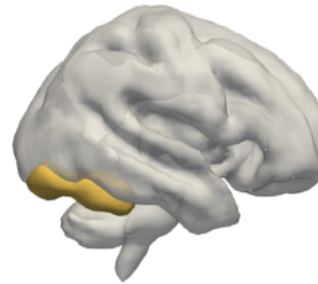
Axial slice visualisation of the functional grey matter network representing *reward*, overlaid onto the standard MNI152 template. The labelled co-ordinates map to MNI space. The colours label functional subnetworks separated by microarray gene expression, here represented in yellow and blue. This forms the basis upon which treatment effect heterogeneity is simulated, with hypothetical treatments selectively effective for lesions disrupting defined subnetworks.

S10.12.1: *Visual Recognition* subnetwork render

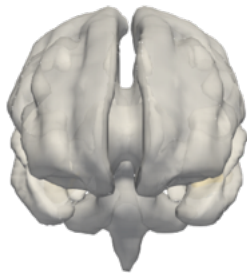
a



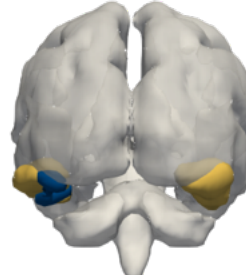
b



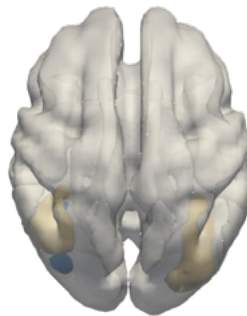
c



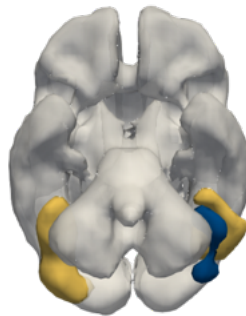
d



e

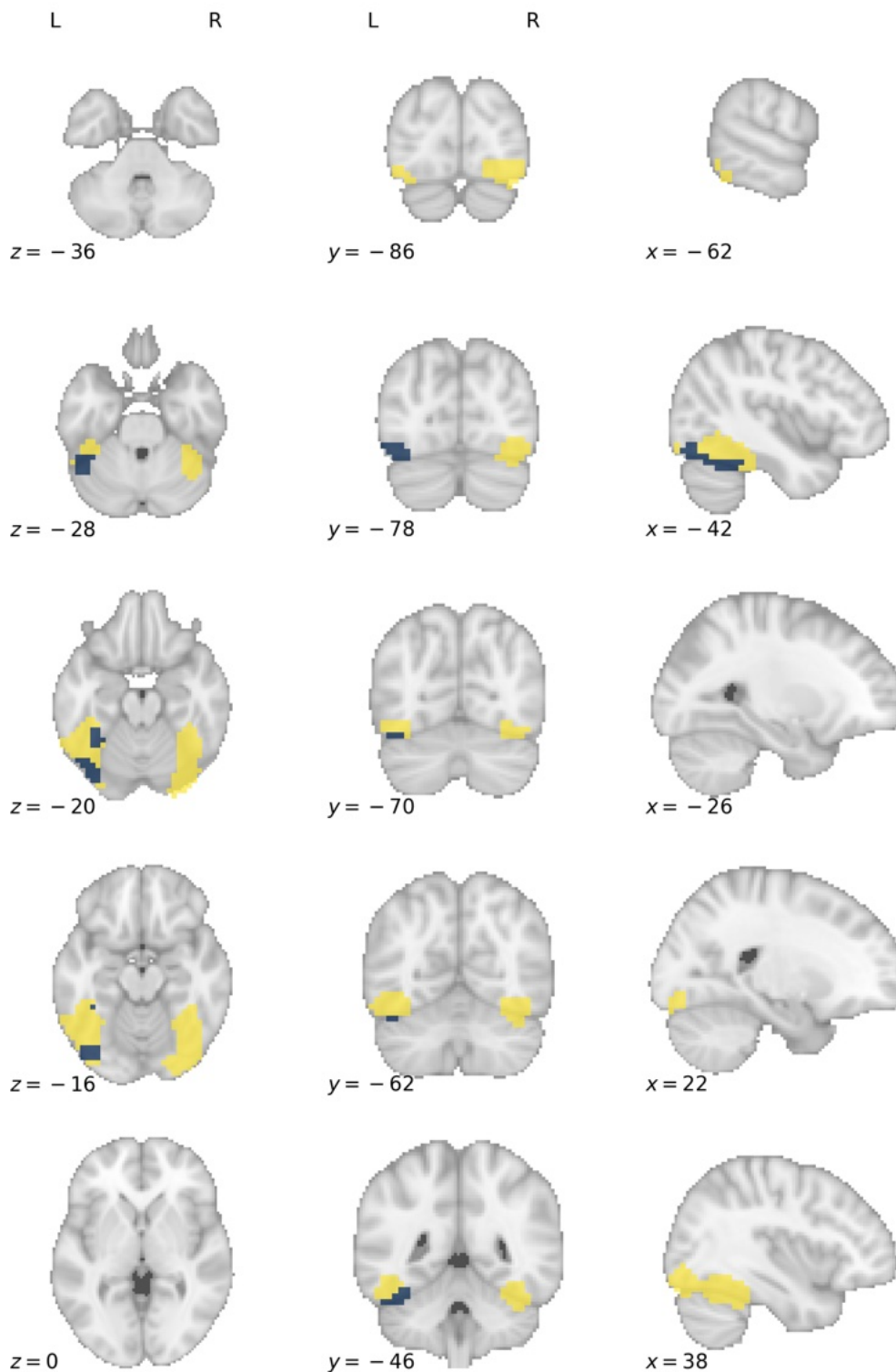


f



Three-dimensional rendering of the functional grey matter network representing *visual recognition*. The colours label functional subnetworks separated by microarray gene expression data, here represented in yellow and blue. This forms the basis upon which treatment effect heterogeneity is simulated, with hypothetical treatments selectively effective for lesions disrupting defined subnetworks. Each panel shows the same render from a different spatial perspective: **a**, left; **b**, right; **c**, anterior; **d**, posterior; **e**, superior; **f**, inferior.

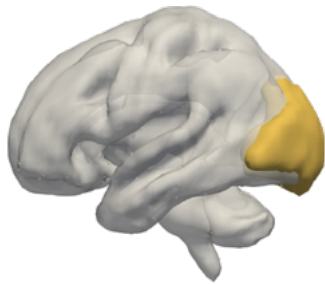
S10.12.2: *Visual Recognition* subnetwork axial slices



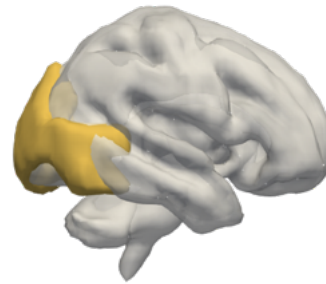
Axial slice visualisation of the functional grey matter network representing *visual recognition*, overlaid onto the standard MNI152 template. The labelled co-ordinates map to MNI space. The colours label functional subnetworks separated by microarray gene expression, here represented in yellow and blue. This forms the basis upon which treatment effect heterogeneity is simulated, with hypothetical treatments selectively effective for lesions disrupting defined subnetworks.

S10.13.1: *Visual Perception* subnetwork render

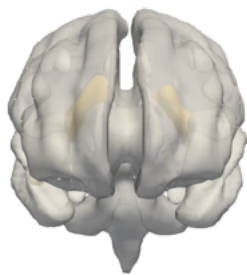
a



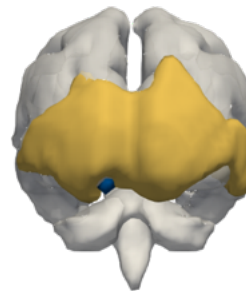
b



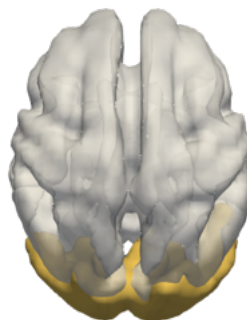
c



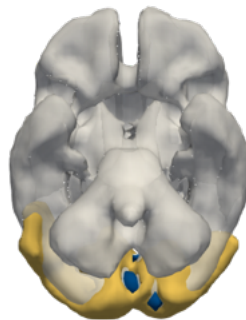
d



e

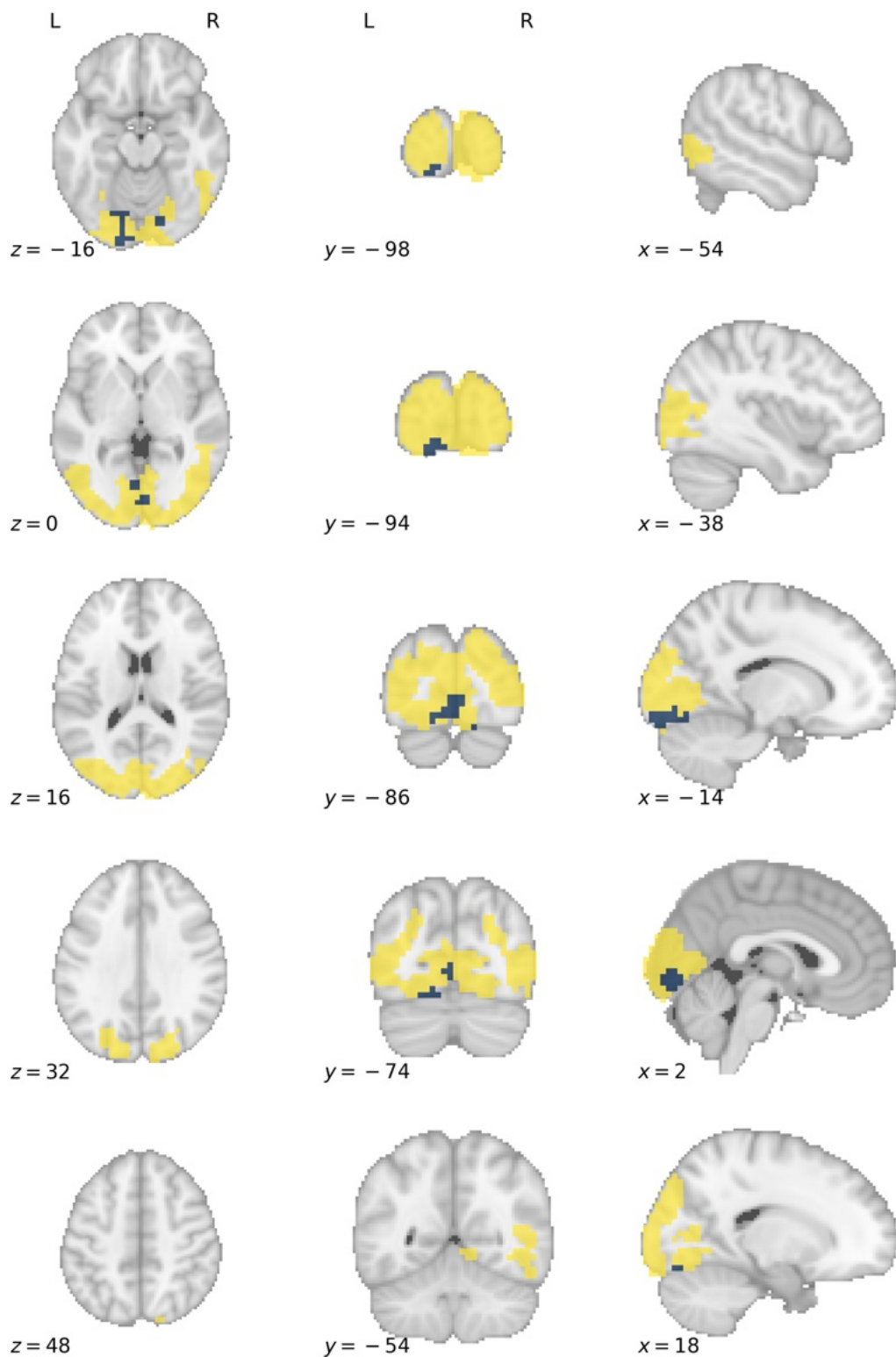


f



Three-dimensional rendering of the functional grey matter network representing *visual perception*. The colours label functional subnetworks separated by microarray gene expression data, here represented in yellow and blue. This forms the basis upon which treatment effect heterogeneity is simulated, with hypothetical treatments selectively effective for lesions disrupting defined subnetworks. Each panel shows the same render from a different spatial perspective: **a**, left; **b**, right; **c**, anterior; **d**, posterior; **e**, superior; **f**, inferior.

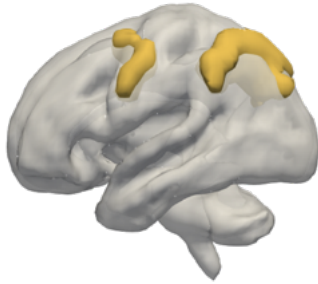
S10.13.2: *Visual Perception* subnetwork axial slices



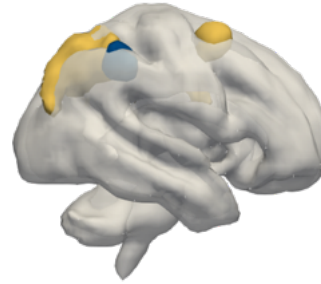
Axial slice visualisation of the functional grey matter network representing *visual perception*, overlaid onto the standard MNI152 template. The labelled co-ordinates map to MNI space. The colours label functional subnetworks separated by microarray gene expression, here represented in yellow and blue. This forms the basis upon which treatment effect heterogeneity is simulated, with hypothetical treatments selectively effective for lesions disrupting defined subnetworks.

S10.14.1: *Spatial Reasoning* subnetwork render

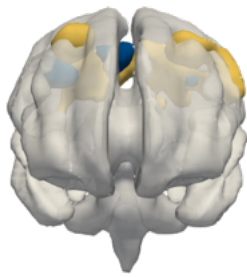
a



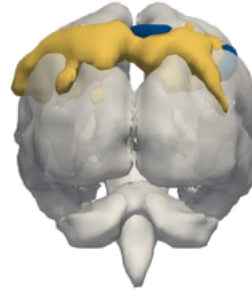
b



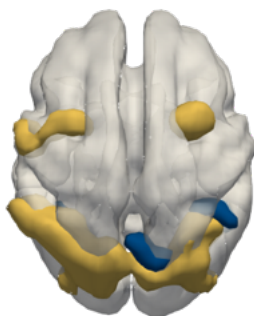
c



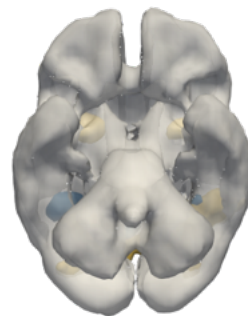
d



e

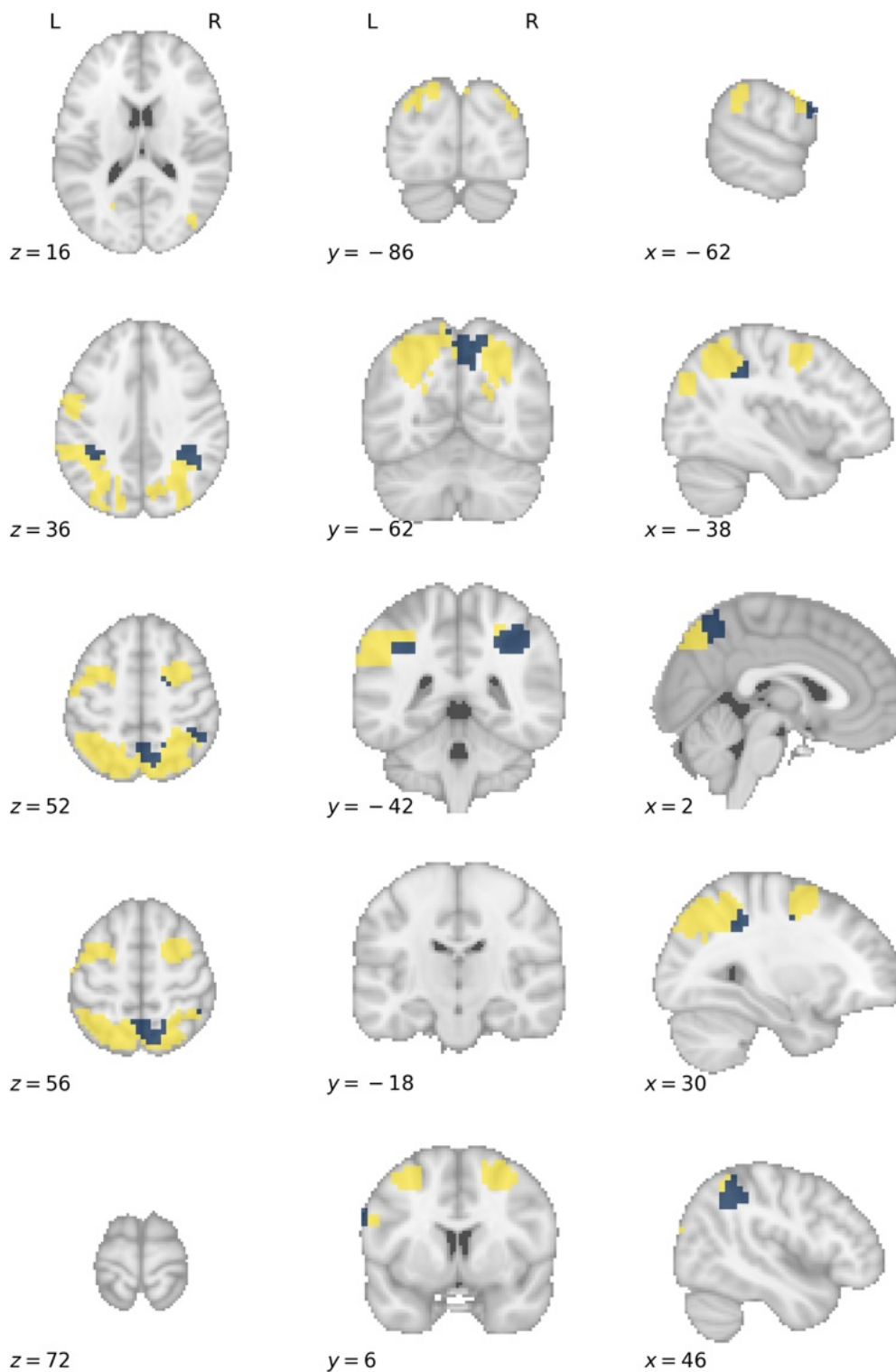


f



Three-dimensional rendering of the functional grey matter network representing *spatial reasoning*. The colours label functional subnetworks separated by microarray gene expression data, here represented in yellow and blue. This forms the basis upon which treatment effect heterogeneity is simulated, with hypothetical treatments selectively effective for lesions disrupting defined subnetworks. Each panel shows the same render from a different spatial perspective: **a**, left; **b**, right; **c**, anterior; **d**, posterior; **e**, superior; **f**, inferior.

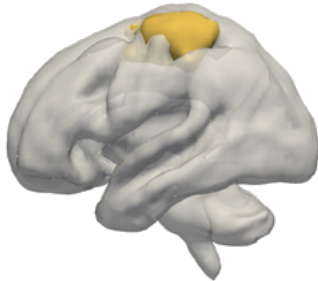
S10.14.2: *Spatial Reasoning* subnetwork axial slices



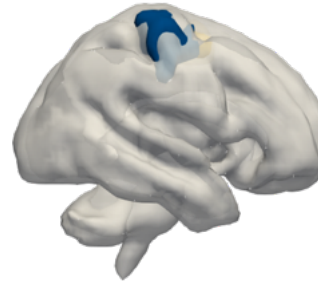
Axial slice visualisation of the functional grey matter network representing *spatial reasoning*, overlaid onto the standard MNI152 template. The labelled co-ordinates map to MNI space. The colours label functional subnetworks separated by microarray gene expression, here represented in yellow and blue. This forms the basis upon which treatment effect heterogeneity is simulated, with hypothetical treatments selectively effective for lesions disrupting defined subnetworks.

S10.15.1: *Motor* subnetwork render

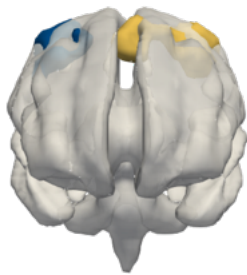
a



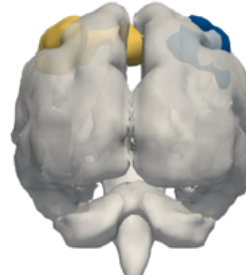
b



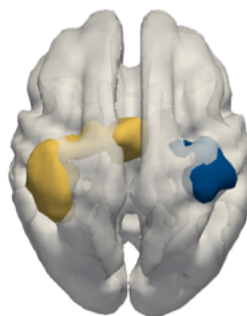
c



d



e

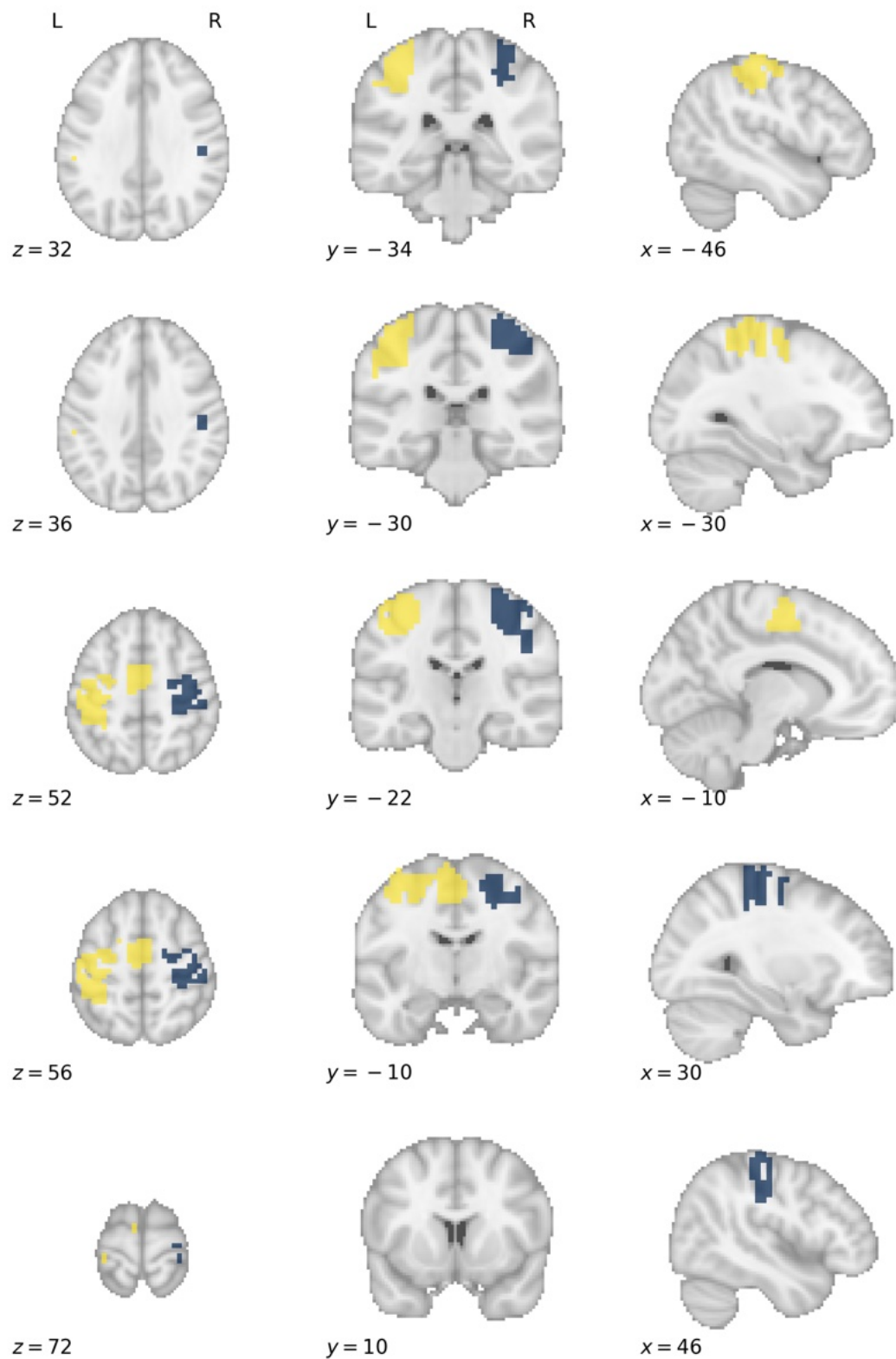


f



Three-dimensional rendering of the functional grey matter network representing *motor behaviour*. The colours label functional subnetworks separated by microarray gene expression data, here represented in yellow and blue. This forms the basis upon which treatment effect heterogeneity is simulated, with hypothetical treatments selectively effective for lesions disrupting defined subnetworks. Each panel shows the same render from a different spatial perspective: **a**, left; **b**, right; **c**, anterior; **d**, posterior; **e**, superior; **f**, inferior.

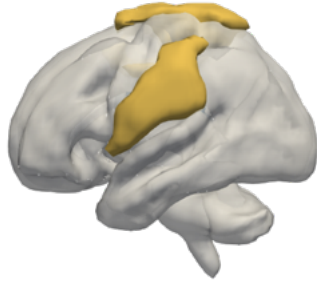
S10.15.2: *Motor* subnetwork axial slices



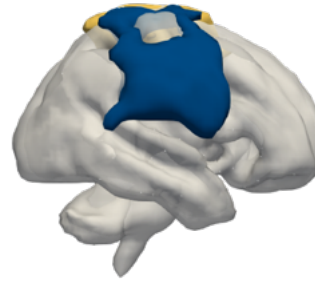
Axial slice visualisation of the functional grey matter network representing *motor behaviour*, overlaid onto the standard MNI152 template. The labelled co-ordinates map to MNI space. The colours label functional subnetworks separated by microarray gene expression, here represented in yellow and blue. This forms the basis upon which treatment effect heterogeneity is simulated, with hypothetical treatments selectively effective for lesions disrupting defined subnetworks.

S10.16.1: *Somatosensory* subnetwork render

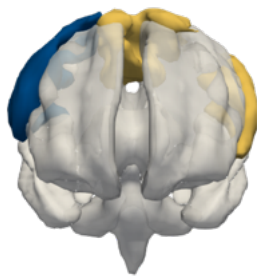
a



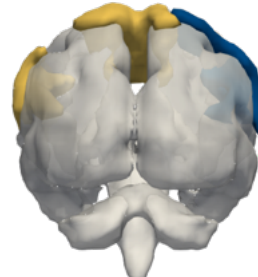
b



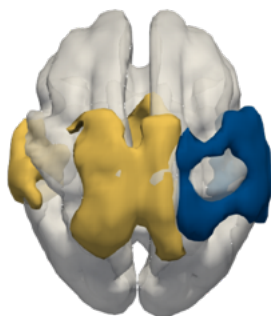
c



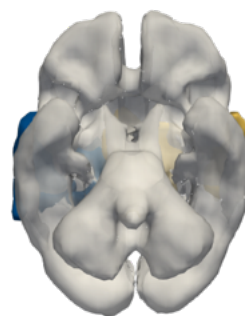
d



e

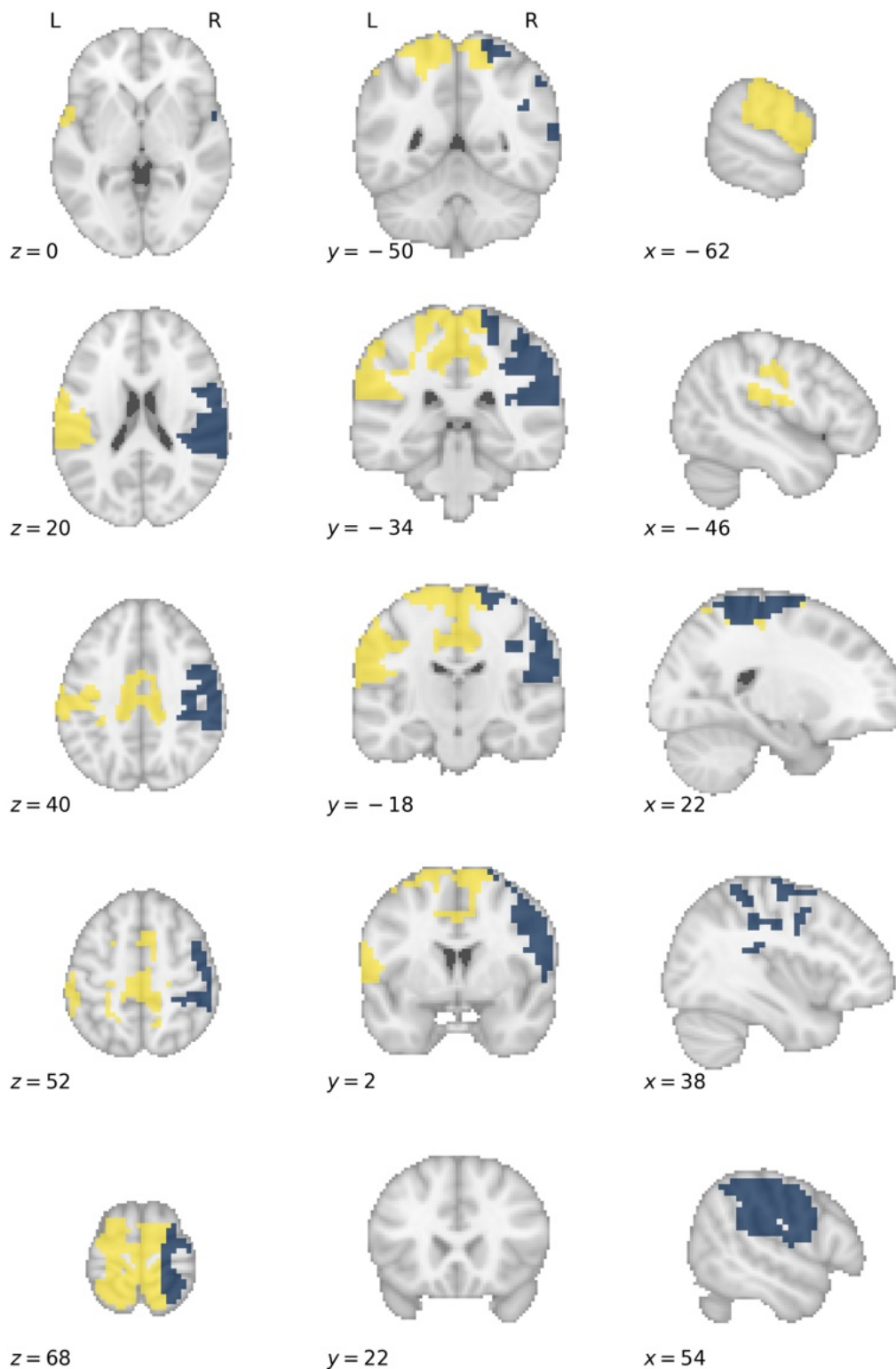


f



Three-dimensional rendering of the functional grey matter network representing *somatosensory function*. The colours label functional subnetworks separated by microarray gene expression data, here represented in yellow and blue. This forms the basis upon which treatment effect heterogeneity is simulated, with hypothetical treatments selectively effective for lesions disrupting defined subnetworks. Each panel shows the same render from a different spatial perspective: **a**, left; **b**, right; **c**, anterior; **d**, posterior; **e**, superior; **f**, inferior.

S10.16.2: Somatosensory subnetwork axial slices



Axial slice visualisation of the functional grey matter network representing *somatosensory function*, overlaid onto the standard MNI152 template. The labelled co-ordinates map to MNI space. The colours label functional subnetworks separated by microarray gene expression, here represented in yellow and blue. This forms the basis upon which treatment effect heterogeneity is simulated, with hypothetical treatments selectively effective for lesions disrupting defined subnetworks.

S11: Lesion representations & location bias results

S11.1: Full results table

Representation	Model	Configuration	Balanced accuracy	PEHE
VAE	ExtraTrees	Two	0.638095	0.670712
VAE	Logistic regression	Two	0.632575	0.706211
VAE	Random forest	Two	0.632377	0.673765
AE	Logistic regression	Two	0.630802	0.711604
AE	ExtraTrees	Two	0.630651	0.676929
PCA	ExtraTrees	Two	0.627552	0.680252
PCA	Random forest	Two	0.625893	0.676612
AE	Random forest	Two	0.624254	0.678743
VAE	ExtraTrees	One	0.620283	0.695618
VAE	XGBoost	Two	0.620071	0.712113
PCA	XGBoost	Two	0.618296	0.714805
AE	XGBoost	Two	0.615551	0.715816
AE	ExtraTrees	One	0.614499	0.697340
PCA	ExtraTrees	One	0.613021	0.694528
PCA	Logistic regression	Two	0.612483	0.731578
NMF	ExtraTrees	Two	0.604669	0.705303
NMF	ExtraTrees	One	0.603761	0.705476
NMF	Random forest	Two	0.600153	0.700542
NMF	Random forest	One	0.580878	0.725727
VAE	Random forest	One	0.578627	0.730461
AE	Random forest	One	0.576798	0.729762
PCA	Random forest	One	0.575839	0.730990
NMF	XGBoost	Two	0.570808	0.756893
AE	XGBoost	One	0.560585	0.715964
VAE	XGBoost	One	0.559008	0.716564
PCA	XGBoost	One	0.555964	0.715761
VAE	Gaussian process	One	0.553557	0.759963
NMF	XGBoost	One	0.553063	0.720112
VAE	Gaussian process	Two	0.550553	0.758173
NMF	Gaussian process	Two	0.532766	0.712642
NMF	Logistic regression	Two	0.531445	0.709866
NMF	Gaussian process	One	0.528550	0.713111
AE	Gaussian process	One	0.527859	0.760956
PCA	Gaussian process	One	0.527066	0.757244
PCA	Gaussian process	Two	0.526727	0.755334
AE	Gaussian process	Two	0.525933	0.759227
PCA	Logistic regression	One	0.484691	0.726026
AE	Logistic regression	One	0.484600	0.726624
VAE	Logistic regression	One	0.484444	0.725735
NMF	Logistic regression	One	0.484085	0.724560

S11.2: Optimal model by balanced accuracy: VAE, two-model ExtraTrees

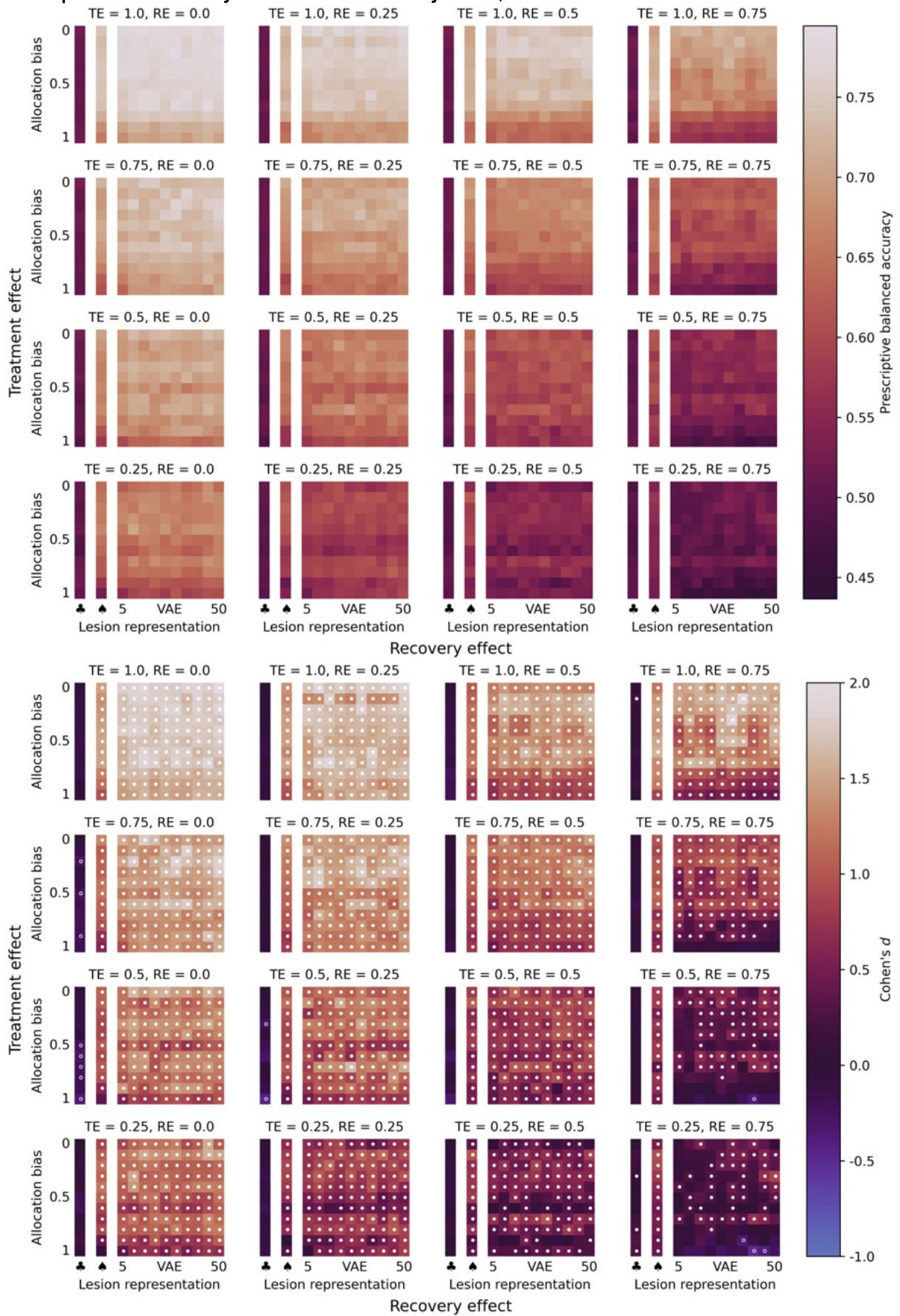


Figure S11.2. Performance comparison of models with lesion representations: balanced accuracy (upper panel) and statistical analysis (lower panel). Prescriptive performance of an optimized, extremely randomized trees-based treatment recommendation system, given binary lesion representations, across the range of response noise (major axes) and allocation bias (minor y -axes), at various levels of expressivity of the individualized representation quantified by embedding length (minor x -axes). The columns to the left of each minor axis show prescriptive performance when individual phenotypes are represented by classification of major affected arterial territory: anterior or posterior circulation (♣) and ACA/MCA/posterior cerebral artery/VB (♠). The upper left subplot shows performance under zero response noise and the lower right subplot shows performance under the conditions of extremely high response noise. The top row of each subplot shows perfect randomization, with zero allocation bias. The upper panel shows prescriptive performance measured by balanced accuracy—the mean proportion of patients allocated to the treatment for which they are truly responsive—for patients that are exclusively responsive to one treatment.

The lower panel shows Cohen's d -effect sizes, by colour, when comparing the prescriptive performance (measured by balanced accuracy, as shown in the upper panel) against a randomized trial based upon individualized information consisting of the major vascular supply (anterior or posterior circulation), at each respective TE/RE pair. Warm colours show performance greater than the comparative randomized trial, while cool colours show the converse. White shows equivalent performance. Trials marked with a circle indicate an effect size exceeding the critical p -value 0.0423 (as adjusted for multiple comparisons at the 0.05 significance level, according to the Benjamini–Hochberg procedure), corresponding to the t -value in a two-sided independent sample t -test. Filled circles show superiority of the prescriptive model from observational data; unfilled circles show superiority of the randomized trial.

TE: treatment effect; RE: recovery effect; VAE: variational auto-encoder representation; ACA: anterior cerebral artery; MCA: middle cerebral artery; VB: vertebrobasilar artery

S11.3: Best-performing by PEHE: VAE, two-model ExtraTrees

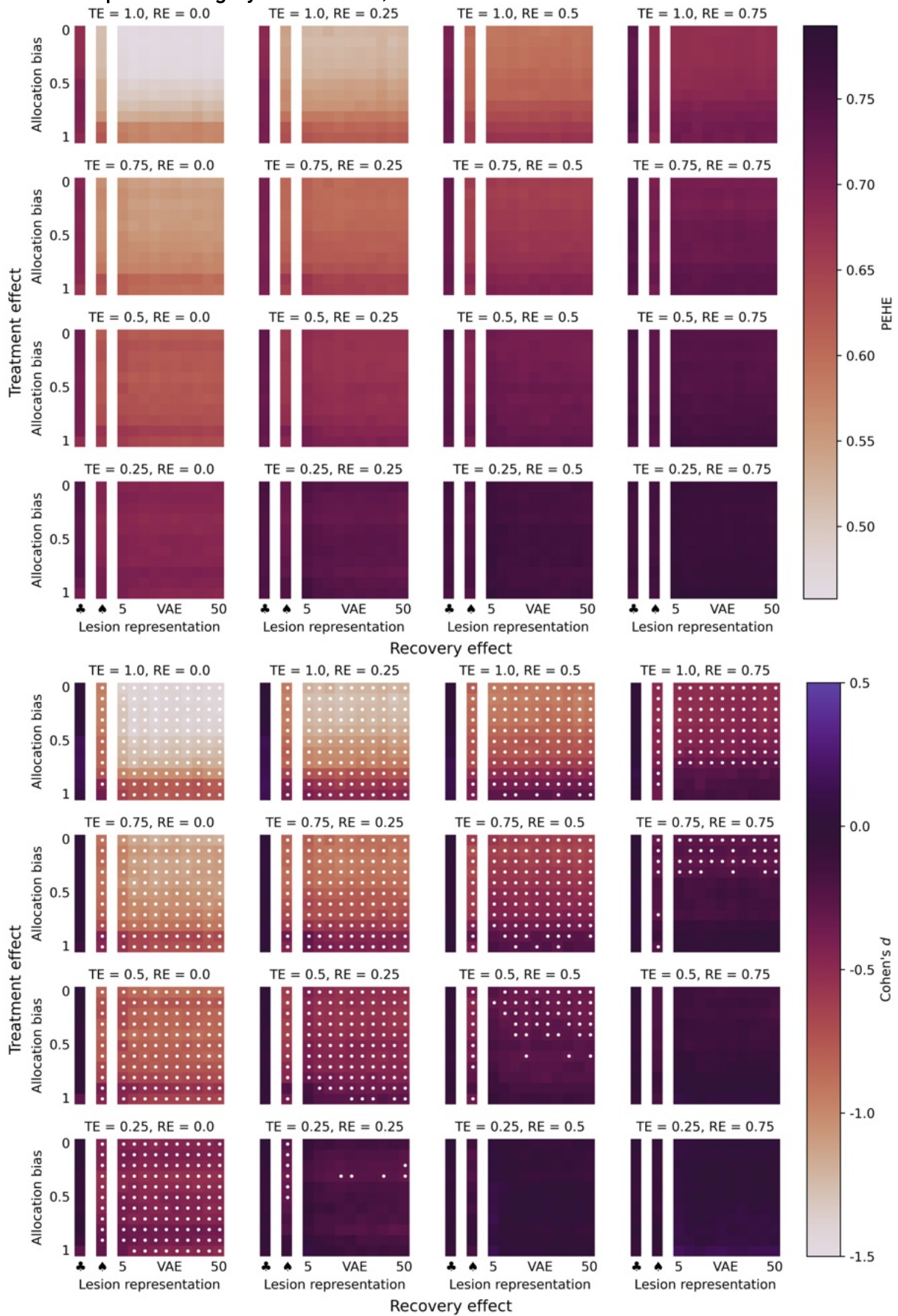


Figure S11.3. Performance comparison of models with lesion representations: PEHE (upper panel) and statistical analysis (lower panel). Prescriptive performance of an optimized, extremely randomized trees-based treatment recommendation system, given binary lesion representations, across the range of response noise (major axes) and allocation bias (minor y-axes), at various levels of expressivity of the individualized representation quantified by embedding length (minor x-axes). The columns to the left of each minor axis show prescriptive performance when individual phenotypes are represented by classification of major affected arterial territory: anterior or posterior circulation (♣) and ACA/MCA/posterior cerebral artery/VB (♠). The upper left subplot shows performance under zero response noise and the lower right subplot shows performance under the conditions of extremely high response noise. The top row of each subplot shows perfect randomization, with zero allocation bias. The upper panel shows prescriptive performance measured by PEHE the root-mean-squared-error in estimation of the true individualized treatment effect (lower is better).

The lower panel shows Cohen's *d*-effect sizes, by colour, when comparing the prescriptive performance (measured by PEHE, as shown in the upper panel) against a randomized trial based upon individualized information consisting of the major vascular supply (anterior or posterior circulation), at each respective TE/RE pair. Warm colours show performance greater than the comparative randomized trial, while cool colours show the converse. White shows equivalent performance. Trials marked with a circle indicate an effect size exceeding the critical *p*-value 0.0285 (as adjusted for multiple comparisons at the 0.05 significance level, according to the Benjamini–Hochberg procedure), corresponding to the *t*-value in a two-sided independent sample *t*-test. Filled circles show superiority of the prescriptive model from observational data; unfilled circles show superiority of the randomized trial.

TE: treatment effect; RE: recovery effect; VAE: variational auto-encoder representation; ACA: anterior cerebral artery; MCA: middle cerebral artery; VB: vertebrobasilar artery

S12: Disconnectome representations & location bias results

S12.1: Full results table

Representation	Model	Configuration	Balanced accuracy	PEHE
AE	ExtraTrees	Two	0.718161	0.573161
VAE	ExtraTrees	Two	0.712637	0.576710
AE	Logistic regression	Two	0.711435	0.564923
AE	Random forest	Two	0.708890	0.574772
PCA	ExtraTrees	Two	0.707576	0.579157
VAE	Logistic regression	Two	0.705775	0.568535
AE	ExtraTrees	One	0.705127	0.593895
VAE	Random forest	Two	0.704094	0.578082
VAE	ExtraTrees	One	0.699950	0.596088
AE	XGBoost	Two	0.699258	0.611886
VAE	XGBoost	Two	0.695058	0.616278
PCA	Random forest	Two	0.694213	0.581038
PCA	ExtraTrees	One	0.694118	0.596600
PCA	Logistic regression	Two	0.691628	0.590505
PCA	XGBoost	Two	0.687607	0.617454
NMF	Gaussian process	Two	0.686881	0.617289
NMF	Gaussian process	One	0.682916	0.617831
NMF	ExtraTrees	Two	0.680377	0.597582
NMF	Logistic regression	Two	0.669639	0.583176
NMF	ExtraTrees	One	0.666861	0.614481
AE	Random forest	One	0.661850	0.629989
VAE	Random forest	One	0.658928	0.631005
AE	XGBoost	One	0.653617	0.608419
VAE	XGBoost	One	0.650446	0.610225
NMF	Random forest	Two	0.648854	0.620553
NMF	XGBoost	Two	0.648703	0.646442
PCA	Random forest	One	0.647613	0.631801
PCA	XGBoost	One	0.638673	0.611830
NMF	XGBoost	One	0.629108	0.617982
NMF	Random forest	One	0.612928	0.646711
AE	Gaussian process	One	0.612842	0.679290
AE	Gaussian process	Two	0.610761	0.679116
VAE	Gaussian process	One	0.609586	0.676570
VAE	Gaussian process	Two	0.607783	0.676405
PCA	Gaussian process	Two	0.515168	0.684232
PCA	Gaussian process	One	0.514813	0.684112
PCA	Logistic regression	One	0.500099	0.633768
VAE	Logistic regression	One	0.500000	0.634573
AE	Logistic regression	One	0.500000	0.634102
NMF	Logistic regression	One	0.500000	0.634233

S12.2: Optimal model by balanced accuracy: AE, two-model ExtraTrees

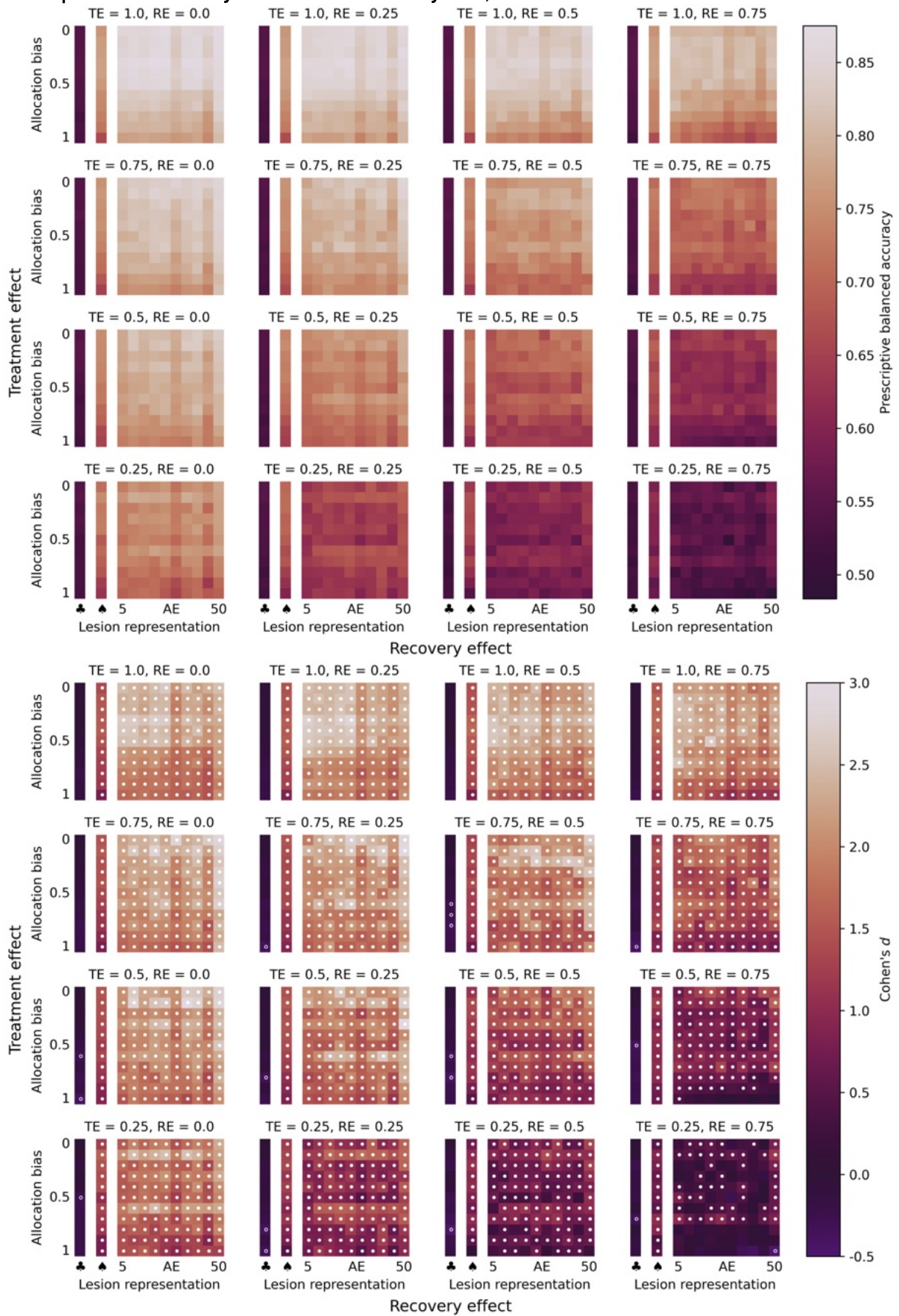


Figure S12.2. Performance comparison of models with disconnectome representations: balanced accuracy (upper panel) and statistical analysis (lower panel). Prescriptive performance of an optimized, extremely randomized trees-based treatment recommendation system, given lesion disconnectome representations, across the range of response noise (major axes) and allocation bias (minor y-axes), at various levels of expressivity of the individualized representation quantified by embedding length (minor x-axes). The columns to the left of each minor axis show prescriptive performance when individual phenotypes are represented by classification of major affected arterial territory: anterior or posterior circulation (♣) and ACA/MCA/posterior cerebral artery/VB (♠). The upper left subplot shows performance under zero response noise and the lower right subplot shows performance under the conditions of extremely high response noise. The top row of each subplot shows perfect randomization, with zero allocation bias. The upper panel shows prescriptive performance measured by balanced accuracy—the mean proportion of patients allocated to the treatment for which they are truly responsive—for patients that are exclusively responsive to one treatment.

The lower panel shows Cohen's *d*-effect sizes, by colour, when comparing the prescriptive performance (measured by balanced accuracy, as shown in the upper panel) against a randomized trial based upon individualized information consisting of the major vascular supply (anterior or posterior circulation), at each respective TE/RE pair. Warm colours show performance greater than the comparative randomized trial, while cool colours show the converse. White shows equivalent performance. Trials marked with a circle indicate an effect size exceeding the critical *p*-value 0.0439 (as adjusted for multiple comparisons at the 0.05 significance level, according to the Benjamini–Hochberg procedure), corresponding to the *t*-value in a two-sided independent sample *t*-test. Filled circles show superiority of the prescriptive model from observational data; unfilled circles show superiority of the randomized trial.

TE: treatment effect; RE: recovery effect; AE: auto-encoder representation; ACA: anterior cerebral artery; MCA: middle cerebral artery; VB: vertebrobasilar artery

S12.3 Optimal model by PEHE: AE, two-model logistic regression

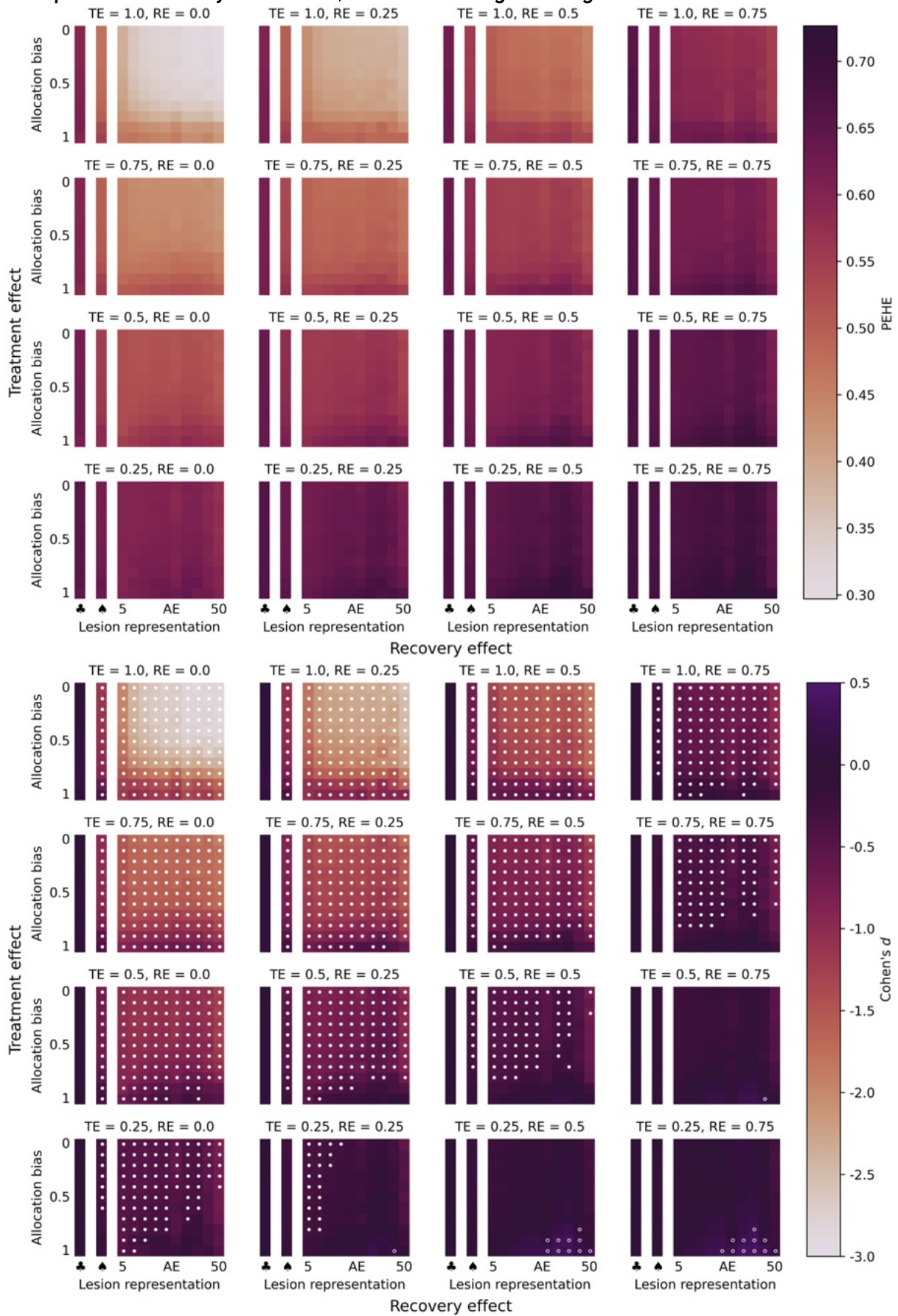


Figure S12.3. Performance comparison of models with disconnectome representations: PEHE (upper panel) and statistical analysis (lower panel). Prescriptive performance of an optimized, logistic regression-based treatment recommendation system, given lesion disconnectome representations, across the range of response noise (major axes) and allocation bias (minor y -axes), at various levels of expressivity of the individualized representation quantified by embedding length (minor x -axes). The columns to the left of each minor axis show prescriptive performance when individual phenotypes are represented by classification of major affected arterial territory: anterior or posterior circulation (♣) and ACA/MCA/posterior cerebral artery/VB (♠). The upper left subplot shows performance under zero response noise and the lower right subplot shows performance under the conditions of extremely high response noise. The top row of each subplot shows perfect randomization, with zero allocation bias. The upper panel shows prescriptive performance measured by PEHE the root-mean-squared-error in estimation of the true individualized treatment effect (lower is better).

The lower panel shows Cohen's d -effect sizes, by colour, when comparing the prescriptive performance (measured by PEHE, as shown in the upper panel) against a randomized trial based upon individualized information consisting of the major vascular supply (anterior or posterior circulation), at each respective TE/RE pair. Warm colours show performance greater than the comparative randomized trial, while cool colours show the converse. White shows equivalent performance. Trials marked with a circle indicate an effect size exceeding the critical p -value 0.0308 (as adjusted for multiple comparisons at the 0.05 significance level, according to the Benjamini-Hochberg procedure), corresponding to the t -value in a two-sided independent sample t -test. Filled circles show superiority of the prescriptive model from observational data; unfilled circles show superiority of the randomized trial.

TE: treatment effect; RE: recovery effect; AE: auto-encoder representation; ACA: anterior cerebral artery; MCA: middle cerebral artery; VB: vertebrobasilar artery

S13: Lesion representations & unobservable bias results

S13.1: Full results table

Representation	Model	Configuration	Balanced accuracy	PEHE
VAE	ExtraTrees	Two	<i>0.634868</i>	<i>0.675041</i>
VAE	Random forest	Two	0.632986	0.675653
PCA	Random forest	Two	0.629856	0.677745
AE	ExtraTrees	Two	0.629503	0.680522
PCA	ExtraTrees	Two	0.628197	0.683752
AE	Random forest	Two	0.626798	0.680120
VAE	Logistic regression	Two	0.626791	0.705085
AE	Logistic regression	Two	0.626455	0.709188
VAE	ExtraTrees	One	0.621575	0.698383
PCA	ExtraTrees	One	0.616874	0.697986
AE	ExtraTrees	One	0.616618	0.699988
VAE	XGBoost	Two	0.615532	0.716068
PCA	XGBoost	Two	0.613898	0.716403
AE	XGBoost	Two	0.612566	0.718603
NMF	ExtraTrees	Two	0.607165	0.705433
PCA	Logistic regression	Two	0.606519	0.723128
NMF	ExtraTrees	One	0.605393	0.708592
NMF	Random forest	Two	0.597810	0.704014
NMF	Random forest	One	0.583920	0.727636
VAE	Random forest	One	0.583522	0.731577
AE	Random forest	One	0.582877	0.731212
PCA	Random forest	One	0.581141	0.732307
AE	XGBoost	One	0.571251	0.715186
VAE	XGBoost	One	0.570046	0.716167
PCA	XGBoost	One	0.566437	0.716168
NMF	XGBoost	Two	0.565989	0.760494
VAE	Gaussian process	One	0.560465	0.759893
VAE	Gaussian process	Two	0.559801	0.758888
NMF	XGBoost	One	0.558269	0.721118
NMF	Gaussian process	Two	0.543848	0.714962
NMF	Gaussian process	One	0.538039	0.717106
NMF	Logistic regression	Two	0.537959	0.713148
PCA	Gaussian process	Two	0.533801	0.755991
AE	Gaussian process	One	0.532606	0.760836
PCA	Gaussian process	One	0.532467	0.757201
AE	Gaussian process	Two	0.532157	0.759965
PCA	Logistic regression	One	0.484090	0.730363
VAE	Logistic regression	One	0.483963	0.730514
AE	Logistic regression	One	0.483900	0.731088
NMF	Logistic regression	One	0.482509	0.731510

S13.2: Optimal model by balanced accuracy: VAE, two-model ExtraTrees

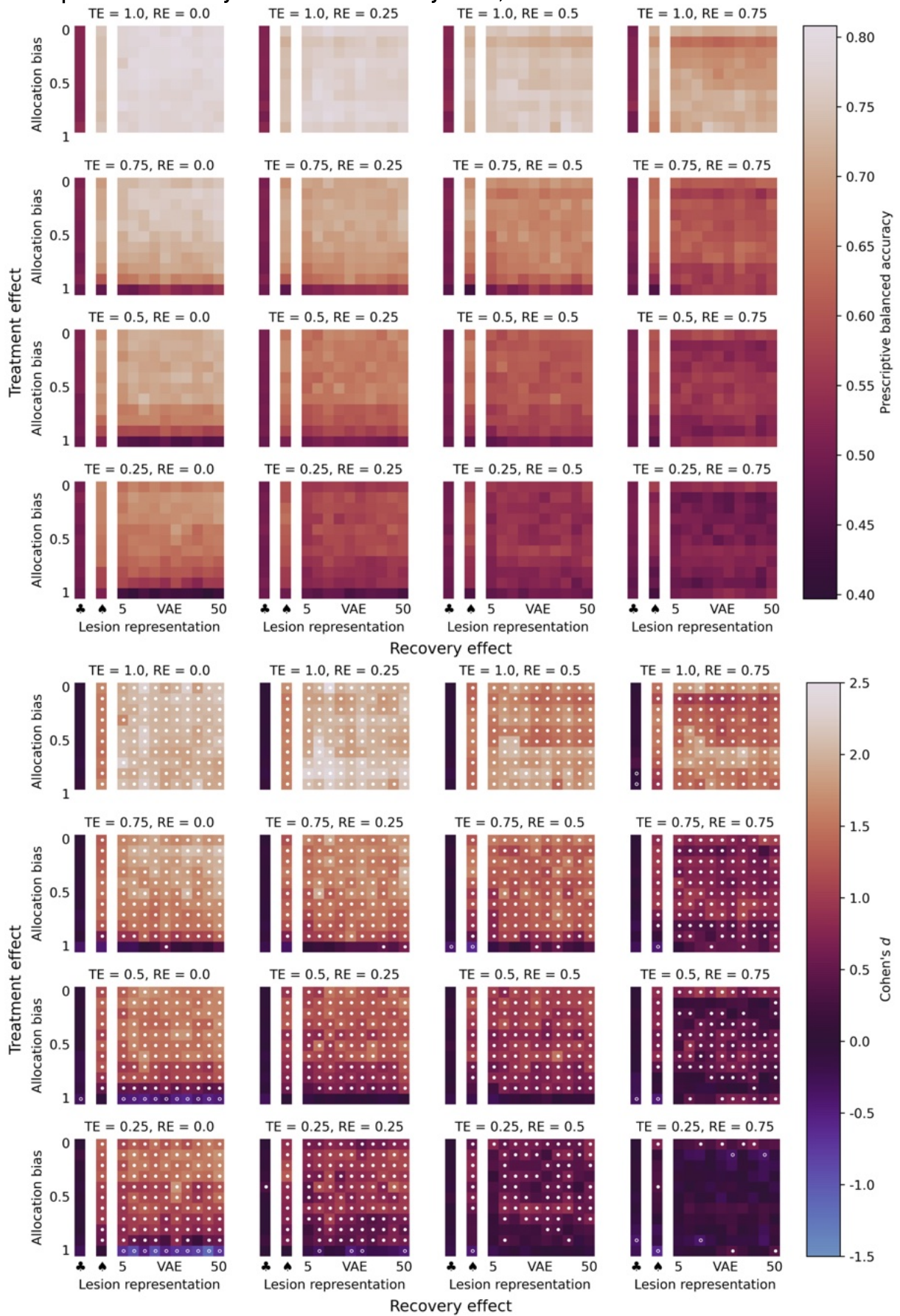


Figure S13.2. Performance comparison of models with lesion representations: balanced accuracy (upper panel) and statistical analysis (lower panel). Prescriptive performance of an optimized, extremely randomized trees-based treatment recommendation system, given binary lesion representations, across the range of response noise (major axes) and allocation bias (minor y -axes), at various levels of expressivity of the individualized representation quantified by embedding length (minor x -axes). The columns to the left of each minor axis show prescriptive performance when individual phenotypes are represented by classification of major affected arterial territory: anterior or posterior circulation (♣) and ACA/MCA/posterior cerebral artery/VB (♠). The upper left subplot shows performance under zero response noise and the lower right subplot shows performance under the conditions of extremely high response noise. The top row of each subplot shows perfect randomization, with zero allocation bias. The upper panel shows prescriptive performance measured by balanced accuracy—the mean proportion of patients allocated to the treatment for which they are truly responsive—for patients that are exclusively responsive to one treatment.

The lower panel shows Cohen's d -effect sizes, by colour, when comparing the prescriptive performance (measured by balanced accuracy, as shown in the upper panel) against a randomized trial based upon individualized information consisting of the major vascular supply (anterior or posterior circulation), at each respective TE/RE pair. Warm colours show performance greater than the comparative randomized trial, while cool colours show the converse. White shows equivalent performance. Trials marked with a circle indicate an effect size exceeding the critical p -value 0.0391 (as adjusted for multiple comparisons at the 0.05 significance level, according to the Benjamini–Hochberg procedure), corresponding to the t -value in a two-sided independent sample t -test. Filled circles show superiority of the prescriptive model from observational data; unfilled circles show superiority of the randomized trial.

TE: treatment effect; RE: recovery effect; VAE: variational auto-encoder representation; ACA: anterior cerebral artery; MCA: middle cerebral artery; VB: vertebrobasilar artery

13.3: Optimal model by PEHE: VAE, two-model ExtraTrees

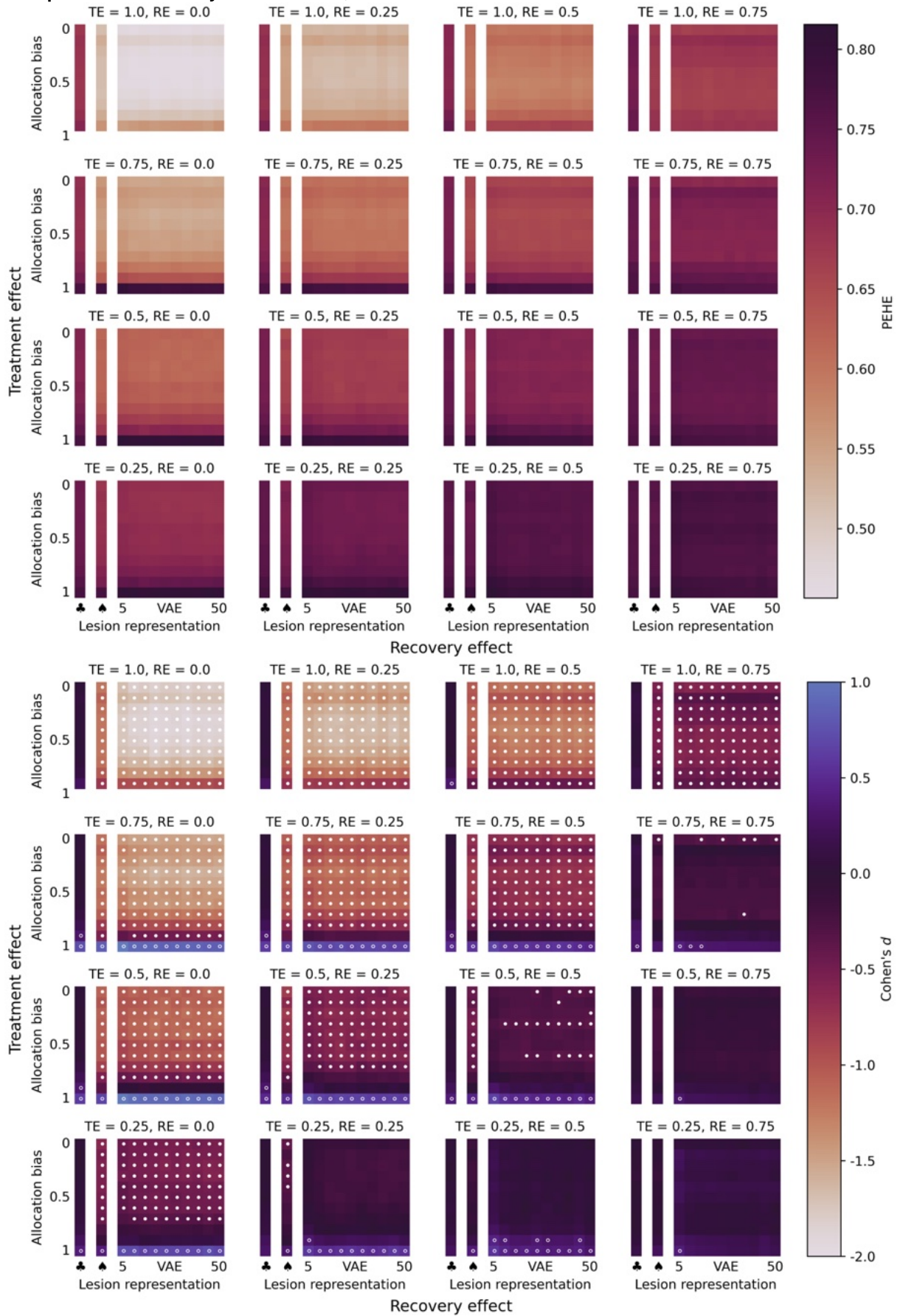


Figure S13.3. Performance comparison of models with lesion representations: PEHE (upper panel) and statistical analysis (lower panel). Prescriptive performance of an optimized, extremely randomized trees-based treatment recommendation system, given binary lesion representations, across the range of response noise (major axes) and allocation bias (minor y-axes), at various levels of expressivity of the individualized representation quantified by embedding length (minor x-axes). The columns to the left of each minor axis show prescriptive performance when individual phenotypes are represented by classification of major affected arterial territory: anterior or posterior circulation (♣) and ACA/MCA/posterior cerebral artery/VB (♠). The upper left subplot shows performance under zero response noise and the lower right subplot shows performance under the conditions of extremely high response noise. The top row of each subplot shows perfect randomization, with zero allocation bias. The upper panel shows prescriptive performance measured by PEHE the root-mean-squared-error in estimation of the true individualized treatment effect (lower is better).

The lower panel shows Cohen's *d*-effect sizes, by colour, when comparing the prescriptive performance (measured by PEHE, as shown in the upper panel) against a randomized trial based upon individualized information consisting of the major vascular supply (anterior or posterior circulation), at each respective TE/RE pair. Warm colours show performance greater than the comparative randomized trial, while cool colours show the converse. White shows equivalent performance. Trials marked with a circle indicate an effect size exceeding the critical *p*-value 0.0280 (as adjusted for multiple comparisons at the 0.05 significance level, according to the Benjamini–Hochberg procedure), corresponding to the *t*-value in a two-sided independent sample *t*-test. Filled circles show superiority of the prescriptive model from observational data; unfilled circles show superiority of the randomized trial.

TE: treatment effect; RE: recovery effect; VAE: variational auto-encoder representation; ACA: anterior cerebral artery; MCA: middle cerebral artery; VB: vertebrobasilar artery

S14: Disconnectome representations & unobservable bias results

S14.1: Full results table

Representation	Model	Configuration	Balanced accuracy	PEHE
AE	ExtraTrees	Two	0.718837	0.579313
AE	Random forest	Two	0.714471	0.578065
VAE	ExtraTrees	Two	0.712073	0.582655
PCA	ExtraTrees	Two	0.710911	0.584353
VAE	Random forest	Two	0.708585	0.581181
AE	ExtraTrees	One	0.708433	0.596302
AE	Logistic regression	Two	0.707938	0.569637
VAE	Logistic regression	Two	0.703190	0.572824
VAE	ExtraTrees	One	0.703130	0.598384
PCA	Random forest	Two	0.702288	0.583597
PCA	ExtraTrees	One	0.699538	0.599767
NMF	Gaussian process	Two	0.699174	0.619340
AE	XGBoost	Two	0.697737	0.618557
NMF	Gaussian process	One	0.695420	0.620670
PCA	Logistic regression	Two	0.693443	0.585198
VAE	XGBoost	Two	0.693418	0.622570
PCA	XGBoost	Two	0.690214	0.621575
NMF	ExtraTrees	Two	0.680675	0.601148
AE	XGBoost	One	0.675524	0.604095
VAE	XGBoost	One	0.672516	0.606058
NMF	Logistic regression	Two	0.671997	0.589040
NMF	ExtraTrees	One	0.671001	0.615725
AE	Random forest	One	0.670605	0.629387
VAE	Random forest	One	0.666972	0.630420
PCA	XGBoost	One	0.661126	0.608323
PCA	Random forest	One	0.655172	0.632082
NMF	Random forest	Two	0.650144	0.623045
NMF	XGBoost	One	0.648049	0.614402
NMF	XGBoost	Two	0.647411	0.651443
AE	Gaussian process	One	0.643552	0.678775
AE	Gaussian process	Two	0.642924	0.677752
VAE	Gaussian process	Two	0.631617	0.675007
VAE	Gaussian process	One	0.631354	0.676044
NMF	Random forest	One	0.621269	0.646555
PCA	Gaussian process	Two	0.516954	0.683877
PCA	Gaussian process	One	0.516913	0.684464
PCA	Logistic regression	One	0.500040	0.638890
AE	Logistic regression	One	0.500000	0.639670
NMF	Logistic regression	One	0.500000	0.642166
VAE	Logistic regression	One	0.500000	0.640058

S14.2: Optimal model by balanced accuracy: AE, two-model ExtraTrees

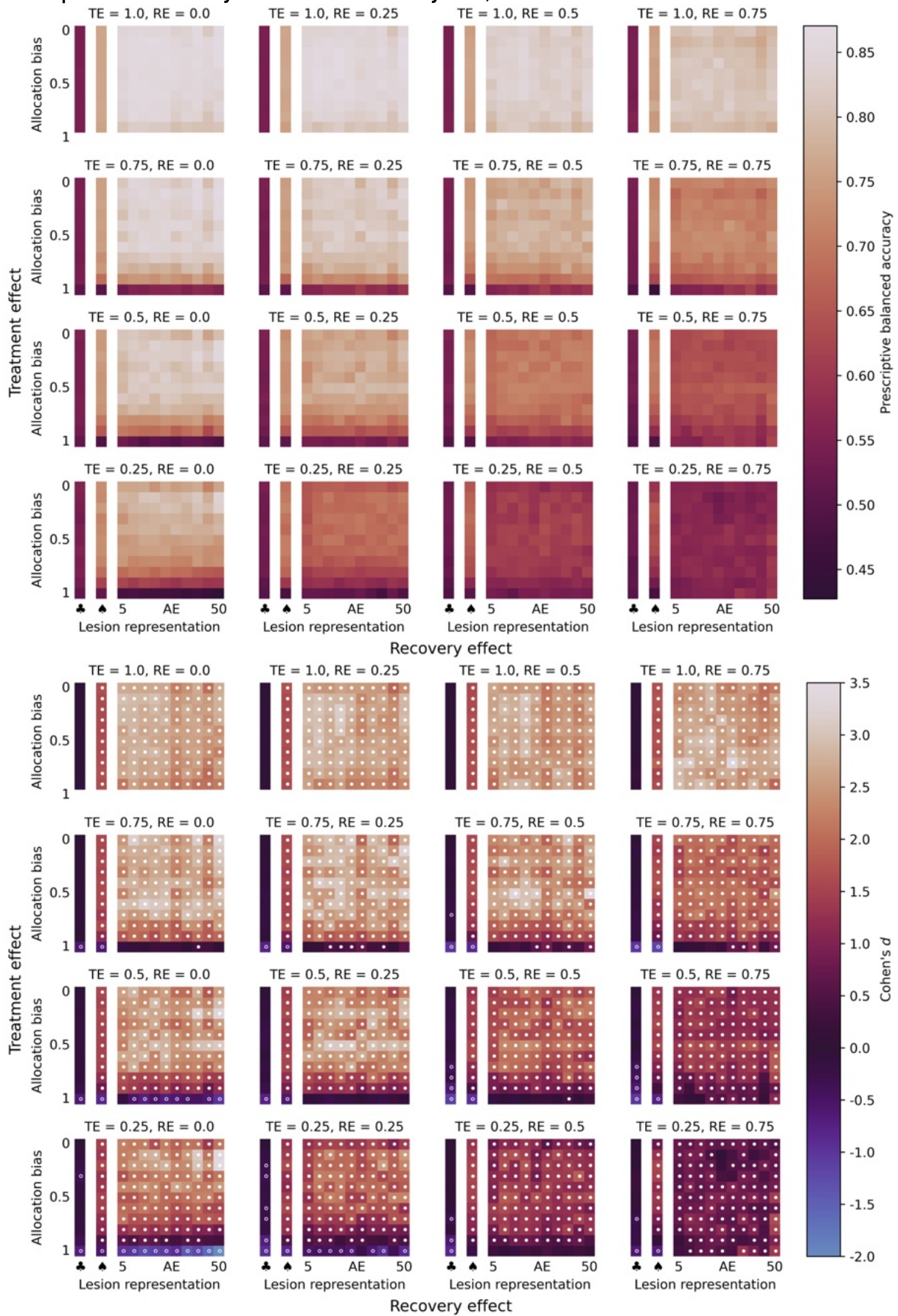


Figure S14.2. Performance comparison of models with disconnectome representations: balanced accuracy (upper panel) and statistical analysis (lower panel). Prescriptive performance of an optimized, extremely randomized trees-based treatment recommendation system, given lesion disconnectome representations, across the range of response noise (major axes) and allocation bias (minor y-axes), at various levels of expressivity of the individualized representation quantified by embedding length (minor x-axes). The columns to the left of each minor axis show prescriptive performance when individual phenotypes are represented by classification of major affected arterial territory: anterior or posterior circulation (♣) and ACA/MCA/posterior cerebral artery/VB (♠). The upper left subplot shows performance under zero response noise and the lower right subplot shows performance under the conditions of extremely high response noise. The top row of each subplot shows perfect randomization, with zero allocation bias. The upper panel shows prescriptive performance measured by balanced accuracy—the mean proportion of patients allocated to the treatment for which they are truly responsive—for patients that are exclusively responsive to one treatment.

The lower panel shows Cohen's d -effect sizes, by colour, when comparing the prescriptive performance (measured by balanced accuracy, as shown in the upper panel) against a randomized trial based upon individualized information consisting of the major vascular supply (anterior or posterior circulation), at each respective TE/RE pair. Warm colours show performance greater than the comparative randomized trial, while cool colours show the converse. White shows equivalent performance. Trials marked with a circle indicate an effect size exceeding the critical p -value 0.0429 (as adjusted for multiple comparisons at the 0.05 significance level, according to the Benjamini–Hochberg procedure), corresponding to the t -value in a two-sided independent sample t -test. Filled circles show superiority of the prescriptive model from observational data; unfilled circles show superiority of the randomized trial.

TE: treatment effect; RE: recovery effect; AE: auto-encoder representation; ACA: anterior cerebral artery; MCA: middle cerebral artery; VB: vertebrobasilar artery

S14.3: Best-performing by PEHE: AE, two-model logistic regression

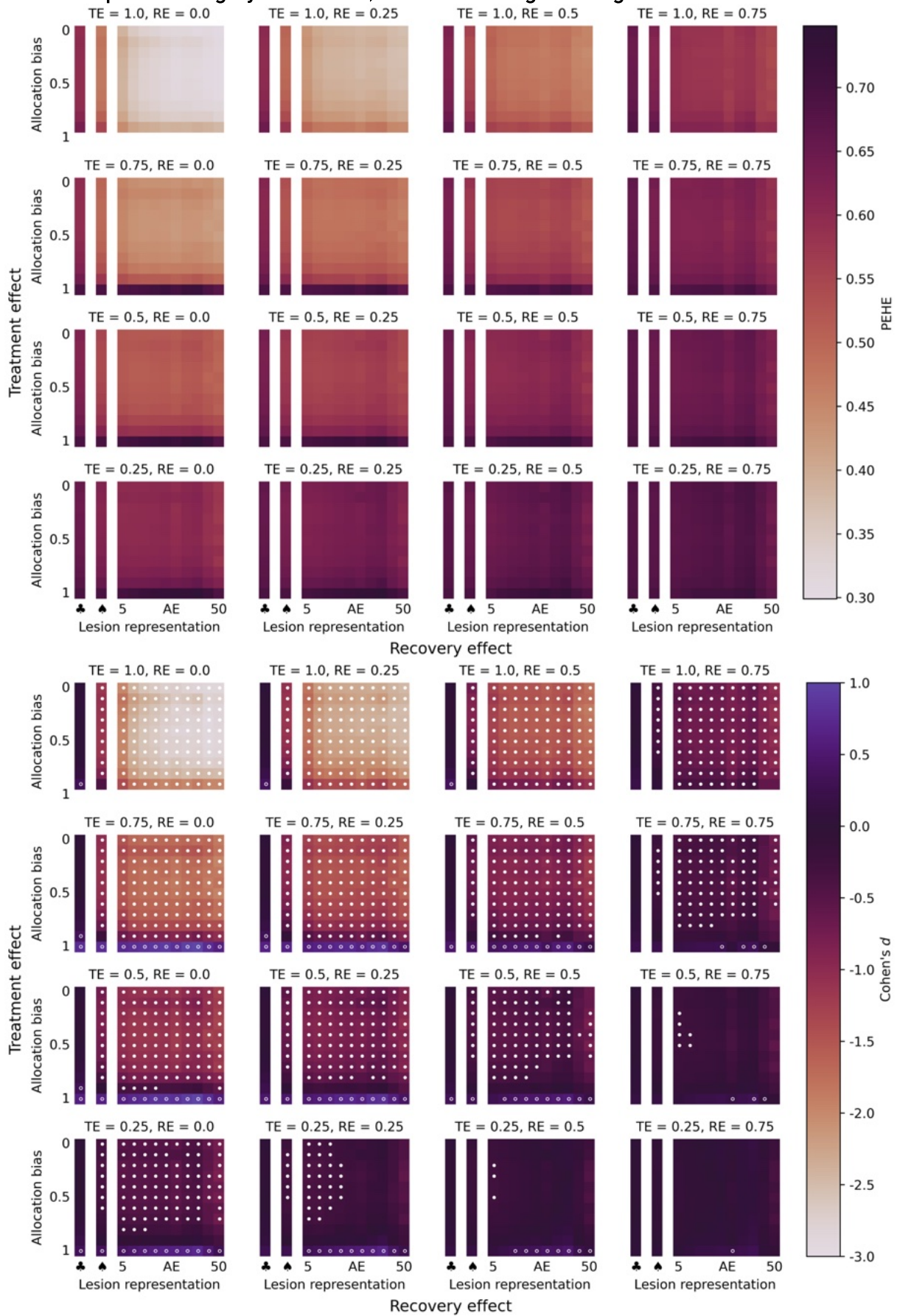


Figure S14.3. Performance comparison of models with disconnectome representations: PEHE (upper panel) and statistical analysis (lower panel). Prescriptive performance of an optimized, logistic regression-based treatment recommendation system, given lesion disconnectome representations, across the range of response noise (major axes) and allocation bias (minor y -axes), at various levels of expressivity of the individualized representation quantified by embedding length (minor x -axes). The columns to the left of each minor axis show prescriptive performance when individual phenotypes are represented by classification of major affected arterial territory: anterior or posterior circulation (♣) and ACA/MCA/posterior cerebral artery/VB (♠). The upper left subplot shows performance under zero response noise and the lower right subplot shows performance under the conditions of extremely high response noise. The top row of each subplot shows perfect randomization, with zero allocation bias. The upper panel shows prescriptive performance measured by PEHE the root-mean-squared-error in estimation of the true individualized treatment effect (lower is better).

The lower panel shows Cohen's d -effect sizes, by colour, when comparing the prescriptive performance (measured by PEHE, as shown in the upper panel) against a randomized trial based upon individualized information consisting of the major vascular supply (anterior or posterior circulation), at each respective TE/RE pair. Warm colours show performance greater than the comparative randomized trial, while cool colours show the converse. White shows equivalent performance. Trials marked with a circle indicate an effect size exceeding the critical p -value 0.0327 (as adjusted for multiple comparisons at the 0.05 significance level, according to the Benjamini–Hochberg procedure), corresponding to the t -value in a two-sided independent sample t -test. Filled circles show superiority of the prescriptive model from observational data; unfilled circles show superiority of the randomized trial.

TE: treatment effect; RE: recovery effect; AE: auto-encoder representation; ACA: anterior cerebral artery; MCA: middle cerebral artery; VB: vertebrobasilar artery

S15: Results summary by PEHE

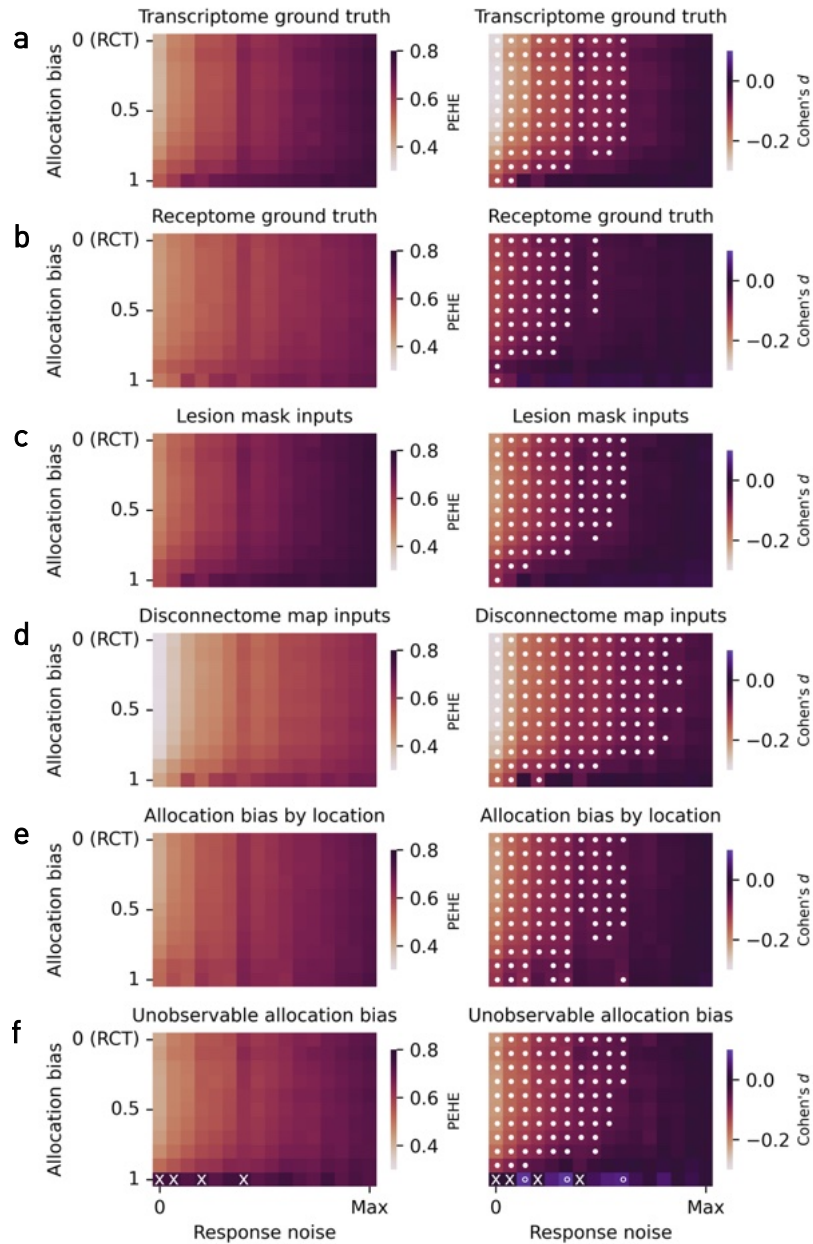


Figure S15. Prescriptive performance with the optimal richly expressive representation quantified by PEHE (left panel column, see Supplementary S11-S14 for full descriptions), and statistical comparison against a simple vascular baseline (anterior or posterior vascular territories) (right panel column). A filled circle indicates significantly higher performance for the expressive representation, and an unfilled circle significantly higher performance for the baseline model (using a Benjamini–Hochberg corrected critical value for 0.05 significance level). An 'x' indicates simulation conditions with insufficient class balance to permit prescriptive model fitting (e.g. because there are no non-responders). Rows **a** and **b** show performance averaged across the criteria for treatment responsiveness (transcriptome or receptome); rows **c** and **d** across lesion input representation type (lesion masks or disconnectomes); and rows **e** and **f** across allocation bias observability (location-based or unobservable). The optimal expressive representation is shown to be non-inferior to simple vascular territories at informing prescription across almost the full landscape of observational conditions, and superior in the majority. See Figure 6 for respective balanced accuracy plots.

S16: Results summary, stratified by deficit, by PEHE

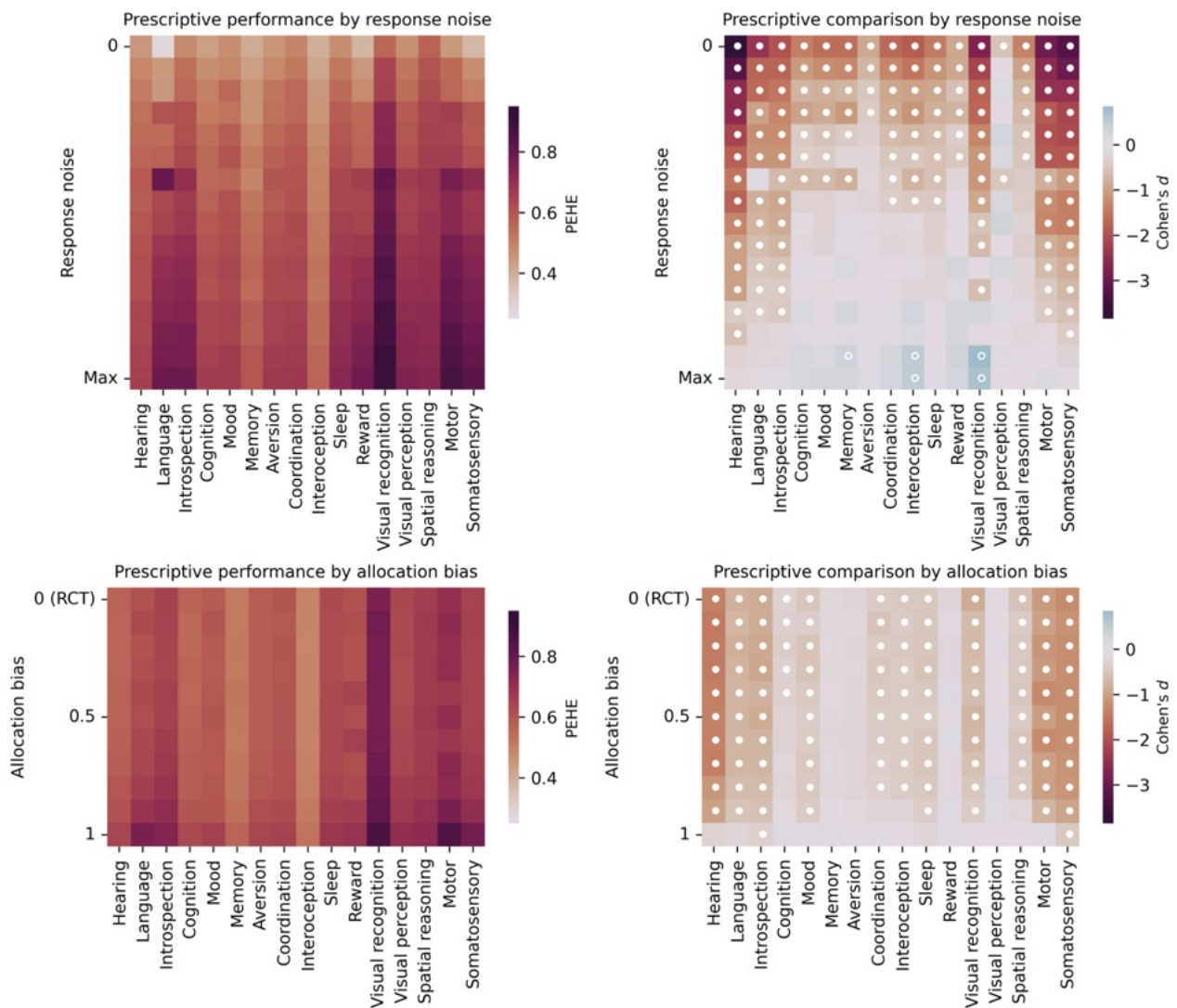


Figure S16. Prescriptive performance with the optimal richly expressive representation quantified by PEHE (see S11-S14 for full description), stratified according to the modelled functional deficit, and averaged across all simulation conditions. The right column shows Cohen's *d*-effect size when comparing prescriptive performance using the optimal representation against a simple vascular baseline. A filled circle indicates superior performance for the optimal representation, beyond the Benjamini–Hochberg corrected critical value for 0.05 significance level; an unfilled circle indicates superior performance for the simple vascular baseline correspondingly. The full anatomical—physiological modelling framework is visualized in Supplementary S9 & S10 for receptome and transcriptome, respectively. The advantage in prescriptive performance for the richly expressive approach is shown to generalize across modelled functional deficits as well as data conditions defined by outcome response noise and treatment allocation bias. See Figure 7 for respective balanced accuracy plot.

S17: Performance comparison under ideal experimental conditions

Balanced accuracy; lesion representation; location bias

Representation	Embedding length	Prescriptive model	Inferential configuration	Performance (95% CI)	Control (95% CI)	<i>t</i>	<i>p</i>	<i>d</i>
VAE	30	ExtraTrees	Two-model	0.778 (0.74, 0.84)	0.521 (0.48, 0.56)	5.78	0.0000038	1.76

Balanced accuracy; lesion representation; unobservable bias

Representation	Embedding length	Prescriptive model	Inferential configuration	Performance (95% CI)	Control (95% CI)	<i>t</i>	<i>p</i>	<i>d</i>
AE	25	ExtraTrees	Two-model	0.773 (0.71, 0.84)	0.524 (0.48, 0.57)	5.98	0.0000019	1.70

Balanced accuracy; disconnectome representation; location bias

Representation	Embedding length	Prescriptive model	Inferential configuration	Performance (95% CI)	Control (95% CI)	<i>t</i>	<i>p</i>	<i>d</i>
AE	50	ExtraTrees	Two-model	0.873 (0.80, 0.94)	0.546 (0.51, 0.58)	8.85	0.000000024	2.63

Balanced accuracy; disconnectome representation; unobservable bias

Representation	Embedding length	Prescriptive model	Inferential configuration	Performance (95% CI)	Control (95% CI)	<i>t</i>	<i>p</i>	<i>d</i>
AE	50	ExtraTrees	Two-model	0.862 (0.79, 0.94)	0.546 (0.51, 0.58)	8.29	0.000000098	2.52

PEHE; lesion representation; location bias

Representation	Embedding length	Prescriptive model	Inferential configuration	Performance (95% CI)	Control (95% CI)	<i>t</i>	<i>p</i>	<i>d</i>
AE	25	ExtraTrees	Two-model	0.465 (0.42, 0.50)	0.676 (0.61, 0.74)	-5.53	0.0000058	-1.44

PEHE; lesion representation; unobservable bias

Representation	Embedding length	Prescriptive model	Inferential configuration	Performance (95% CI)	Control (95% CI)	<i>t</i>	<i>p</i>	<i>d</i>
Lateralized arterial territory atlas	N/A	Random forest	Two-model	0.516 (0.46, 0.57)	0.676 (0.62, 0.73)	-3.71	0.00083	-0.957

PEHE; disconnectome representation; location bias

Representation	Embedding length	Prescriptive model	Inferential configuration	Performance (95% CI)	Control (95% CI)	<i>t</i>	<i>p</i>	<i>d</i>
VAE	50	Logistic regression	Two-model	0.305 (0.26, 0.34)	0.592 (0.54, 0.64)	-6.04	0.0000066	-2.27

PEHE; disconnectome representation; unobservable bias

Representation	Embedding length	Prescriptive model	Inferential configuration	Performance (95% CI)	Control (95% CI)	<i>t</i>	<i>p</i>	<i>d</i>
VAE	50	Logistic regression	Two-model	0.304 (0.27, 0.34)	0.592 (0.54, 0.64)	-6.33	0.0000028	-2.34

S18: Glossary

Average treatment effect, ATE: $\mathbb{E}[Y_i^{(A)} - Y_i^{(B)}]$. The expected difference between two potential outcomes. Sometimes referred to as the population average treatment effect, or PATE.

Conditional average treatment effect, CATE: $\hat{\tau}(\mathbf{x}_i) := \mathbb{E}[Y_i^{(A)} - Y_i^{(B)} \mid \mathbf{X} = \mathbf{x}_i]$. The expected difference between potential outcomes for individual i , conditioned on phenotype characterisation, \mathbf{x}_i .

Confounding hyperparameter: a hyperparameter that controls the association between treatment allocation and outcome when generating virtual trial data.

Identifiability: a causal quantity such as the ATE, or the CATE, is *identifiable* if it can be estimated, typically given a set of assumptions.

Individualized treatment effect, ITE: $\tau_i := Y_i^{(A)} - Y_i^{(B)}$. The difference between the two potential outcomes for individual i .

Prescriptive inference: inferring how to prescribe a treatment from predictive models of potential outcomes.

Treatment responsiveness: $\mathbb{P}(Y = 1 \mid W = w, \mathbf{X} = \mathbf{x})$. The probability of a favourable outcome for an individual, with phenotype characterisation \mathbf{x} , given treatment w .

Virtual trial: a set of semi-synthetic observational data, $\{(\mathbf{x}_i, w_i, y_i)\}_{i=1}^n$, with a framework for deciding treatment allocation and responsiveness, CATE estimation, inferring prescriptions and then evaluating this inference. The phenotype characterisations are representations of real ischaemic stroke lesions. The allocation and responsiveness framework is designed to promote biological plausibility, using functional, transcriptomic and receptomic data. Framework hyperparameters control confounding and response noise.